

Constraints on the Electroweak Sector in the Phenomenological MSSM by the ATLAS Experiment

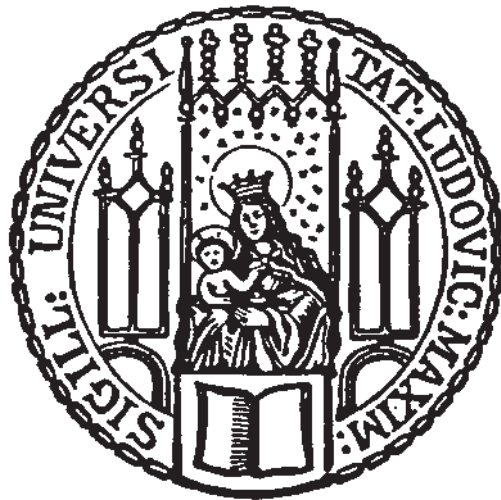


Master Thesis at the Faculty of Physics
of the
Ludwig-Maximilians-Universität München

Markus Eck
December 2021

Supervisor: Jeanette Lorenz

Einschränkungen auf den elektroschwachen Sektor im phenomenologischen MSSM durch das ATLAS Experiment



Masterarbeit an der Fakultät für Physik
der
Ludwig-Maximilians-Universität München

Markus Eck
Dezember 2021

Betreuerin: Jeanette Lorenz

Abstract

While the Standard Model of particle physics is a theoretical framework extremely well validated by experiments, it cannot provide answers to a number of questions raised by observations and theoretical considerations. This motivates the introduction of extensions of the Standard Model, as e.g. supersymmetric theories. Supersymmetry associates supersymmetric partners to the Standard Model particles and can thus, for example, provide a candidate for dark matter.

In the first part of this work a search for the electroweak production of supersymmetric particles with compressed mass spectra in a final state with two same-flavour leptons, high missing transverse momentum and hadronic activity is presented. The search uses 139 fb^{-1} of data from proton-proton collisions at a center-of-mass energy of $\sqrt{s} = 13 \text{ TeV}$, recorded with the ATLAS detector at the Large Hadron Collider. No significant deviation from the Standard Model prediction is seen in data and the analysis sets limits on the supersymmetric particles in simplified models. The search is able to exclude electroweakinos in scenarios with very small mass splittings down to 1.5 GeV .

In the second part of this work larger efforts within the ATLAS cooperation, in which the presented search is embedded in, are introduced. These efforts aim to perform a large-scale reinterpretation of ATLAS searches for electroweak production of supersymmetric particles in a subspace of a set of more complete supersymmetric models. Analysis simplifications necessary to perform such computationally challenging, large-scale reinterpretations are discussed. Preliminary studies are performed and their results are discussed, with a focus on the impact of the search presented in the first part of this work on the more complex model space. Ideas for additional efforts with a special focus on the dark matter perspective are also presented.

Zusammenfassung

Obwohl das Standardmodell der Teilchenphysik eine sehr gut durch Experimente verifizierte Theorie ist, gibt es durch Beobachtungen und theoretische Überlegungen aufgeworfene Fragen, die es nicht beantworten kann. Diese Tatsache ist der Grund für die Einführung von Erweiterungen des Standardmodells wie z.B. supersymmetrische Theorien. Supersymmetrie sagt die Existenz von supersymmetrischen Partnern für die Teilchen des Standardmodells voraus und kann somit unter anderem einen Teilchenkandidaten für Dunkle Materie liefern.

Im ersten Abschnitt dieser Arbeit wird eine Suche nach, durch die elektroschwache Wechselwirkung produzierten, supersymmetrischen Teilchen mit sehr komprimierten Massespektren vorgestellt. Endzustände mit einem Elektron-Positron- oder Myon-Antimyon-Paar, hoher fehlender Transversalenergie und hadronischer Aktivität werden untersucht. Die Suche berücksichtigt 139 fb^{-1} an Daten aus Proton-Proton Kollisionen bei Schwerpunktsenergien von $\sqrt{s} = 13 \text{ TeV}$, die mit dem ATLAS Detektor am Large Hadron Collider aufgezeichnet wurden. In den Daten wird keine signifikante Abweichung von den Vorhersagen des Standardmodells beobachtet, weshalb die Analyse dazu benutzt wird gewisse Bereiche für die Massen der supersymmetrischen Teilchen vereinfachter Modelle auszuschließen. Die Suche kann Neutralinos und Charginos in Szenarien mit sehr geringen Massendifferenzen bis zu $1,5 \text{ GeV}$ ausschließen.

Im zweiten Teil der Arbeit werden übergeordnete Forschungsanstrengungen innerhalb der ATLAS Kollaboration beschrieben, in welche die beschriebene Suche eingebettet ist. Das Ziel dieser Studien ist eine umfassende Neuinterpretation von Suchen nach, durch die elektroschwache Wechselwirkung erzeugten, supersymmetrischen Teilchen in einem Unterraum einer Menge von vollständigeren supersymmetrischen Modellen. Die notwendigen Vereinfachungen bezüglich der Analysen um eine solche rechenintensive Neuinterpretation durchzuführen werden besprochen. Vorläufige Studien werden durchgeführt und deren Ergebnisse werden diskutiert mit einem Fokus auf den Effekt der im ersten Abschnitt besprochenen Suche auf den komplexeren Modellraum. Darüber hinaus werden Ideen für weitere Forschungsanstrengungen mit einem speziellen Fokus auf die Interpretation hinsichtlich Dunkler Materie präsentiert.

Contents

1	Introduction	1
2	Theory	3
2.1	The Standard Model of particle physics	3
2.1.1	Particle content of the Standard Model	3
2.1.2	The Standard Model as a gauge quantum field theory	4
2.2	Supersymmetry	10
2.2.1	Motivations for Supersymmetry	10
2.2.2	Supersymmetry algebra and supermultiplets	12
2.2.3	Particle content of the MSSM	13
2.2.4	Supersymmetry breaking	14
2.2.5	R-parity	15
2.2.6	The phenomenological MSSM	15
2.2.7	Simplified models	16
3	Experiment	17
3.1	The Large Hadron Collider	17
3.2	The ATLAS Experiment	19
3.2.1	Coordinate system	21
3.2.2	Inner detector	21
3.2.3	Calorimeters	22
3.2.4	Muon spectrometer	23
3.2.5	Trigger system and data	24
4	Searching for electroweakinos with compressed mass spectra	27
4.1	Analysis overview and targeted signal scenarios	28
4.2	Object definitions and event reconstruction	30
4.2.1	Electrons	31
4.2.2	Muons	31
4.2.3	Jets	32

4.2.4	B-tagging	32
4.2.5	Tracks	33
4.2.6	Missing transverse momentum	33
4.3	Overlap removal	33
4.4	Trigger strategy	34
4.5	Analysis variables	34
4.6	Signal regions	38
4.7	Background estimation	39
4.7.1	Reducible background	39
4.7.2	Irreducible background	39
4.8	Results of the model dependent signal fit	42
5	Reinterpretations in the pMSSM	45
5.1	Truth-level analyses	46
5.2	Validation of the truth-level electroweak compressed analysis	47
5.2.1	E_T^{miss} trigger efficiencies	47
5.2.2	Comparison of kinematic distributions at preselection level	49
5.2.3	Comparison of yields in the signal regions	49
5.2.4	Computation of additional efficiencies	51
5.3	Simplified likelihood fit	51
5.4	Model generation	53
5.5	Scan results	55
5.6	Discussion	58
6	Properties of pMSSM models	61
6.1	K-means clustering	61
6.2	Clustering of pMSSM models	62
7	Dark matter interpretations of ATLAS SUSY searches	65
7.1	Run-1 electroweak pMSSM scan	65
7.1.1	Selection of models	66
7.1.2	Evaluation of models	66
7.1.3	Impact of ATLAS searches on the sampled models	67
7.2	Likelihood-driven sampling	68
7.2.1	Sampling in the spirit of Bayesian statistics	68
7.2.2	Run-1 initial likelihood scan	69
7.2.3	Construction of the likelihood	70
7.3	Updating the Run-1 procedure	71

8 Conclusion	73
A Validation of the truth-level electroweak compressed analysis	87
A.1 Comparison of kin. distributions at preselection level	87

Chapter 1

Introduction

The goal of particle physics is to provide a description of nature on the most fundamental level by studying the elementary building blocks of matter and their interactions. Especially during the second half of the 20th century a fruitful interplay between theoretical predictions and experimental observations improved the physicists' understanding of nature on the subatomic scale. These developments resulted in a theoretical framework, called the Standard Model (SM) of particle physics. Since then the SM continually proved to be a highly successful theory with many of its predictions experimentally tested to remarkable precision. The discovery of the Higgs boson by the ATLAS and CMS collaborations at the Large Hadron Collider (LHC) in 2012 experimentally completed the SM. While this discovery of the last missing constituent of the SM is another important milestone in particle physics, it also gives rise to the question of what comes next, especially in terms of experimental physics.

In fact, there are several experimental observations and theoretical considerations, which can not be explained or even addressed in the SM. For example, the existence of dark matter (DM) is well-established by cosmological observations, but no particle in the SM has suitable properties to be a candidate for it. The SM describes three of the four fundamental forces in nature, namely the electromagnetic and weak forces, which are described in a unified way as the electroweak force as well as the strong force. From the theoretical perspective it seems plausible that an extension of the SM should exist for which the three forces are described in a unified way at high energies. Ultimately a fundamental description of nature, valid at energies corresponding to the Planck scale should also contain a description of gravity.

Many different approaches to physics beyond the Standard Model (BSM), aiming to explain its shortcomings, exist. One popular theoretical framework extending the SM is Supersymmetry (SUSY), which postulates a symmetry between bosonic and fermionic states and associates supersymmetric partners to the SM particles. SUSY can thus, for example, provide a candidate particle for DM.

As theoretical considerations suggest that supersymmetric particles could have masses at a scale that can be probed with the LHC a lot of research within the ATLAS and CMS experiments is dedicated to the search for SUSY. So far no signs for the existence of supersymmetric particles have been found. After the recent completion of the second run of the LHC at an upgraded center-of-mass energy of 13 TeV a larger than ever before amount of data is available to be analysed by the researchers. This in particular enables searches for supersymmetric particles produced through the electroweak interaction, which were in the past limited by low production cross sections.

This work presents search efforts for the SUSY partners of the Higgs and gauge bosons, referred to as electroweakinos. The search uses 139 fb^{-1} of proton-proton collision data recorded

at a centre-of-mass energy of $\sqrt{s} = 13$ TeV and is interpreted in two different theoretical models with differing complexity. Chapter 2 provides an introduction to the relevant theoretical concepts of the SM and SUSY. An overview of the LHC and the ATLAS experiment is given in Chapter 3. In Chapter 4 the aforementioned search for electroweakinos is introduced and its results in the context of a simplified model are reported. The content in this chapter reviews the results of the search originally presented in Ref. [1]. Reinterpretations of SUSY searches, focusing on the search presented in the previous chapter, in a more complete supersymmetric scenario, referred to as the phenomenological Minimal Supersymmetric Standard Model (pMSSM) are discussed in Chapter 5. Chapter 6 presents studies on the properties of models in this SUSY scenarios using clustering algorithms. Efforts specifically assessing the impact of electroweakino searches from a dark matter perspective are reviewed in Chapter 7. A brief conclusion is given in Chapter 8.

Chapter 2

Theory

The aim of this chapter is to give a concise theoretical introduction to concepts necessary for the later parts of this work. The first section therefore gives a short review of the Standard Model of Particle Physics (SM). In the second part the main motivations to consider Supersymmetric theories are discussed and some important concepts and phenomenological consequences are introduced. The presentation is mostly based on Refs. [2, 3] for the SM and [4, 5] for Supersymmetry.

2.1 The Standard Model of particle physics

The Standard Model of Particle Physics is a theoretical framework, describing elementary particles and their electromagnetic, weak and strong interactions. Its foundations were laid in the 1960s with a theory by Glashow, Weinberg and Salam, combining unified electroweak interactions with the Brout-Englert-Higgs mechanism [6–11]. Especially during the 1970s it was further established by experimental discoveries and theoretical developments, e.g. the development of the theory of strong interactions [12, 13]. Predictions made by the SM were since then continually tested by experiments to very high levels of accuracy, making it a highly successful description of three of the four fundamental forces in nature. Gravity remains the only force not described within the Standard Model.

2.1.1 Particle content of the Standard Model

In the Standard Model matter is made up by three generations of electrically charged leptons and quarks of up- and down type. For every charged lepton there exists a corresponding neutral neutrino. Quarks carry an additional quantum number called colour charge, which can take one of three different values red, green and blue. All these particles are fermions with spin $s = 1/2$ and for each exists a corresponding anti-particle with the same mass and spin but inverted charge-like quantum numbers¹.

Bosons with spin $s = 1$ serve as mediators for the fundamental forces described by the SM. The massless photon γ mediates electromagnetic interactions between electrically charged particles. The weak force can only be consistently described in a unified theory together with the electromagnetic force. The vector bosons corresponding to this electroweak unification are two electrically charged W^\pm and a neutral Z boson. As opposed to the photon these are massive particles, with masses generated through the Brout-Englert-Higgs mechanism, discussed in Sec. 2.1.2. As a consequence an additional massive scalar particle, the physical

¹The existence of antiparticles is necessary in a relativistic quantum theory.

	particle	electric charge [e]	mass
leptons	electron (e)	-1	511 keV
	electron neutrino (ν_e)	0	0
	muon (μ)	-1	106 MeV
	muon neutrino (ν_μ)	0	0
	tau (τ)	-1	1.78 GeV
	tau neutrino (ν_τ)	0	0
quarks	up (u)	$\frac{2}{3}$	2.16 MeV
	down (d)	$-\frac{1}{3}$	4.67 MeV
	charm (c)	$\frac{2}{3}$	1.27 GeV
	strange (s)	$-\frac{1}{3}$	93 MeV
	top (t)	$\frac{2}{3}$	173 GeV
	bottom (b)	$-\frac{1}{3}$	4.18 GeV

Table 2.1: Overview of the fermions in the SM with their charges (in multiples of the elementary charge e) and masses. Neutrinos are stated as massless. The experimentally measured values for the stated masses as well as limits on neutrino masses can be found in [14].

particle	spin	electric charge [e]	mass
photon (γ)	1	0	0
gluon (g)	1	0	0
W^\pm	1	± 1	80.4 GeV
Z^0	1	0	91.2 GeV
Higgs boson (h)	0	0	125 GeV

Table 2.2: Overview of the bosons in the SM with their spin, charges (in multiples of the elementary charge e) and masses. Values taken from Ref. [14], rounded to three digits.

Higgs boson, appears. The discovery of the Higgs boson in 2012 is the most prominent recent progress in experimentally validating the Standard Model. Finally, the mediators of strong interactions are called gluons, which come in eight different states, each carrying a combination of colour and anti-colour². Gluons are massless and electrically neutral. The particles of the SM are summarized in Tab. 2.1 and Tab. 2.2.

2.1.2 The Standard Model as a gauge quantum field theory

The SM is an example for a quantum field theory (QFT), which is the result of combining quantum mechanics with special relativity. One reason why in a QFT one introduces (quantized) fields instead of just dealing with quantum mechanical particles is that in the relativistic regime effects that change the number of particles are important. The dynamics of these fields are described by a Lagrangian density $\mathcal{L}[\phi_i, \partial_\mu \phi_i]$ built from fields ϕ_i , which are given by representations of the Lorentz group³. For a given Lagrangian the equations of motion for the different fields are determined from the action

$$S = \int \mathcal{L}(\phi_i, \partial_\mu \phi_i) d^4x. \quad (2.1)$$

using the principle of least action $\delta S = 0$. In this way, Lagrangians constructed to be explicitly Lorentz invariant, lead to a relativistic theory.

²How this comes about is described in more detail in Sec. 2.1.2.

³In fact in the most general case the fields transform in representations of the universal cover of the Lorentz group, which is the group $SL(2, \mathbb{C})$. These include then also the spinor representations corresponding to fermions.

In order for such a theory to also describe particles, one has to make sure that these can be embedded into the fields. Particles in that sense are defined as irreducible unitary representations of the Poincaré group, which according to their classification by E. Wigner [15], are characterized by two quantum numbers, namely a non-negative real mass m and a non-negative integer or half-integer spin j . For $j = 0$ there is always only one independent state in the representation, while for $j > 0$ and $m > 0$ there are $2j + 1$ and for $m = 0$ there is exactly two.

If one now wants to construct a field theory as introduced above, also describing this notion of particles, the construction of the Lagrangian has to be such, that the right number of degrees of freedom is propagated. For example in the theory of a free massless spin-1 particle (e.g. the photon), the form of the Lagrangian has to ensure that for the Lorentz vector A_μ , which has four components, only two of them are treated as physical degrees of freedom. This is the reason, why the corresponding Lagrangian

$$\mathcal{L}_{\text{Maxwell}} = -\frac{1}{4}F_{\mu\nu}F^{\mu\nu}, \quad F_{\mu\nu} = \partial_\mu A_\nu - \partial_\nu A_\mu \quad (2.2)$$

exhibits gauge invariance, which means that it is invariant under local transformations

$$A_\mu(x) \longrightarrow A_\mu(x) + \partial_\mu \alpha(x). \quad (2.3)$$

While the concept of gauge invariance is therefore only a property (more precisely: a redundancy) of the description, it can be used as a principle for the construction of Lagrangians. In particular, when constructing an interacting theory, invariance under transformations of a certain gauge group dictates the form of the interactions.

Abelian U(1) gauge theory

The following example yielding the quantum electrodynamics (QED) Lagrangian illustrates how the gauge principle works in practice. One starts with the Dirac Lagrangian, describing a free spinor field ψ with mass m , for which the adjoint spinor is denoted by $\bar{\psi}$

$$\mathcal{L}_{\text{Dirac}} = \bar{\psi}(i\gamma^\mu \partial_\mu - m)\psi, \quad (2.4)$$

which is invariant under a global U(1) transformation

$$\psi(x) \longrightarrow \psi'(x) = \exp(i\alpha)\psi(x), \quad (2.5)$$

where α is real and spacetime independent. In order to include an interaction with a vector field, one has to make sure, that the resulting Lagrangian is invariant under local transformations with a spacetime dependent parameter⁴

$$\begin{aligned} \psi(x) &\longrightarrow \psi'(x) = \exp(i\alpha(x))\psi(x), \\ A_\mu(x) &\longrightarrow A'_\mu(x) = A_\mu(x) + \frac{1}{e}\partial_\mu \alpha(x). \end{aligned} \quad (2.6)$$

This can be done by introducing A_μ via the covariant derivative

$$D_\mu = \partial_\mu - ieA_\mu, \quad (2.7)$$

replacing the ordinary derivative in the Dirac Lagrangian. The only thing still missing is then the kinetic term for the vector field, but this is simply the free Maxwell Lagrangian (eq.

⁴A conventional factor $1/e$, where e is the elementary charge, has been added with respect to the expression from before.

2.2). Finally the Lagrangian of QED is given by

$$\begin{aligned}\mathcal{L}_{\text{QED}} &= \bar{\psi}(i\gamma^\mu D_\mu - m)\psi - \frac{1}{4}F_{\mu\nu}F^{\mu\nu} \\ &= \bar{\psi}(i\gamma^\mu \partial_\mu - m)\psi - \frac{1}{4}F_{\mu\nu}F^{\mu\nu} - e\bar{\psi}\gamma^\mu\psi A_\mu,\end{aligned}\tag{2.8}$$

which for quantized fields describes the electromagnetic interaction of charged fermions via photons.

Non-Abelian SU(N) gauge theory

For the Standard Model one also has to consider non-Abelian gauge groups [16], specifically the groups SU(N), which can be represented in the fundamental representation by unitary $N \times N$ matrices, with $\det = 1$, acting on N -dimensional vectors. As the considered groups are Lie groups, any element can be written as

$$U(\alpha^1, \dots, \alpha^n) = \exp(i\alpha^a T^a),\tag{2.9}$$

where a summation over repeated group indices is implicitly assumed, α^a are numbers parametrizing the group elements and T^a are called the group generators. For the groups SU(2) and SU(3), which are needed for the SM, there are $n = 3$ and $n = 8$ generators respectively⁵. The generators satisfy commutation relations involving the structure constants f^{abc}

$$[T^a, T^b] = if^{abc}T^c.\tag{2.10}$$

The following section extends the previous discussion to these cases. The free Lagrangian for N fermion fields (all with the same mass m), arranged in a fundamental representation multiplet $\Psi = (\psi_1, \psi_2, \dots, \psi_N)^T$ reads

$$\mathcal{L}_{\text{free}} = \bar{\Psi}(i\gamma^\mu \partial_\mu - m)\Psi,\tag{2.11}$$

and is invariant under global transformations of the SU(N) groups just introduced, for which

$$\Psi(x) \longrightarrow \Psi'(x) = U(\alpha^1, \dots, \alpha^n)\Psi(x).\tag{2.12}$$

A Lagrangian, which is invariant under the same transformations with spacetime dependent parameters, can again be constructed by the replacement

$$\partial_\mu \longrightarrow D_\mu = \partial_\mu - igW_\mu,\tag{2.13}$$

where g is the coupling constant. The gauge field can be expanded in terms of the generators as

$$W_\mu(x) = T^a W_\mu^a(x),\tag{2.14}$$

so the resulting Lagrangian describes n vector fields W_μ^a , transforming in the adjoint representation. The invariant kinetic term for the gauge fields looks similar to the one in the Abelian case and is given by

$$\mathcal{L} = -\frac{1}{4}F_{\mu\nu}^a F^{a,\mu\nu},\tag{2.15}$$

where now the field strength has components

$$F_{\mu\nu}^a = \partial_\mu W_\nu^a - \partial_\nu W_\mu^a + gf^{abc}W_\mu^b W_\nu^c.\tag{2.16}$$

The last part of this expression is quadratic in the fields W and contains the structure constants, which reflect the non-commutativity of the group transformations. This leads to cubic and quartic terms in the Lagrangian, describing self-interactions between the gauge fields.

⁵The general formula for the number of generators of SU(N) is $N^2 - 1$.

The Standard Model as a gauge theory

Finally, the Standard Model is based on the gauge group

$$SU(3)_C \otimes SU(2)_L \otimes U(1)_Y. \quad (2.17)$$

The gauge theory associated with the $SU(3)$ part in this expression is called quantum chromodynamics (QCD) and describes the strong interaction. The subscript ‘ C ’ indicates that the quantum number associated with the $SU(3)$ symmetry group is the colour charge, which can take three different values accordingly. The only fermions charged under this symmetry are the quarks, with each of them described by a triplet of fermion fields $q = (q_1, q_2, q_3)^T$. As there is $n = 8$ generators for $SU(3)$, the same number of gauge fields are introduced when constructing a gauge invariant Lagrangian, and these fields can be identified as the different gluon states. As already discussed for general $SU(N)$ gauge theories, the gluons are themselves colour-charged and therefore self-interacting. This leads to a property of QCD called asymptotic freedom, which means that at small, subnuclear distance scales the interactions between quarks and gluons become very weak. On the other hand, at large distances the coupling becomes strong, such that colour charged particles can never be observed as free particles. This phenomenon is called confinement.

Electroweak interactions of elementary particles are based on the gauge group $SU(2)_L \otimes U(1)_Y$. The subscript ‘ Y ’ stands for the weak hypercharge, while the ‘ L ’ indicates that only left-handed fermions are charged under the corresponding $SU(2)$ symmetry group. The three generations of left-handed leptons and quarks in the Standard Model form $SU(2)$ doublets

$$L_L^i = \begin{pmatrix} \nu_e \\ e \end{pmatrix}_L, \begin{pmatrix} \nu_\mu \\ \mu \end{pmatrix}_L, \begin{pmatrix} \nu_\tau \\ \tau \end{pmatrix}_L, \quad Q_L^i = \begin{pmatrix} u \\ d \end{pmatrix}_L, \begin{pmatrix} c \\ s \end{pmatrix}_L, \begin{pmatrix} t \\ b \end{pmatrix}_L, \quad (2.18)$$

while the right-handed fermions are singlets

$$\ell_R^i = e_R, \mu_R, \tau_R, \quad u_R^i = u_R, c_R, t_R \quad d_R^i = d_R, s_R, b_R. \quad (2.19)$$

With these it is then possible, following the same procedure as before, to construct a Lagrangian invariant under the respective gauge group. This time there are three gauge fields W_μ^a associated with the three generators of $SU(2)$ and one vector field B_μ associated with the hypercharge group $U(1)_Y$. In order for the Lagrangian to be gauge invariant, there can not be any mass terms for these gauge boson fields. In order for a theory to describe gauge bosons with non-zero mass, such as the W^\pm and Z^0 , the full symmetry has to be broken. In the Standard Model this is achieved through the Brout-Englert-Higgs mechanism⁶ with a spontaneous symmetry breaking pattern

$$SU(2)_L \otimes U(1)_Y \longrightarrow U(1)_{em}, \quad (2.20)$$

recovering the electromagnetic $U(1)$ gauge group. For this a $SU(2)$ doublet of complex scalar fields

$$\Phi(x) = \begin{pmatrix} \phi^+(x) \\ \phi^0(x) \end{pmatrix} \quad (2.21)$$

together with a potential

$$V(\Phi) = -\mu^2 \Phi^\dagger \Phi + \frac{\lambda}{4} (\Phi^\dagger \Phi)^2 \quad (2.22)$$

⁶The real physical purpose of the Brout-Englert-Higgs mechanism is to make sure that perturbative unitarity is not lost at high energy. The existence of the Higgs boson ensures the cancelation of problematic high-energy behaviour of scattering amplitudes coming from longitudinal components of massive vector bosons.

is introduced. The parameters μ^2 and λ are positive and real, such that the potential has the form of a mexican hat with minima for non-zero field configurations. Therefore the Higgs doublet obtains a non-zero vacuum expectation value (VEV), which can be taken to be

$$\langle \Phi \rangle = \frac{1}{\sqrt{2}} \begin{pmatrix} 0 \\ v \end{pmatrix}, \quad (2.23)$$

where $v = 2\mu/\sqrt{\lambda}$ depends on the parameters of the potential. This is not invariant under the electroweak gauge transformations and thus the vacuum spontaneously breaks the symmetry present in the Lagrangian. It can be shown, that there remains a subgroup of symmetry transformations, which is exactly the $U(1)_{em}$ associated with electromagnetism. If one expresses the Higgs field as excitations around this vacuum state and plugs this back into the potential one obtains terms corresponding to the physical, massive Higgs boson and three massless Goldstone bosons. These Goldstone bosons appear according to the Nambu-Goldstone theorem [17, 18] whenever a continuous symmetry is spontaneously broken. For a local symmetry they can be absorbed as the longitudinal component of then massive vector bosons.

The mass terms one obtains for the gauge bosons are non-diagonal, but can be diagonalized by a transformation from the fields W_μ^a and B_μ to the physical fields

$$W_\mu^\pm = \frac{1}{\sqrt{2}}(W_\mu^1 \mp iW_\mu^2) \quad (2.24)$$

and

$$\begin{pmatrix} Z_\mu \\ A_\mu \end{pmatrix} = \begin{pmatrix} \cos \theta_W & -\sin \theta_W \\ \sin \theta_W & \cos \theta_W \end{pmatrix} \begin{pmatrix} W_\mu^3 \\ B_\mu \end{pmatrix}, \quad (2.25)$$

with the weak mixing angle θ_W . After that it can be seen that the Higgs mechanism yields massive W^\pm and Z bosons, whereas the field A_μ is massless and can thus be identified with the gauge boson of the electromagnetic $U(1)_{em}$ symmetry, which is the photon.

As also fermion mass terms of the form $\bar{\psi}\psi = \bar{\psi}_L\psi_R + \bar{\psi}_R\psi_L$ are not invariant under chiral $SU(2)_L$ transformations, the Higgs doublet also serves the purpose of generating the mass of the fermions through Yukawa interactions

$$\mathcal{L}_Y = - \sum_{i,j} \left(\bar{L}_L^i Y_\ell^{ij} \ell_R^j \Phi + \bar{Q}_L^i Y_d^{ij} d_R^j \Phi + \bar{Q}_L^i Y_u^{ij} u_R^j \Phi^C \right) + h.c. , \quad (2.26)$$

with the indices i, j denoting the three generations and Yukawa coupling matrices Y_f^{ij} . For the quarks the mass terms one gets after spontaneous symmetry breaking, i.e. by replacing Φ by its vacuum expectation value, read

$$\mathcal{L}_{Y,q} = - \frac{v}{\sqrt{2}} \sum_{i,j} \left(\bar{d}_L^i Y_d^{ij} d_R^j + \bar{u}_L^i Y_u^{ij} u_R^j \right) + h.c. . \quad (2.27)$$

By transforming from the flavour to the mass eigenstates with the help of different matrices for u- and d-type quarks, these terms can be diagonalized. Applying the same transformations in the interactions of quarks with the W^\pm bosons reveals that there is mixing among the different quark flavours in the charged current (CC) part of the Lagrangian described by a unitary matrix called the Cabibbo-Kobayashi-Maskawa (CKM) matrix [19, 20]:

$$\mathcal{L}_{CC} = - \frac{g_2}{\sqrt{2}} \left(\bar{\tilde{u}}_L \gamma^\mu W_\mu^+ V_{CKM} \tilde{d}_L + \bar{\tilde{d}}_L \gamma^\mu W_\mu^- V_{CKM}^\dagger \tilde{u}_L \right). \quad (2.28)$$

Here the tilde denotes the transformed fields. The CKM matrix is parametrized by three rotation angles and one complex phase. This phase leads to violation of CP-symmetry in the

Standard Model.

Furthermore these charged current interactions are the only way to change flavour, while flavour changing neutral currents (FCNCs) are absent at tree level and generally suppressed in the SM. The agreement of the Standard Model predictions regarding flavour structure and CP-violation with experimental observations places stringent constraints on extensions of the SM.

2.2 Supersymmetry

The second section of this chapter introduces extensions of the Standard Model, for which a symmetry relating fermions and bosons, called supersymmetry (SUSY) is introduced. It starts by discussing some of the main motivations to consider supersymmetric theories. After that some key features and their mathematical description are presented, focusing on the SUSY model with minimal number of new particles, called the Minimal Supersymmetric Standard Model (MSSM). Based on that, in the last part a simplification of the MSSM, called the phenomenological MSSM (pMSSM), which is the model most relevant for the main part of this work, is introduced. The content of this chapter can be found in much more detail e.g. in Refs. [4, 5].

2.2.1 Motivations for Supersymmetry

The Hierarchy Problem

The issue described in the following, often referred to as the 'Hierarchy Problem', is not a problem of the Standard Model itself, but of any possible extension of it. Beyond Standard Model (BSM) theories are considered, because the SM can not be a complete description of nature up to arbitrarily large energy scales. At the latest at the Planck scale $M_P \approx 10^{19}$ GeV, where effects of quantum gravity become important, there has to be a new theoretical framework. The Higgs boson as a scalar particle receives loop corrections to its mass-squared m_h^2 from any other existing particle that couples directly or indirectly to the Higgs field. The

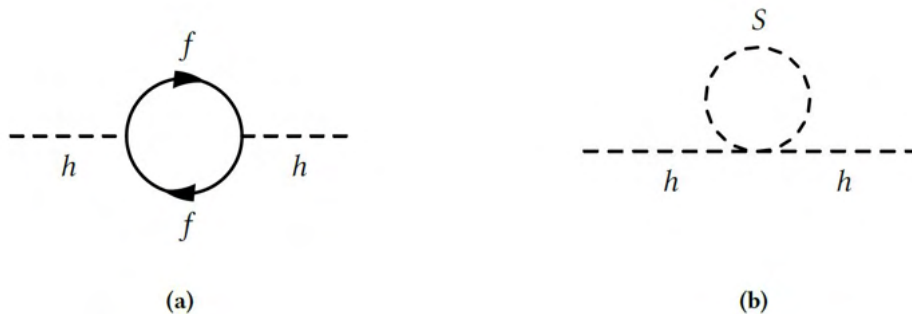


Figure 2.1: Loop diagrams with a fermion (a) and a boson (b) coupling to the Higgs boson.

contribution to these corrections from a fermion loop as depicted in Fig. 2.1(a) is given by

$$\Delta m_h^2 = -\frac{\lambda_f^2}{8\pi^2} \Lambda^2 + \dots, \quad (2.29)$$

where λ_f is the corresponding Yukawa coupling and Λ is a cutoff, with the physical interpretation to be the scale up to which the Standard Model remains valid. If one takes Λ to be the Planck scale then the correction to the Higgs mass-squared becomes much larger than the expected value itself. Similar corrections are obtained from loops involving a (hypothetical) massive scalar as in Fig. 2.1(b). For quartic coupling to the Higgs boson λ_S they read

$$\Delta m_h^2 = \frac{\lambda_S}{16\pi^2} \Lambda^2 + \dots \quad (2.30)$$

Although in above expressions terms depending on the square of the masses of the particles in the loop, also leading to the same problematic behaviour of the Higgs mass, have been omitted, comparing expressions (2.29) and (2.30) serves to illustrate how aforementioned

problem can be solved. As the two contributions have a relative minus sign, they would exactly cancel if for every fermion there were two scalars with $\lambda_S = \lambda_f^2$. This is the case in theories with supersymmetry, leading to systematic cancellation of all terms with problematic behaviour and therefore making it possible for the Higgs mass to be at the electroweak scale, as observed. The terms, which were neglected in both expressions above, are at most logarithmic in Λ . Each of them depends on the square of the considered particle's mass. This places an upper limit on the superpartner masses, which should typically not be much greater than the TeV scale.

Dark Matter

There is a convincing amount of experimental evidence for the existence of non-luminous matter, called dark matter (DM) from astrophysical observations at all astrophysical length scales [21]. One example on the galactic scale is the discrepancy in the form of measured and expected rotation curves of galaxies. These curves describing the orbital velocities of stars and gas as a function of their distance from the galactic center should fall off at larger radii given only the visible mass in the galaxies. Observations however show flat behaviour at large distances, which can be explained by the existence of a DM halo [22].

The total dark matter content in the universe can be inferred from the analysis of anisotropies in the cosmic microwave background (CMB), as e.g. done by the Planck mission [23]. Ordinary matter makes up only about 4.9% of the matter/energy content of the universe, while dark matter constitutes 26.1%. The highest percentage, roughly 69%, corresponds to dark energy, the nature of which is an even bigger puzzle than DM. In principle the Standard Model extended to account for massive neutrinos⁷, would have said neutrinos as candidates for dark matter, but these are ruled out as sole or main component of DM e.g. by measurements of the relic density [21]. Therefore one motivation to consider further extensions of the SM is to have theories with new particles, for which at least one of them has the correct properties to possibly account for the dark matter content in the universe. Candidate particles need to be stable on cosmological time scales, not electromagnetically interacting and they have to yield the correct value of the relic density [25]. A preferred type of DM candidates are Weakly Interacting Massive Particles (WIMPs). In many SUSY models the lightest supersymmetric particle (LSP) is neutral and colourless and its stability is guaranteed by R-parity conservation, a concept introduced in Sec. 2.2.5. Therefore these models contain good WIMP dark matter candidates.

Unification of gauge couplings

In the Standard Model the electromagnetic and weak force are described by the theory of unified electroweak interactions. The goal of grand unified theories (GUT) is to also incorporate the strong interaction in the unification to obtain a theory with a single interaction, based on one non-Abelian gauge group. This larger gauge group, e.g. SU(5), is then thought to be spontaneously broken down at high energies, to yield the low-energy description based on the SM gauge group. The resulting organisation of particles in irreducible representations of the unified gauge group could e.g. explain why electric charges are quantized as observed with fractionally charged quarks yielding protons and neutrons, which in turn form neutral atoms together with electrons.

If the Standard Model is to be extended to such a GUT, the electroweak and strong coupling constants, when evolved with increasing energy, have to become equal at some high-energy

⁷The SM treats neutrinos as massless, but in fact it is known from the observation of neutrino oscillations [24] that at least two of them have to be massive.

scale. As can be seen in Fig. 2.2 this is not the case. In the Minimal Supersymmetric Standard Model, however, the additional particle content at the TeV scale leads to an intersection of the inverse gauge couplings at about 10^{16} GeV.

The possibility of unification makes supersymmetric theories good candidates for physics beyond the SM.

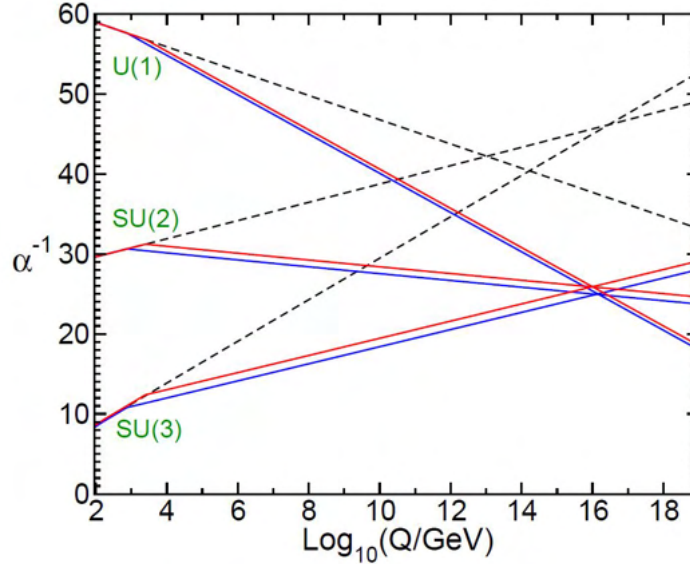


Figure 2.2: Evolution of inverse gauge couplings in the Standard Model (dashed lines) and the MSSM (solid lines). The colours indicate different masses of supersymmetric particles. Figure taken from Ref. [4]

2.2.2 Supersymmetry algebra and supermultiplets

Supersymmetry introduces transformations of bosonic states into fermionic ones and vice versa. One can schematically write this as

$$Q |Boson\rangle = |Fermion\rangle \quad (2.31)$$

$$Q |Fermion\rangle = |Boson\rangle, \quad (2.32)$$

with Q the anticommuting fermionic generator of such transformations. In principle the Coleman-Mandula theorem [26] restricts the symmetry group of a consistent 4-dimensional QFT to consist of the direct product between the Poincaré group, describing space-time transformations and an internal symmetry group. However this theorem is based on the assumption that the generators are commuting and, as stated in the Haag–Lopuszanski–Sohnius extension [27], can thus be evaded if the Poincaré algebra is extended by including anticommuting generators, as in supersymmetry. For a theory, which contains chiral fermions and parity violating interactions, the important part of the algebra relations containing the generators Q and Q^\dagger then has the form

$$\begin{aligned} \{Q, Q^\dagger\} &= P^\mu, \\ \{Q, Q\} &= \{Q^\dagger, Q^\dagger\} = 0, \\ [P^\mu, Q] &= [P^\mu, Q^\dagger] = 0. \end{aligned} \quad (2.33)$$

Here P^μ denotes the four-momentum generator of spacetime translations and spinorial indices have been suppressed.

The particles described by a supersymmetric theory are arranged in irreducible representations of the supersymmetry algebra, which are called supermultiplets. The fermionic and bosonic particles falling into one supermultiplet are usually referred to as superpartners. As the supersymmetry generators commute with the four-momentum generator (see Eq. 2.33), the Casimir invariant of the Poincaré algebra $-P^2 = -P^\mu P_\mu$ is also an invariant in the case of supersymmetry. Therefore the particles in a supermultiplet have the same eigenvalues of $-P^2$, which means they have the same mass. Furthermore particles in the same supermultiplet are also in the same representation of the gauge group and thus their electric charges, weak isospin and properties related to colour charge are also the same. It can be shown that the number of fermionic and bosonic degrees of freedom within a given supermultiplet are equal: $n_F = n_B$.

The first representation needed in order to construct a supersymmetric extension of the SM is called a chiral (or scalar) supermultiplet and contains a Weyl fermion with two degrees of freedom and two bosonic degrees of freedom assembled into a complex scalar⁸. The scalar superpartners of fermions defined in this way are called sfermions. The second relevant representation, the gauge (or vector) supermultiplet, contains a massless spin-1 boson and a Weyl fermion, referred to as a gaugino.

The task, tackled in the next section, is now to accommodate the known SM particles to these supermultiplets. By doing so it also becomes clear which new supersymmetric particles (sparticles) appear. The following section focuses on the Minimal Supersymmetric Standard Model (MSSM), which introduces the minimal amount of such new particles.

2.2.3 Particle content of the MSSM

It is impossible for any of the SM particles to be superpartners of each other, simply due to the fact that they have different values for various quantum numbers, whereas particles in a supermultiplet just differ by spin. Therefore all particles predicted by SUSY really are new, unseen particles.

The quarks and leptons are arranged in chiral supermultiplets together with their bosonic superpartners, the squarks and sleptons and the spin-1 bosons are put in gauge supermultiplets with corresponding gauginos. All the SUSY partners, with their names, notation and spin are listed in Tab. 2.3.

It's important to note that, as the SM treats left- and right-handed fermions differently, these must belong to different supermultiplets and have distinct superpartners. Although the concept of chirality is meaningless for scalar particles the different sfermions are still denoted by \tilde{f}_L and \tilde{f}_R in order to distinguish them.

In order to give masses to u- and d-type quarks via Yukawa couplings and to avoid inconsistencies due to gauge anomalies, in the MSSM one has to introduce two Higgs doublets

$$H_u = \begin{pmatrix} H_u^+ \\ H_u^0 \end{pmatrix}, \quad H_d = \begin{pmatrix} H_d^0 \\ H_d^- \end{pmatrix}. \quad (2.34)$$

The fermionic superpartners of the Higgs scalars are called higgsinos and the corresponding $SU(2)_L$ -doublets have components \tilde{H}_u^+ , \tilde{H}_u^0 , \tilde{H}_d^0 and \tilde{H}_d^- . Spontaneous breaking of electroweak symmetry in the MSSM is complicated by the fact that there exist these two Higgs doublets and can only be fully understood after the concept of supersymmetry breaking is introduced (see Sec. 2.2.4). Irrespective of the detailed form of the scalar potential, both H_u and H_d develop non-zero VEVs, for which their ratio is typically given as $\tan \beta := v_u/v_d$. After electroweak symmetry breaking three of the eight degrees of freedom of the two complex

⁸Unphysical auxiliary fields, necessary to balance the number of degrees of freedom off-shell, are ignored here.

particle	spin	superpartner	spin
quarks q	1/2	squarks \tilde{q}	0
→ top t		stop \tilde{t}	
→ bottom b		sbottom \tilde{b}	
→ charm c		scharm \tilde{c}	
→ strange s		sstrange \tilde{s}	
→ up u		sup \tilde{u}	
→ down d		sdown \tilde{d}	
leptons ℓ	1/2	sleptons $\tilde{\ell}$	0
→ electron e		selectron \tilde{e}	
→ muon μ		smuon $\tilde{\mu}$	
→ tau τ		stau $\tilde{\tau}$	
→ neutrinos ν_ℓ		sneutrino $\tilde{\nu}_\ell$	
gauge bosons	1	gauginos	1/2
→ boson B		Bino \tilde{B}	
→ boson W		Wino \tilde{W}	
→ gluon g		gluino \tilde{g}	
Higgs bosons $H_i^{\pm,0}$	0	higgsinos $\tilde{H}_i^{\pm,0}$	1/2

Table 2.3: Particle content of the MSSM, adapted from Ref. [5]. The first and second row labelled spin show the spin of the particles and the corresponding superpartners respectively.

Higgs doublets become the longitudinal modes of the Z^0 and W^\pm bosons. The remaining degrees of freedom lead to the appearance of five physical Higgs bosons in the MSSM: two CP-even, neutral scalars h^0 and H^0 , one CP-odd, neutral scalar A^0 and two conjugate scalars H^\pm with charge ± 1 . Model-building experiences have shown, that sensible models can be obtained, where h^0 behaves nearly indistinguishable from the Higgs boson in the SM and therefore these two particles are identified in those cases [4].

Due to electroweak symmetry breaking the superpartners of the Higgs degrees of freedom and the electroweak gauge bosons mix to form electroweakinos. More precisely the neutral higgsinos (\tilde{H}_u^0 and \tilde{H}_d^0) and the Bino and neutral Wino yield mass eigenstates called neutralinos. These are typically denoted by $\tilde{\chi}_1^0, \tilde{\chi}_2^0, \tilde{\chi}_3^0$ and $\tilde{\chi}_4^0$, conventionally labeled in ascending mass order. The charged higgsinos and Winos mix to form charginos with charge ± 1 , referred to as $\tilde{\chi}_1^\pm$ and $\tilde{\chi}_2^\pm$, where the latter again has higher mass. While there is also mixing within the squarks and sleptons, the gluino is the only sparticle that can not mix, because of it being the only colour octet fermion.

2.2.4 Supersymmetry breaking

As a consequence of the way supersymmetric particles were introduced in Sec. 2.2.2 they would all have to have masses equal to their SM counterparts. If that were true then they would have already been discovered, which is not the case. Therefore SUSY has to be a broken symmetry, allowing the superpartners to have different masses. One important constraint on how supersymmetry is broken is given by the hierarchy problem, introduced in Sec. 2.2.1 as a main motivation to consider supersymmetric theories. In unbroken SUSY the introduced particles and associated dimensionless couplings are exactly such that problematic contributions to the Higgs mass-squared cancel. If that is supposed to still hold in the presence of supersymmetry breaking the relations between couplings have to be maintained. Such a breaking of SUSY is called soft supersymmetry breaking and can be described by writing the

Lagrangian in the form

$$\mathcal{L} = \mathcal{L}_{\text{SUSY}} + \mathcal{L}_{\text{soft}}, \quad (2.35)$$

where $\mathcal{L}_{\text{SUSY}}$ is SUSY invariant, while the terms in $\mathcal{L}_{\text{soft}}$ violate supersymmetry but feature only couplings with positive mass dimension.

In the MSSM the supersymmetry breaking Lagrangian $\mathcal{L}_{\text{soft}}$ in its most general form introduces a total of 105 new free parameters, not related to any parameters in the SM. Many of these are related to flavour mixing or CP violating processes, which are heavily constrained by experiments [14]. These and other experimental constraints justify the introduction of SUSY models with additional assumptions restricting the space of free parameters [28]. One of these constrained models, namely the phenomenological MSSM (pMSSM) is introduced in Sec. 2.2.6.

2.2.5 R-parity

In principle it is possible for the Lagrangian of a supersymmetric theory to contain terms that violate the conservation of Lepton number (L) and/or Baryon number (B). Corresponding L- and B-violating processes have not been observed experimentally. One example for this is the non-observation of proton decay via $p \rightarrow e^+ \pi^0$, which implies a lower limit for the proton lifetime of roughly 10^{34} years [29].

These terms are avoided in the MSSM by introducing a new symmetry and conserved quantity, called R-parity, which is a multiplicatively conserved quantum number given by a combination of lepton number, baryon number and spin s :

$$P_R = (-1)^{3(B-L)+2s}. \quad (2.36)$$

According to this expression, the SM particles and Higgs bosons are assigned even R-parity ($P_R = +1$), while the superpartners have odd R-parity ($P_R = -1$). R-parity conservation at each vertex has important phenomenological consequences:

- Sparticles are produced in even numbers (usually in pairs).
- A sparticle decays into an odd number of other lighter sparticles (usually only one).
- As a consequence the lightest supersymmetric particle (LSP) must be stable.

If the LSP is electrically neutral and only weakly interacting with ordinary matter it is a candidate for dark matter, as introduced in Sec. 2.2.1. The lightest neutralino χ_1^0 is the most promising DM candidate in the MSSM as it typically is the LSP and fulfills the necessary criteria.

2.2.6 The phenomenological MSSM

As discussed previously the MSSM introduces 105 new free parameters. Apart from the fact that many of these lead to phenomenologically problematic models for generic parameter values, the high number of parameters makes experimental analyses of the MSSM basically impossible. Therefore, as already anticipated, it is reasonable to employ assumptions based on phenomenological constraints in order to constrain the parameter space. By doing this one obtains the pMSSM [28, 30], which has then only 19 free parameters, listed in Tab. 2.4.

The particular constraints, applied to restrict the parameter space are:

- No new source of CP-violation in addition to the CKM matrix. This is achieved by assuming that all phases in the soft-SUSY breaking terms are zero.

pMSSM parameters	
$\tan \beta$	ratio of the VEVs of the two Higgs doublets
M_A	mass of the pseudoscalar Higgs boson
μ	Higgs-higgsino mass parameter
M_1, M_2, M_3	wino, bino and gluino mass parameters
$m_{\tilde{q}}, m_{\tilde{u}_R}, m_{\tilde{d}_R}, m_{\tilde{\ell}}, m_{\tilde{e}_R}$	first and second generation sfermion masses
$m_{\tilde{Q}}, m_{\tilde{t}_R}, m_{\tilde{b}_R}, m_{\tilde{L}}, m_{\tilde{\tau}_R}$	third generation sfermion masses
A_t, A_b, A_τ	trilinear couplings of the third generation sfermions

Table 2.4: Parameters of the phenomenological Minimal Supersymmetric Standard Model (pMSSM).

- The matrices for sfermion masses and trilinear couplings are diagonal. This prohibits the existence of flavour changing neutral currents (FCNCs) at tree level.
- The masses for the first and second generation of sfermions are degenerate. The trilinear couplings between sfermions and Higgs bosons are set to zero for the first and second generation. This is justified by the fact that they always get multiplied by fermion masses, which are negligibly small for the first two generations.

In this framework it is then possible to perform scans of the parameter space and compare to experimental data, even more so if one focuses on a particular sector of the theory. The following work is going to focus on the electroweak sector or more precisely on electroweakinos.

2.2.7 Simplified models

Searches for SUSY with ATLAS are mainly designed based on and interpreted in simplified models [14, 31]. Such models take into account only a very limited set of sparticle production and decay modes, leading to usually one specific fixed decay chain featuring typically two or three SUSY particles. All other sparticles are assumed to be decoupled and play no role. The branching ratios of decays of participating sparticles are often set to 100%. Simplified models replace the huge parameter space of complete SUSY scenarios with a small set of model parameters, in most cases only the masses of the participating sparticles, which can be varied freely. In practice, the model space spanned by the mass parameters is scanned using a set of discrete signal or model points defined by their corresponding mass values, referred to as a signal grid.

If no excess above the Standard Model expectation is found in a search, regions within the parameter space of the simplified model, which are incompatible with the experimental observation, are determined. These experimental bounds are typically presented as exclusion limits in planes spanned by the masses of the involved supersymmetric particles.

Simplified models are a very appealing framework for SUSY searches, because they feature much fewer parameters compared to more complete supersymmetric models and offer the possibility to conduct comprehensive studies of individual SUSY topologies in a straightforward and convenient way. If simplified models are a reasonable approximation of more complete scenarios, they can be used to explore sizeable amounts of the parameter space of these more complete models, but one has to keep in mind that exclusion limits obtained in simplified models are a priori only valid in the corresponding limited scope. Depending on the specific case, simplified model limits can differ significantly from the true underlying constraints on sparticle masses in more complete SUSY models. Oftentimes the exclusion in terms of the sparticle masses is overestimated, especially when the simplified model assumes branching fractions of 100%, which is usually not the case in more complex SUSY models (see e.g. [32]).

Chapter 3

Experiment

One of the most important laboratories for experiments in particle physics is CERN [33]. The CERN laboratory, located at the Franco-Swiss border near Geneva, comprises several particle accelerators and detectors. It was founded in 1954 and nowadays has 23 member states [33]. Its infrastructure and the produced data serve as a basis for the research programme of 11400 scientists working for institutes in 76 countries, as of December 2020 [33].

The following chapter gives an outline of the Large Hadron Collider (LHC) and the ATLAS experiment, within which the research efforts presented in this work are conducted. The first part on the LHC is mostly based on Ref. [34], in which a much more detailed description of the collider can be found.

3.1 The Large Hadron Collider

The LHC, installed in a circular tunnel with a circumference of 26.7 km at depths between 45 m and 170 m, is the largest particle accelerator at CERN. Its main purpose is to accelerate and collide counter-rotating proton beams¹ with a maximal design centre-of-mass energy of $\sqrt{s} = 14$ TeV, i.e. 7 TeV per beam. Following the geometry of the tunnel, originally designed and constructed for the Large Electron Positron Collider (LEP), the LHC consists of eight straight sections and eight arcs. Four of the straight sections have beam crossings and are used for the insertion of detectors. The other four are used for hardware necessary for the operation of the collider.

Before it is injected into the LHC the proton beam is accelerated by passing through a sequence of smaller machines of the CERN accelerator complex, depicted in Fig. 3.1. The pre-accelerator chain starts with the linear accelerator Linac2² and is followed by the PS Booster, the Proton Synchrotron (PS) and the Super Proton Synchrotron (SPS). Each machine in the chain raises the energy of the protons, which are then injected into the LHC with an energy of 450 GeV and further accelerated to the final beam energy. The acceleration of the particles is achieved by using radio frequency cavities. The traversed accelerators also serve the purpose of tuning the beam parameters as needed or desired for the LHC. At extraction from the PS for example the protons in the beam are grouped in bunches of roughly 10^{11} protons with a bunch spacing of approximately 25 ns. Each beam in the LHC contains 2808 of these bunches.

In order to keep the protons on their circular trajectory around the ring 1232 superconducting dipole electromagnets are installed in the arc regions of the LHC. The superconducting coils are cooled down to 1.9 K by superfluid helium and produce a magnetic field with a field

¹In addition to that the LHC is also used as a collider for heavy ions.

²Linac2 was replaced in 2020 by Linac4 [36], as already shown in Fig. 3.1.

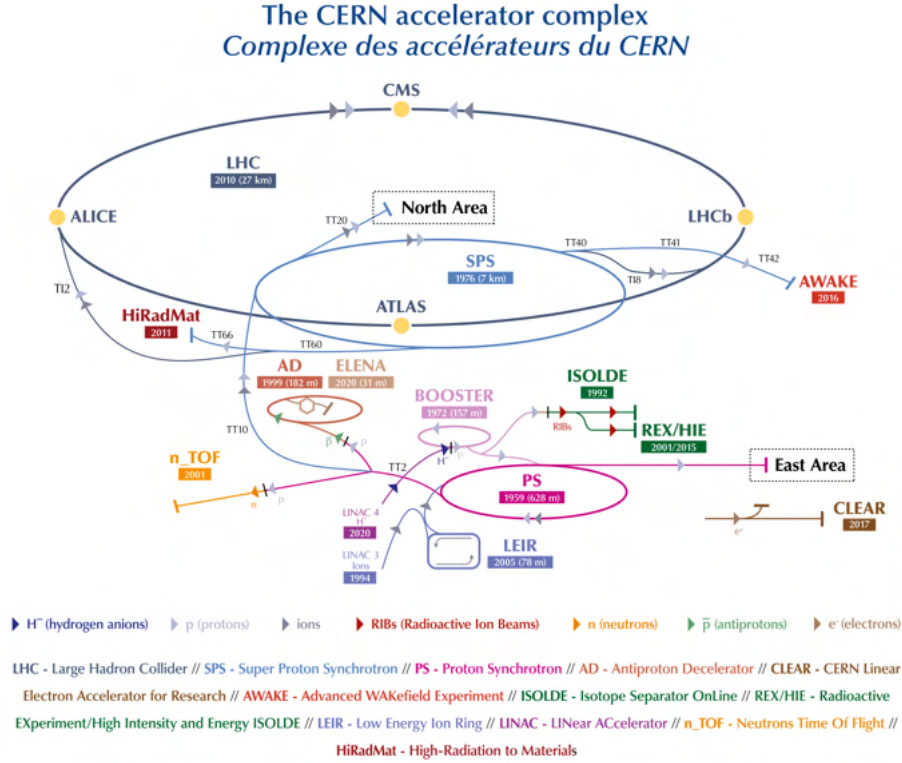


Figure 3.1: The CERN accelerator complex [35].

strength of 8.3 T. The peak value of the dipole field strength is a limiting factor for the maximum beam energy, that can be reached by the LHC. Additional quadrupole and multipole magnets are used to focus the beams and correct their trajectory.

The LHC is used for four main experiments with dedicated detectors: ATLAS [37], CMS [38], ALICE [39] and LHCb [40]. The first two are general purpose detectors used e.g. in order to search for and perform measurements of the Higgs boson and search for BSM physics. ALICE is a detector primarily designed for heavy-ion collisions probing the physics of strongly interacting matter and the quark-gluon plasma at high energies. By performing measurements of CP violation and of rare decays of b- and c-hadrons, LHCb searches for BSM physics responsible for the asymmetry of matter and antimatter in the universe. In addition to the main experiments, several smaller ones are conducted with the LHC. TOTEM [41] studies elastic and diffractive scattering, LHCf [42] is designed for measurements on particles in the very forward region and MoEDAL [43] mainly searches for magnetic monopoles. FASER [44], which started measurements in 2021, is the most recent experiment at the LHC and is dedicated to searching for light, extremely weakly-interacting particles.

Luminosity of the LHC and data-taking with ATLAS

The instantaneous luminosity L_{inst} a collider provides is the most important quantity, besides the beam energy [45]. For a proton-proton collider with Gaussian beam shape it is given in terms of the beam parameters as

$$L_{\text{inst}} = \frac{f_{\text{rev}} n_b N_p^2}{4\pi\sigma_x\sigma_y} \cdot F(\theta_c, \sigma_x, \sigma_z). \quad (3.1)$$

Here f_{rev} is the revolution frequency of a proton bunch, n_b the number of proton bunches in the machine and N_p the number of protons per bunch. The parameters $\sigma_{x,y}$ are the transverse

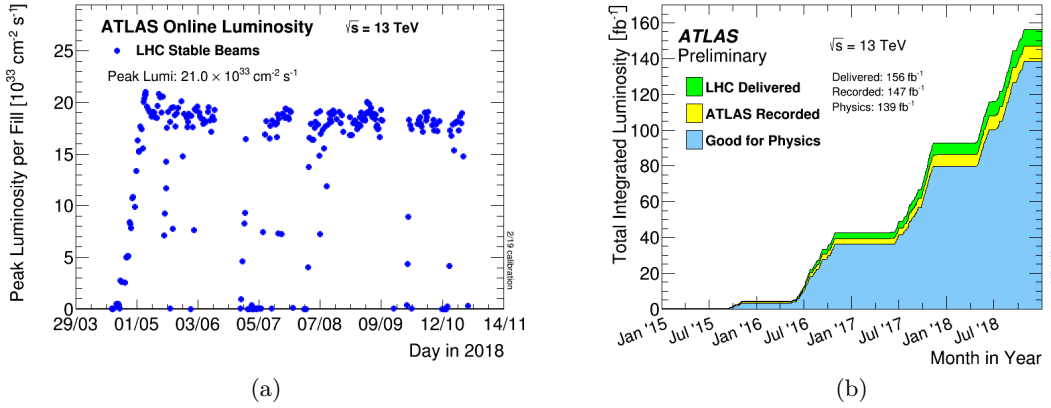


Figure 3.2: (a) Peak instantaneous luminosity delivered to ATLAS by the LHC in the course of 2018 and (b) the cumulative luminosity for the second data-taking period [50].

beam width and F is a correction factor, taking into account the reduction in luminosity due to the angle θ_c between the beams at the collision point.

Using the integrated luminosity L the number of observed events for a particular process with cross section σ under study can be calculated as

$$N_{\text{events}}^{\text{obs}} = \sigma \cdot \epsilon \cdot L = \sigma \cdot \epsilon \cdot \int L_{\text{inst}} dt, \quad (3.2)$$

where ϵ is the detection efficiency of the corresponding experiment. From this it is clear that luminosity is an important factor when it comes to obtaining event counts of statistical significance when observing processes with low cross sections.

The first data-taking period of the LHC from late 2009 to 2013 is referred to as Run 1. During this time period the LHC reached a center-of-mass energy for proton-proton collisions of 7 TeV in 2010 and 2011 and an energy of 8 TeV in 2012, where it delivered a peak instantaneous luminosity of $L_{\text{peak}} = 7.7 \cdot 10^{33} \text{ cm}^{-2} \text{ s}^{-1}$ and integrated luminosity of 22.7 fb^{-1} to ATLAS [46, 47]. In Run 2, which started in 2015 and ended in 2018, the LHC reached values of instantaneous luminosity for proton beams with $\sqrt{s} = 13 \text{ TeV}$ about twice as high as the design value of $L_{\text{inst}} = 10^{34} \text{ cm}^{-2} \text{ s}^{-1}$ (see Fig. 3.2(a)) [48, 49]. As can be seen in Fig. 3.2(b), of the integrated luminosity of 156 fb^{-1} delivered by the LHC during Run 2, collision data corresponding to 139 fb^{-1} were collected by the ATLAS detector and used for physics analyses.

The instantaneous luminosity of the LHC is measured by dedicated detectors, which are calibrated during specific low-intensity LHC fills [45]. An accurate measurement of the luminosity is important for physics analyses, e.g. for the evaluation of SM background levels and determining the sensitivity to new processes in BSM studies [46].

3.2 The ATLAS Experiment

ATLAS (A Toroidal LHC ApparatuS) [37] is a general purpose detector designed to collect data used for research on a broad range of topics, e.g. the search for and measurements of the SM Higgs boson, precision tests of the SM and searches for hints on BSM physics, enabled by the high energy and luminosity of the LHC. Goals in terms of physics and the experimental conditions at the LHC translate to demands on the design of the ATLAS detector [37, 51], e.g.:

- The fact that the LHC collides proton bunches, containing a high number of protons,

with a small time interval in between bunch-crossings, leads to a phenomenon referred to as pile-up. This means that the scattering events one is interested in are accompanied by a number of undesired pp collisions. A fast detector response and high spatial resolutions help mitigate this problem.

- The detector and its electronics have to withstand high levels of radiation coming mostly from collisions at the interaction point.
- In order to separate rare processes from the very dominant QCD background of proton-proton collisions, a good lepton identification and measurement is needed.
- Measurements of particle energies with a coverage of almost the full solid angle are necessary for an accurate determination of missing transverse energy E_T^{miss} , important in particular for SUSY particle searches.

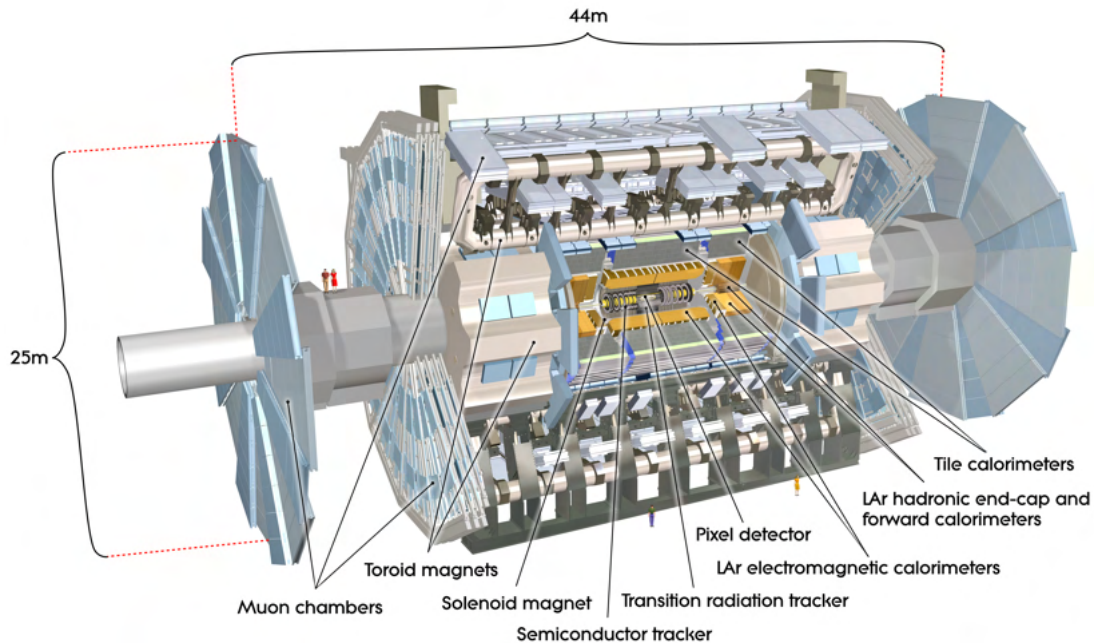


Figure 3.3: Computer generated image of the ATLAS detector, showing the general structure and subsystems [52].

Fig. 3.3 shows a computer generated view of the 44 m long and 25 m high ATLAS detector and its interior composition [37]. The design of ATLAS is to a large extent determined by the magnet system [37], generating a magnetic field, necessary to determine the momenta of particles by the form of their trajectories within the field [51]. The magnet configuration consists of a thin superconducting solenoid surrounding the inner detector and three large superconducting toroids, one for the middle part, called barrel and two for the end-caps.

The following sections give an introduction to the different components of the ATLAS detector, starting from the inner detector closest to the beam pipe, followed by the calorimeters and the muon spectrometer as the outermost subsystem of the barrel and in the end-caps. The information specific to the ATLAS detector presented throughout this part, including the values of design parameters, is taken from Ref. [37], if not indicated otherwise. Information on detector technology in general can be found in [3].

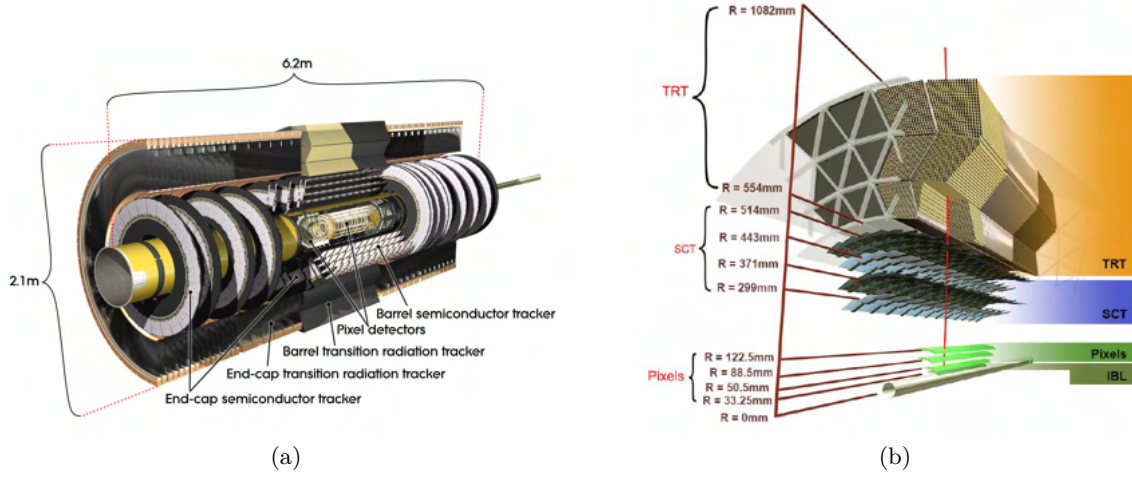


Figure 3.4: (a) Computer generated cut-away view of the inner detector [53] and (b) the different layers of the inner detector in the barrel, including the IBL [54].

3.2.1 Coordinate system

In order to describe the particles resulting from collision events and features of detector systems, a suitable coordinate system for the ATLAS detector has to be introduced. The nominal interaction point is taken as the origin of a right-handed coordinate system, in which the beam direction corresponds to the z -axis. In the x - y -plane transverse to the beam direction the x -axis is defined to point from the interaction point to the center of the LHC ring and the y -axis points upwards. In addition spherical coordinates with the azimuthal angle ϕ around the beam axis and the polar angle θ from the beam axis are introduced.

Pseudorapidity [14] η is a commonly used variable related to the angle θ . It is given by

$$\eta = -\ln\left(\tan\frac{\theta}{2}\right) \quad (3.3)$$

and is approximately equal to the rapidity

$$y = \frac{1}{2} \ln\left(\frac{E + p_z}{E - p_z}\right) \quad (3.4)$$

in the high-energy limit where $p \gg m$ and $\theta \gg 1/\gamma$. Both these variables are useful, because differences in the variables $\Delta\eta$ and Δy and therefore also differences

$$\Delta R = \sqrt{(\Delta\eta)^2 + (\Delta\phi)^2} \quad \text{and} \quad \Delta R_y = \sqrt{(\Delta y)^2 + (\Delta\phi)^2} \quad (3.5)$$

are invariant under Lorentz boosts in z -direction³. Pseudorapidity has the advantage, that it can be determined even if the mass and momentum of the particle are unknown. The direction along the beam axis corresponds to a pseudorapidity $\eta = \infty$ and directions in the transverse plane have $\eta = 0$.

3.2.2 Inner detector

The main purpose of the inner detector is to record the tracks of charged particles in the 2 T magnetic field generated by the surrounding solenoid in order to determine their momenta

³For $\Delta\eta$ this assumes the massless limit.

and to reconstruct interaction vertices. It consists of three different subsystems. Fig. 3.4 shows the overall structure of the detector and its components.

In the original design of ATLAS the first component closest to the beam pipe featured three silicon pixel layers, with pixel sizes of typically $50\ \mu\text{m} \times 400\ \mu\text{m}$ arranged concentrically around the beam axis in the barrel and on perpendicular discs in the end-caps. Semiconductor-based pixel detectors are used as the innermost component, because they offer the highest spatial resolution, while being able to withstand the high-radiation environment. Before Run 2 an additional pixel layer, called Insertable B-Layer (IBL) [55, 56] was installed, in order to improve or at least maintain the durability and performance of the ATLAS tracking system in view of the raised luminosity of the LHC. The accuracies of the pixel tracking detectors are $10\ \mu\text{m}$ in $R\text{-}\phi$ and $115\ \mu\text{m}$ in z for the barrel and $10\ \mu\text{m}$ in $R\text{-}\phi$ and $115\ \mu\text{m}$ in R for the end-caps.

The second component of the inner detector is the silicon microstrip tracker (SCT), which comprises four double-layers of strips in the barrel and nine disc double-layers in each of the end-caps. The strips in each double-layer are arranged in such a way as to provide information on both space coordinates, e.g. in the barrel one set of strips is aligned parallel to the beam axis and the SCT measures the values of $R\text{-}\phi$ and z of four points, in which tracks of charged particles cross the strip layers. The intrinsic precisions are $17\ \mu\text{m}$ in $R\text{-}\phi$ and $580\ \mu\text{m}$ in z and R respectively. Both the pixel detector and the SCT cover a region with pseudorapidities $|\eta| < 2.5$.

The transition radiation tracker (TRT) is the outermost and largest subsystem of the inner detector. It consists of straw tubes with a diameter of 4 mm filled with a Xe-based gas mixture. A coating on the inside of the tubes serves as a cathode and a wire, supported at the straw end and center, as an anode. This allows for particle tracking by reading out the electric signal produced through ionisation of the gas filling due to traversing charged particles. While in the barrel region 144 cm long tubes are arranged in 73 layers parallel to the beam axis, in the end-caps the TRT consists of 160 layers of 37 cm long tubes aligned in radial direction. The straw tubes are interleaved with fibres and foils causing traversing particles to emit transition radiation, which is then absorbed in the gas filling, producing an electric signal. This can be used for the identification of electrons, because the intensity of emitted radiation depends on the corresponding particle mass. The TRT provides tracking information in $R\text{-}\phi$ with an accuracy of $130\ \mu\text{m}$ in a range $|\eta| < 2.0$. The lower resolution compared to the semiconductor trackers is compensated by a high amount of hits and longer measured track length.

3.2.3 Calorimeters

To measure the energies of particles, the ATLAS detector uses a calorimeter system (see Fig. 3.5), consisting of different subsystems for electromagnetically and strongly interacting particles and for different ranges of pseudorapidity. The thickness of the calorimeter system is dictated by the fact that the energy of the measured particles ideally has to be completely absorbed and punch-through into the surrounding muon system (see Sec. 3.2.4) has to be limited. Both the electromagnetic and hadronic calorimeters of ATLAS are sampling calorimeters, with alternating layers of absorbing and active material. Through interactions with the absorbing material, particles create a number of secondary particles and thereby lose their energy. The resulting cascade of particles is called a shower. In the active medium the generated particles are measured and the deposited energy is determined.

The electromagnetic calorimeter uses lead as absorbing and liquid argon (LAr) as active material. It consist of two identical halves in the barrel and two coaxial wheels in each of the end-caps. Due to the accordion-like shape of its modules, the calorimeter provides

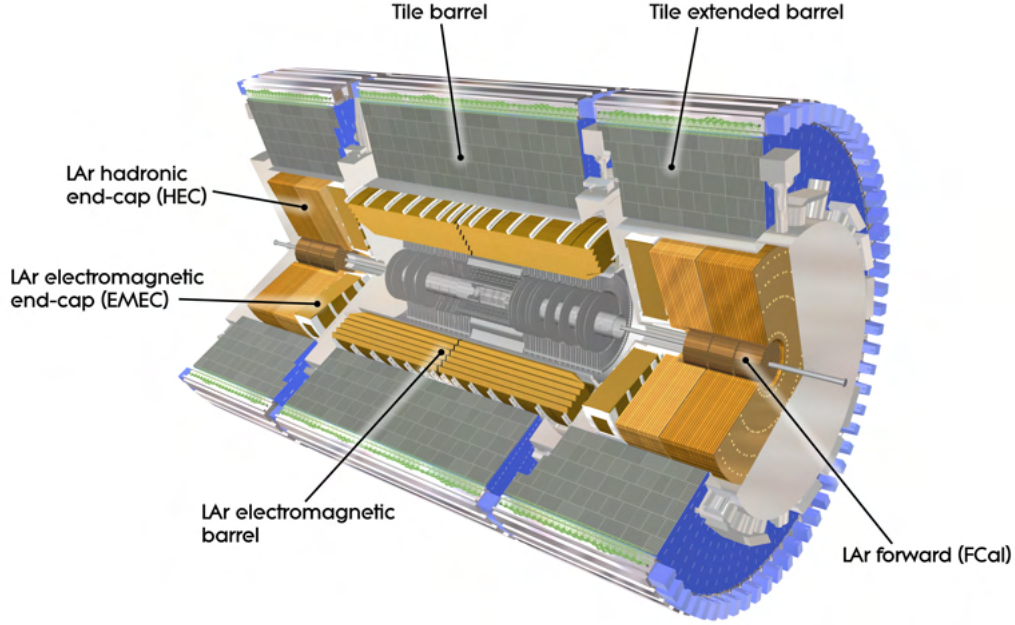


Figure 3.5: Computer generated image of the ATLAS calorimeter systems [57].

full coverage in ϕ . Pseudorapidities up to $|\eta| < 3.2$ are covered, with a finer granularity in the region matched to the inner detector ($|\eta| < 2.5$) in order to achieve high precision measurements. The thickness of the electromagnetic calorimeter is at least 22 radiation lengths⁴ in the barrel region and 24 radiation lengths in the end-caps.

The hadronic calorimeter is located directly outside the electromagnetic calorimeter. While in the barrel component, which has a depth of 7.4 interaction lengths⁵, steel plates and scintillating tiles are used as absorbing and active material respectively, the hadronic end-cap calorimeter wheels feature copper plates interleaved with LAr as active medium.

Both electromagnetic and hadronic calorimetry are extended to higher pseudorapidity values of up to $|\eta| < 4.9$ by the forward calorimeter. It has a thickness of about 10 interaction lengths and consists of three modules in each end-cap, one for the measurement of electromagnetically interacting particles and two for hadronic interactions. While liquid Argon serves again as active material, copper and tungsten are used as absorbers.

3.2.4 Muon spectrometer

The outermost detector component is specifically dedicated to the identification and measurement of muons, which, as minimum ionising particles, pass through the other detector systems. The muon spectrometer is embedded in the magnetic field generated by the barrel and end-cap toroid magnets and allows for momentum measurements in a region $|\eta| < 2.7$. Fig. 3.6 shows an overview of the different components of the muon detector. The tracks of muons are measured in chambers arranged in three layers around the beam axis in the barrel region and three layers perpendicular to the beam in the end-caps. The muon system of

⁴Radiation length [14] describes the mean distance a high-energy electron travels through a material before its energy is decreased to $1/e$ of the initial value by bremsstrahlung, which is the dominant mechanism for a high-energy electron to lose energy in matter.

⁵The hadronic interaction length is the mean distance travelled by a hadronic particle before undergoing an inelastic nuclear interaction.

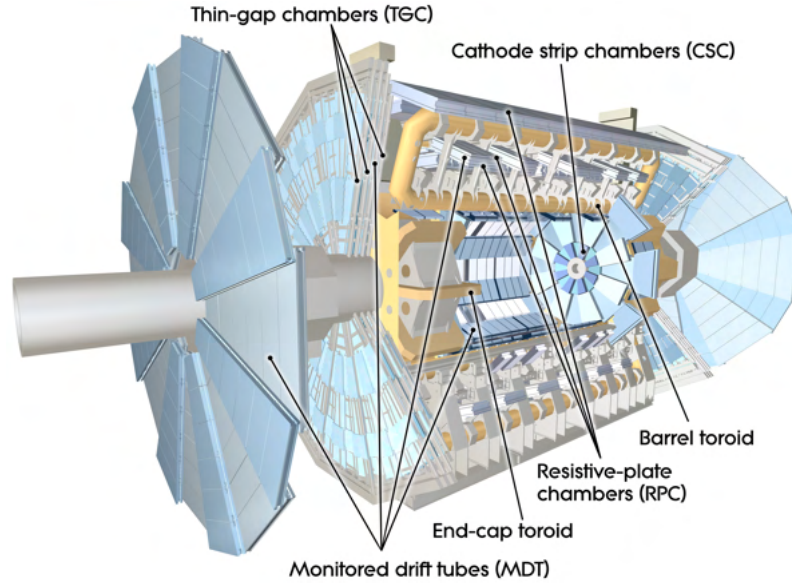


Figure 3.6: Computer generated image showing the different components of the ATLAS muon subsystem [58].

ATLAS is a combination of several different gaseous tracking detectors. The main subsystem used to collect high precision tracking information consists of monitored drift tube (MDT) chambers. One of these chambers comprises up to eight layers of drift tubes with a diameter of 30 mm and has an accuracy of up to $35\ \mu\text{m}$. A wire anode collects the electrons resulting from ionisation of the Ar-based gas mixture induced by traversing particles.

Because of very high particle fluxes, in the forward region $|\eta| > 2.0$ the MDTs in the innermost layer of the end-caps are replaced by cathode strip chambers (CSC), consisting of layers of anode wires enclosed by segmented cathode layers and gas-filled gaps.

Since the MDTs have too high response time for the bunch crossing frequency of the LHC, ATLAS features two systems of triggering chambers assigning detected muons to the correct bunch crossing. Resistive plate chambers (RPC) are used in the barrel part and thin gap chambers (TGC) in the end-caps. In addition, as MDTs measure only the coordinates of tracks in the bending plane, the trigger chambers also serve the purpose of providing the third orthogonal coordinate.

3.2.5 Trigger system and data

The nominal time interval of 25 ns between bunch crossings during proton-proton operation of the LHC corresponds to a bunch crossing rate of 40 MHz. Handling and storing the resulting amount of approximately 60 TB of data per second [45], is impossible due to limited computing resources. In addition, because of low cross sections in comparison to QCD jet production, interesting physics processes occur only rarely and a lot of events can be discarded. The trigger system of ATLAS, which decides whether or not to keep a collision event, consists of a hardware-based first level trigger (L1) [59] and a software-based high level trigger (HLT) [60]. During the LHC shutdown before Run 2 various aspects of the ATLAS trigger system have been upgraded in order to accommodate the higher rates of interesting physics processes [61, 62].

The L1 trigger selects events based on reduced-granularity information from the calorimeters and the trigger chambers of the muon spectrometer. In order to reduce the amount of data, which must be transferred from the detector readout, it also defines Regions-of-Interest (RoI),

i.e. regions in the coordinates η and ϕ , which contain the interesting features identified in the selection process. These regions serve as the basis for the second trigger stage. The L1 trigger has a decision time of $2.5\ \mu\text{s}$, during which the detector information is stored on on-detector memories, and reduces the rate of events to the maximum detector read-out rate of 100 kHz. The HLT uses all detector systems at their full granularity and precision to reduce the rate of events for which data is permanently stored to 1.2 kHz on average, corresponding to 1.2 GB of data per second [61]. The second trigger stage employs a dedicated computing farm to run reconstruction algorithms, typically in a sequence of fast trigger algorithms for early rejection followed by more precise and CPU-intensive ones.

Chapter 4

Searching for electroweakinos with compressed mass spectra

At the LHC, processes producing gluinos and squarks by gluon-gluon and gluon-quark fusion have much higher cross sections and are dominant compared to processes producing charginos and neutralinos [4]. This is illustrated in Fig. 4.1, which shows cross sections of several sparticle production processes. For this reason the SUSY search program at ATLAS (and CMS) is able to place strong constraints on the existence of gluinos and squarks, while limits for the electroweak sector SUSY particles are typically much weaker. Yet, due to the full Run-2 dataset being available and by employing improved analysis strategies and techniques, the limits on electroweakinos and sleptons are constantly improving.

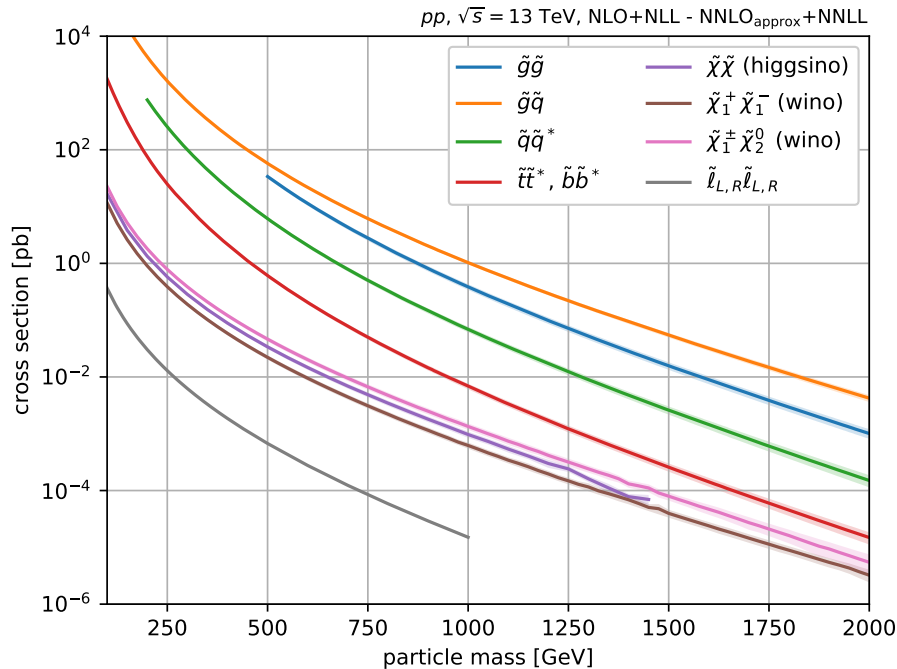


Figure 4.1: Cross sections of different gluino/squark, electroweakino and slepton production processes for pp collisions at $\sqrt{s} = 13$ TeV. Curves corresponding to electroweakino production scenarios lie well below the curves of coloured production processes. The plot is taken from Ref. [63] and uses values based on Refs. [64–66].

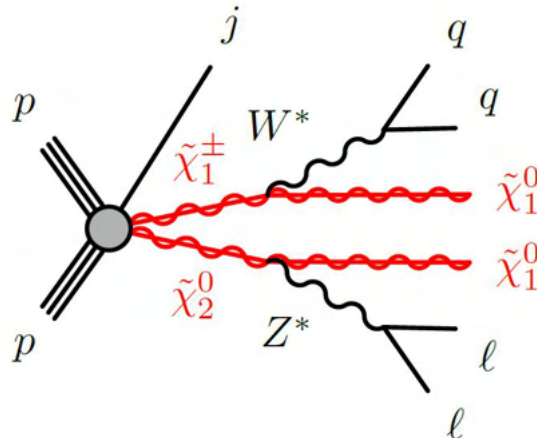


Figure 4.2: Diagram of the simplified model and subsequent decays resulting in a final state with two leptons, multiple jets and E_T^{miss} .

The following sections present a search for electroweakinos [1] in signatures sensitive to models where the considered supersymmetric particles have nearly degenerate mass spectra, in the following referred to as compressed spectra. The newest iteration of the analysis uses 139 fb^{-1} [1] of proton-proton data collected by the ATLAS detector during the Run-2 data-taking period and improved methods to update the previous results obtained for a luminosity of 36.1 fb^{-1} [67]. While the presentation in this work focuses on SUSY scenarios with direct production of electroweakinos, the analysis in principle also considers scenarios with production of electroweakinos through vector-boson fusion (VBF) processes as well as slepton pair production. The analysis is in the following referred to as electroweak compressed analysis.

4.1 Analysis overview and targeted signal scenarios

The analysis targets a final state with two same-flavour leptons (electrons or muons), high missing transverse momentum magnitude (E_T^{miss}) and hadronic activity. The main scenario used to interpret the search results is a simplified model where the lightest chargino decays via $\tilde{\chi}_1^\pm \rightarrow W^* \tilde{\chi}_1^0$ and the next-to-lightest neutralino decays via $\tilde{\chi}_2^0 \rightarrow Z^* \tilde{\chi}_1^0$. Corresponding branching ratios of sparticles are set to 100%. While the subsequent decay of the off-shell W boson (W^*) results in hadronic activity, decays of the off-shell Z boson (Z^*) produce a dilepton pair for which the dilepton invariant mass $m_{\ell\ell}$ is kinematically restricted to be smaller than the mass splitting between the $\tilde{\chi}_2^0$ and $\tilde{\chi}_1^0$. This scenario yielding the targeted final state is illustrated in Fig. 4.2.

One major challenge performing an analysis considering scenarios with highly compressed electroweakino spectra is the reconstruction of particles, in this case electrons and muons, with low momentum. The electroweak compressed analysis uses events with electrons and muons with transverse momentum p_T values as low as 4.5 GeV and 3 GeV, respectively. The sensitivity of the search is enhanced by the requirement of a jet originating from initial-state radiation (ISR), which boosts the entire system, leading to higher values of E_T^{miss} and provides additional kinematic criteria to discriminate against backgrounds.

The phenomenology of electroweakinos is determined by the relations between the MSSM parameters M_1 , M_2 and μ , which are the Bino, Wino and Higgsino mass parameters. Two different scenarios regarding the neutralino/chargino composition and mass relation are considered in the search. The first scenario with parameter relations $|\mu| \ll |M_1|, |M_2|$ is favored

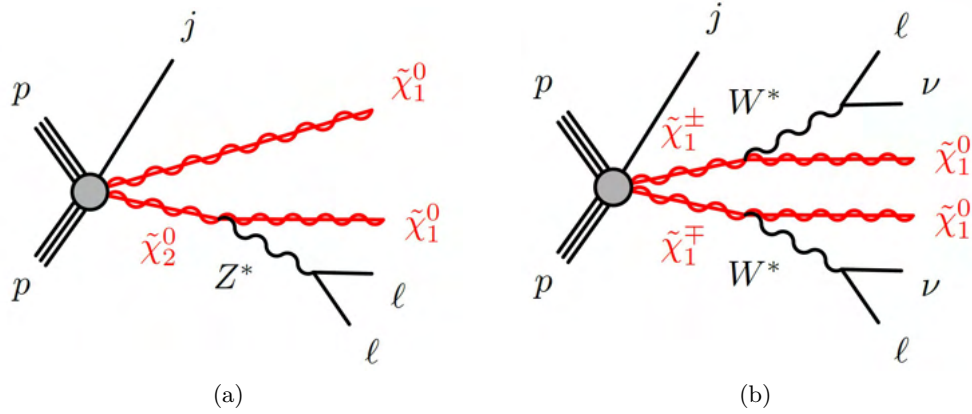


Figure 4.3: Additional processes considered in the Higgsino LSP scenario: (a) Pair production of $\tilde{\chi}_2^0 \tilde{\chi}_1^0$ with the $\tilde{\chi}_2^0$ decaying via $\tilde{\chi}_2^0 \rightarrow (Z^* \rightarrow \ell\ell)\tilde{\chi}_1^0$, (b) pair Production of $\tilde{\chi}_1^\pm \tilde{\chi}_1^\mp$ with each chargino decaying via $\tilde{\chi}_1^\pm \rightarrow (W^* \rightarrow \ell\nu)\tilde{\chi}_1^0$.

by naturalness arguments [68, 69] and features a Higgsino-dominated triplet of lightest SUSY particles, where the three electroweakino states $\tilde{\chi}_1^0$, $\tilde{\chi}_1^\pm$ and $\tilde{\chi}_2^0$ are almost mass degenerate. More specifically, it is possible for the differences between the masses of the lightest electroweakinos to range from hundreds of MeV to tens of GeV depending on the composition of the mass eigenstates determined by the values of M_1 and M_2 .

In this scenario, where the LSP is Higgsino-like, additional processes with $\tilde{\chi}_2^0 \tilde{\chi}_1^0$ and $\tilde{\chi}_1^\pm \tilde{\chi}_1^\mp$ production, depicted in Fig. 4.3 are taken into account. However since the analysis exploits the kinematic endpoint in the $m_{\ell\ell}$ distribution of the leptons from the decay of the off-shell Z boson, processes involving the production of a $\tilde{\chi}_2^0$ are more important for the sensitivity of the search.

The masses of the lightest and second-to-lightest neutralino $m(\tilde{\chi}_1^0)$ and $m(\tilde{\chi}_2^0)$ are systematically varied forming a two-dimensional signal grid evaluated by the analysis. LSP masses from 60 GeV to 300 GeV are considered with an interval of 25 GeV between most signal points. The values of the mass difference $\Delta m = m(\tilde{\chi}_2^0) - m(\tilde{\chi}_1^0)$ lie in the range from 1.5 GeV to 60 GeV with a higher density of points in the region of small mass splittings. The chargino mass $m(\tilde{\chi}_1^\pm) = \frac{1}{2} [m(\tilde{\chi}_1^0) + m(\tilde{\chi}_2^0)]$ is set to be halfway between the two neutralinos.

The cross sections used to scale the signal samples are calculated with RESUMMINO [70] assuming non-degenerate pure Higgsino lightest neutralinos and chargino. The signal samples are generated with MADGRAPH5_AMC@NLO [71, 72] and the parton showering is simulated with PYTHIA8 [73]. For each process the emission of at least one additional parton with $p_T > 50$ GeV is required in order to enforce the targeted ISR topology. The electroweakinos are decayed with MADSPIN [74] and the leptonic branching ratios of the off-shell gauge bosons Z^* and W^* are computed with SUSY-HIT [75]. The branching ratios increase with higher values of the mass splitting Δm . The fast ATLAS detector simulation ATLFast-II [76] is used for the signal samples. This allows for a faster processing by describing the response of the calorimeters to traversing particles by pre-determined parametrizations of electromagnetic and hadronic showers. The full detector simulation with GEANT4 [77] is then only used for the inner detector and the muon spectrometer.

As a second scenario the analysis considers a compressed electroweakino spectrum with a Bino-like $\tilde{\chi}_1^0$ and mass degenerate Wino-like $\tilde{\chi}_2^0$ and $\tilde{\chi}_1^\pm$ corresponding to parameter relations $|M_1| < |M_2| \ll |\mu|$. Such a scenario is motivated by the possibility for the LSP to be a candidate for DM which is compatible with the observed relic density as a result of coannihilation processes in the early universe [78, 79]. The configuration for the generation of signal samples is analog to the one for the Higgsino scenario.

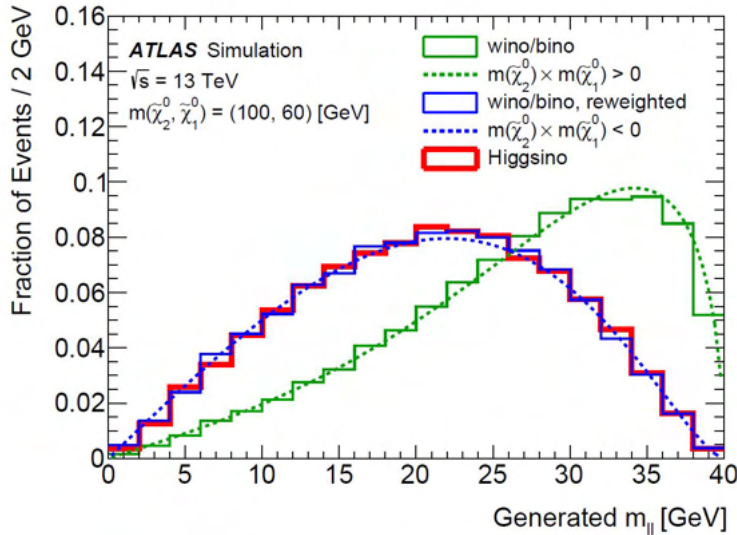


Figure 4.4: Analytical lineshapes and simulated distributions of the dilepton invariant mass for Higgsino and Wino/Bino models. The analytical curve is used to reweight the Wino/Bino distributions to the case where $m(\tilde{\chi}_2^0) \times m(\tilde{\chi}_1^0) < 0$. The agreement of the reweighted distribution and the expected lineshape is shown. Plot taken from Ref. [1].

In a Wino/Bino model the product of the mass eigenvalues of the two lightest neutralinos $m(\tilde{\chi}_2^0) \times m(\tilde{\chi}_1^0)$ can be positive or negative¹ and this relative sign determines the distribution of the dilepton invariant mass from the decay of the virtual Z^* . The processes generated in the Wino/Bino scenario assume the product to be positive yielding a $m_{\ell\ell}$ distribution like the green curve in Fig. 4.4. In the case of a Higgsino LSP only a negative relative sign is possible and the distribution will look like the one shown in red in Fig. 4.4. An analytical description of the lineshapes can be used to reweight the distribution of the Wino/Bino samples to the case where $m(\tilde{\chi}_2^0) \times m(\tilde{\chi}_1^0) < 0$. This introduces two different signal scenarios with a Wino-like NLSP and Bino-like LSP, which are used to provide separate interpretations of the search results.

4.2 Object definitions and event reconstruction

The information gathered by the various components of the detector is used to reconstruct and identify physics objects based on certain criteria and definitions. The goal is to minimize the amount of falsely reconstructed or misidentified objects as well as the number of missed objects not reconstructed at all. Leptons (electrons and muons) and jets are first defined by a set of loose baseline requirements followed by a refinement of their identification through more stringent signal identification criteria. Baseline objects are more prone to reconstruction errors but have a higher acceptance and are therefore used for e.g. the reconstruction of the missing transverse momentum. In the analysis mostly signal objects fulfilling the signal identification criteria are used. Baseline objects are used in the overlap removal, see Sec. 4.3.

Candidate events are preselected by requiring at least one interaction vertex with two associated tracks of charged particles. The reconstruction of tracks [81, 82] employs data recorded with the pixel, SCT and TRT detectors. The vertex position is determined from the resulting set of tracks [83, 84]. If multiple vertices are reconstructed, the one with the highest $\sum p_T^2$ of associated tracks is defined as the primary vertex.

Event cleaning criteria [85] are applied in order to filter out events with detector noise or

¹This is due to the way the mixing matrix is diagonalized, see e.g. Ref. [80].

backgrounds from non-collision sources, e.g. from cosmic rays.

4.2.1 Electrons

The reconstruction of electrons [86] is achieved by an algorithm, which starts by forming clusters [87] of calorimeter cells, which registered an energy deposit above a certain threshold. In the second step the obtained clusters are loosely matched to particle tracks from the inner detector. The previous clustering is subsequently adjusted, e.g. to allow for the treatment of the effects of bremsstrahlung, after which electrons are identified as pairs of a refined cluster and matching track. A likelihood-based discriminant is used to identify and distinguish prompt electrons from non-prompt electrons coming from decays of heavy flavour (HF) hadrons or photon conversions and fake electrons appearing due to the misidentification of jets. The inputs to this likelihood are quantities measured by the tracking and calorimeter systems. Based on fixed threshold values of the discriminant, different working points referred to as *VeryLoose*, *Loose*, *Medium* and *Tight* [86] are defined in order to meet the different requirements of physics analyses. Starting from *VeryLoose*, the working points have decreasing identification efficiency and increasing purity.

In the electroweak compressed analysis electrons are required to have $p_T > 4.5 \text{ GeV}$ and $|\eta| < 2.47$. Baseline electrons are defined by the *VeryLoose* likelihood requirement, which, in contrast to the other working points, does not explicitly contain the requirement of the presence of a hit in the innermost pixel layer and only requires one hit overall in the pixel detector. The longitudinal impact parameter z_0 relative to the primary vertex has to satisfy $|z_0 \sin \theta| < 0.5 \text{ mm}$. Signal electrons are defined by the *Medium* working point identification criteria. To ensure that the electrons originate from the primary vertex the significance of the transverse impact parameter relative to the beam line has to fulfill $|d_0|/\sigma(d_0) < 5$.

Electrons need to satisfy isolation criteria [86] ensuring that there are no additional objects in the region near a reconstructed electron. The aim in a specific physics analysis is to choose the isolation criteria such that a compromise between the identification of prompt electrons and the rejection of electrons from HF decays or light hadrons misidentified as electrons is achieved. The activity in the vicinity of an electron can be quantified by variables related to the tracks of nearby particles and energy deposits in the calorimeter respectively [88]. The track based variable $p_T^{\text{var}20}$ is the sum of track momenta above 1 GeV inside a cone around the electron [88]. The size of the cone shrinks with increasing transverse momentum of the electron. The variable $E_T^{\text{cone}20}$ is the sum of transverse energies in calorimeter clusters with several corrections applied in a cone of fixed size [88].

Electrons in the electroweak compressed analysis are required to satisfy the *Gradient* [86] working point, which requires the two isolation variables to take values such that an isolation efficiency of 90 % at $p_T = 25 \text{ GeV}$ and 99 % at $p_T = 60 \text{ GeV}$ is achieved [86].

4.2.2 Muons

The reconstruction of muons [89] primarily uses tracking information from the inner detector and the muon spectrometer. The process of muon reconstruction starts with the identification of local track segments in the muon spectrometer, which are then combined to track candidates loosely compatible with the interaction point and the parabolic form of a muon trajectory in the magnetic field. The track reconstruction is subsequently refined before the muon spectrometer tracks are combined with tracks in the inner detector by performing a fit, which also takes energy losses in the calorimeters into account. From the reconstructed muon candidates the muon physics objects used by an analysis can be selected through sets

of requirements on, e.g. the number of hits in different subdetector components.

Baseline muons in the analysis considered have $p_T > 3 \text{ GeV}$ and $|\eta| < 2.5$ and correspond to tracks, which satisfy the requirement $|z_0 \sin \theta| < 0.5 \text{ mm}$ on the longitudinal impact parameter. Preselected muons need to pass the requirements of the *LowPt* identification working point, which is specifically designed for analyses targeting muons with very low transverse momentum and is described in more detail in [89]. Signal muons additionally need to satisfy $|d_0|/\sigma(d_0) < 3$ and isolation criteria according to the *FixedCutTightTrackOnly* [90] working point, which uses only tracking information.

4.2.3 Jets

Due to colour-confinement quarks and gluons cannot exist as free particles and therefore hadronise. This happens in such a way that the newly formed hadrons form a stream of hadrons roughly in the direction of the initiating parton, which can be observed in the detector and is referred to as a jet [3]. Jets can be reconstructed with a number of different jet algorithms. In this work the anti- k_t algorithm [91] is used, which is an infrared and collinear safe and soft-resilient sequential recombination algorithm iteratively combining candidate jet constituents with growing distance until the point where the distance becomes too large. The algorithm uses topological clusters [87] formed based on energy deposits in the calorimeter cells as input. The radius parameter is set to $R = 0.4$. The four-momentum of reconstructed jets is corrected by a calibration procedure described in Ref. [92]. First, jet energy contributions due to pile-up are removed by a data-driven method based on the jet area, then the jets are calibrated. The suppression of pile-up jets is further improved by the jet vertex tagger [93], which is a discriminant based on variables that describe the amount of jet momentum corresponding to tracks associated to the primary vertex.

Baseline jets in the compressed search are required to have $p_T > 20 \text{ GeV}$ and $|\eta| < 4.5$. Preselected jets with $p_T < 120 \text{ GeV}$ and $|\eta| < 2.5$ need to satisfy the *Medium* [94] working point of the jet vertex tagger, while jets with $p_T < 50 \text{ GeV}$ and $|\eta| < 2.5$ are required to pass the *Loose* [94] working point of the forward jet vertex tagger. The signal jets considered in the analysis comprise the subset of baseline jets additionally satisfying $p_T > 30 \text{ GeV}$ and $|\eta| < 2.8$.

4.2.4 B-tagging

Hadrons containing b -quarks have lifetimes on the order of $\mathcal{O}(10^{-12} \text{ s})$ [14]. At the typical momenta this means that they usually travel a distance before decaying such that a displaced secondary vertex can be observed in the detector. This and other properties of b -hadrons can be used to identify jets containing b -hadrons, referred to as b -tagged jets. The strategy developed to identify b -jets [95] features two steps. In the first step a set of low-level algorithms reconstruct the characteristic features of b -jets regarding particle tracks and displaced vertices and the obtained results are then combined in high-level algorithms consisting of multivariate classifiers trained on simulated samples.

In the electroweak compressed analysis the b -tagging is performed by the MV2C10 [95] algorithm using jets with p_T and within $|\eta| < 2.5$ as input. The working point of the b -tagging algorithm is chosen such that it achieves an identification efficiency of 85% in simulated $t\bar{t}$ events.

4.2.5 Tracks

In order to increase the sensitivity of the analysis to electroweakino signals with very low mass splittings, where the lepton p_T can be very low, events with one lepton and an additional track are considered.

Baseline track objects have $p_T > 500 \text{ MeV}$ and $\eta < 2.5$ and are required to satisfy a set of conditions on the numbers of hits in the subsystems of the inner detector according to the *Tight-Primary* working point defined in Ref. [96]. Tracks are matched to electron or muon candidates by the requirement of being within $\Delta R = 0.01$ of an electron or muon, which fails the signal lepton criteria defined above. Tracks with transverse momenta not satisfying $0.8 < p_T^{\text{track}}/p_T^\ell < 1.2$ are discarded. The matching of tracks to lepton candidates reduces contributions from tracks not originating from the targeted leptonic decay of electroweakinos and allows an identification as electron or muon tracks, which is relevant for the definition of the corresponding signal region.

Signal tracks have to satisfy $p_T > 1 \text{ GeV}$, $|z_0 \sin \theta| < 0.5 \text{ mm}$ and $|d_0/\sigma(d_0)| < 3$. The isolation of signal tracks is achieved by requiring that there are no jets within $\Delta R < 0.5$ around a track and that the $\sum p_T$ of other tracks within $\Delta R = 0.3$, excluding those belonging to signal leptons, is less than 0.5 GeV .

4.2.6 Missing transverse momentum

Missing transverse momentum $\mathbf{p}_T^{\text{miss}}$ (with magnitude E_T^{miss}) is an observable that can be used to infer the presence of particles which traverse the detector without being explicitly measured. Assuming that the initial momenta in the transverse plane of the colliding partons are negligible, the sum over the transverse momenta of all objects in a collision should vanish due to momentum conservation. The missing transverse momentum in an event is thus computed as the negative vector sum of the transverse momenta of the reconstructed and calibrated electrons, muons², photons³ and jets as well as a soft term corresponding to tracks not associated to any reconstructed object but compatible with the primary vertex [97, 98]:

$$\mathbf{p}_T^{\text{miss}} = - \sum \mathbf{p}_T^e - \sum \mathbf{p}_T^\mu - \sum \mathbf{p}_T^\gamma - \sum \mathbf{p}_T^{\text{jet}} - \sum \mathbf{p}_T^{\text{track}}. \quad (4.1)$$

The calculation of the missing transverse momentum uses the baseline objects defined in the previous sections and features an overlap removal procedure (different to what is introduced in Sec. 4.3) in order to prevent multiple inclusions of the same signal.

Different working points putting constraints on the jets included in the E_T^{miss} calculation are available. In the search considered in this work the *Tight* [98] working point, which is designed to reduce the effects of pile-up, is used. This removes forward jets in the region with $|\eta| > 2.4$ and $20 < p_T < 30 \text{ GeV}$, which contains a high number of pile-up jets.

4.3 Overlap removal

The reconstruction of physics objects is performed independently for the different types of objects and it is therefore possible that tracks or calorimeter energy deposits are used more than once and identified as different objects. In order to resolve ambiguities and prevent possible double-counting an overlap removal procedure is carried out for the baseline objects

²Explicit contributions by τ -leptons are omitted here as they are not specifically treated in the analysis. They are implicitly included by contributions to the electron, muon and jet terms.

³Photons are reconstructed similarly to electrons [88]. In the search considered here they are only relevant in the calculation of E_T^{miss} .

defined by the analysis. The procedure features sequentially executed steps using the sharing of tracks and the distance measure $\Delta R_y = \sqrt{(\Delta y)^2 + (\Delta\phi)^2}$. Based on recommendations in Ref. [99] the following steps are performed:

1. Electrons that share an inner detector track with muons are discarded. This prevents muons, which mimic electrons via bremsstrahlung and subsequent photon conversion to be double-counted.
2. Non b -tagged jets within $\Delta R_y < 0.2$ of any of the remaining electrons are rejected.
3. Electrons with $\Delta R_y < 0.4$ separation to remaining jets are discarded.
4. Jets with an associated muon or with fewer than three tracks with $p_T > 500$ MeV within $\Delta R_y < 0.4$ of a muon are removed to get rid of jets resulting from the additional identification of muons as jets due to bremsstrahlung.
5. Muons with $\Delta R_y < 0.4$ separation to remaining jets are removed to improve the suppression of non-prompt muons produced in c - and b -hadron decays together with jets.

4.4 Trigger strategy

As the goal of the electroweak compressed analysis is to search for SUSY in scenarios with compressed mass spectra, implying events with low p_T leptons, single and dilepton triggers with high lepton p_T thresholds are not viable. The analysis therefore uses data recorded with E_T^{miss} -triggers [100], exploiting the raised E_T^{miss} values due to ISR jet activity.

In the L1 trigger the signals from calorimeter cells are successively summed and compared to noise thresholds to calculate a preliminary value for E_T^{miss} , based on which the events are preselected before being transferred to the HLT where the E_T^{miss} is recalculated using a set of different algorithms depending on the data-taking period. The `mht` algorithm uses hadronic jets reconstructed and calibrated similarly to the procedure in an offline physics analysis and was used in data-taking from 2015 to 2016. During the 2017-2018 data-taking period events were selected based on the E_T^{miss} determined by a combination of the `pufit` and `cell` algorithms. The former uses η - ϕ patches formed by clusters of calorimeter cells and corrected for pile-up contributions, while the latter simply sums over the full set of calorimeter cells with signals above a certain noise threshold. This trigger combination was able to keep the trigger rates almost at a stable level despite the rising instantaneous luminosities in the course of Run 2, while providing high efficiencies.

The performance of E_T^{miss} -triggers is not given by a sharp step function, but features a so-called turn-on region below about 200 GeV, where the trigger is not fully efficient. In an analysis the same trigger selection as in data has to be applied to events from MC simulation, especially if events in the E_T^{miss} range corresponding to the turn-on region are selected as in the analysis presented here. The trigger efficiencies are determined by simulation and corrected with dedicated scale factors in order to account for residual differences between data and simulation.

4.5 Analysis variables

Supersymmetric signal events result in a behaviour of certain variables which differs from what is obtained for SM background events. Requirements on these discriminating variables can thus be used to define signal regions (SR) enriched in signal events and validation (VR)

and control regions (CR), which are used to determine a data-driven background estimate in the SRs. In the following the variables used in the electroweak compressed analysis and the specific requirements set to define the signal regions are discussed.

Lepton multiplicity, flavour and sign

The analysis uses a search channel with two signal leptons (2ℓ) and a channel with one lepton and an additional signal track ($1\ell 1T$) targeting scenarios with very compressed mass spectra. In events with two leptons, the leptons are referred to as leading (ℓ_1) or subleading (ℓ_2) according to their p_T values. If an event contains more than one signal track the one with the highest p_T is used. The signal regions in both channels require the leptons/tracks to have charges with opposite sign (OS) and to be of the same flavour (SF).

Dilepton invariant mass $m_{\ell\ell}$

The invariant mass of the dilepton pair (where one of the leptons is represented by a track object in the $1\ell 1T$ channel) is defined as

$$m_{\ell\ell} = \sqrt{m_{\ell_1}^2 + m_{\ell_2}^2 + 2(E_{\ell_1}E_{\ell_2} - \mathbf{p}_{\ell_1} \cdot \mathbf{p}_{\ell_2})} \quad (4.2)$$

and can be expressed via the p_T of the leptons and their separation in pseudorapidity $\Delta\eta_{\ell_1\ell_2}$ and azimuthal angle $\Delta\phi_{\ell_1\ell_2}$ as

$$m_{\ell\ell} = \sqrt{2p_T^{\ell_1}p_T^{\ell_2}(\cosh\Delta\eta_{\ell_1\ell_2} - \cos\Delta\phi_{\ell_1\ell_2})} \quad (4.3)$$

in the relativistic limit $E \gg m$. An upper limit $m_{\ell\ell} < 60$ GeV is used to reject background processes with decays of on-shell Z bosons and other SM processes. By putting a veto on the region $3 \text{ GeV} < m_{\ell\ell} < 3.2 \text{ GeV}$ contributions from J/ψ decays are removed.

The kinematic endpoint in the $m_{\ell\ell}$ distribution of a dilepton pair originating from a second-to-lightest neutralino via the decay $\tilde{\chi}_2^0 \rightarrow (Z^* \rightarrow \ell\ell)\tilde{\chi}_1^0$ is determined by the mass splitting $\Delta m = m(\tilde{\chi}_2^0) - m(\tilde{\chi}_1^0)$. Therefore the shape of the $m_{\ell\ell}$ distribution is different for different signal points. This motivates the introduction of signal regions divided into several mutually exclusive bins in $m_{\ell\ell}$. These orthogonal bins can be statistically combined and fitted to data simultaneously, which is referred to in the following as a shape-fit. Such a shape-fit in $m_{\ell\ell}$ exploits the differences in the shape of the distribution between signal and background and is able to account for the differences in shape for the different signal points considered.

Lepton/track transverse momenta

In the 2ℓ channel the leading lepton is required to have $p_T > 5$ GeV in order to suppress backgrounds from fake/non-prompt leptons. The subleading lepton has to fulfill a sliding cut dependent on $m_{\ell\ell}$ in order to not lose efficiency for leptons in signals with low mass splittings but still reject background events with fake/non-prompt leptons and higher $m_{\ell\ell}$. As the $1\ell 1T$ channel is supposed to explicitly target scenarios where the decay products have very low momenta due to the small mass splittings of the SUSY particles, the corresponding SR requires that the identified lepton has $p_T < 10$ GeV and that the track has $p_T < 5$ GeV.

Dilepton distance $\Delta R_{\ell\ell}$

Dileptons resulting from the decay of a $\tilde{\chi}_2^0$ via an off-shell Z boson often have only a small angular separation, which leads to inefficiencies in the reconstruction of the leptons. The

method used by the analysis to correct these inefficiencies requires to exclude events with two leptons where the dilepton distance defined by

$$\Delta R_{\ell\ell} = \sqrt{(\eta_{\ell_1} - \eta_{\ell_2})^2 + (\phi_{\ell_1} - \phi_{\ell_2})^2} \quad (4.4)$$

is below certain thresholds. The resulting requirements are $\Delta R_{ee} > 0.3$, $\Delta R_{e\mu} > 0.2$ and $\Delta R_{\mu\mu} > 0.05$. The implicit constraint of $\Delta R_{\ell\ell} > 0.05$ for all flavour pairings also suppresses backgrounds from collinear lepton pairs originating from photon conversions. In the $1\ell 1T$ channel events with $0.05 < \Delta R_{\ell\text{track}} < 1.5$ are selected.

Di-tau invariant mass $m_{\tau\tau}$

The $m_{\tau\tau}$ variable is introduced to suppress the background from Z bosons recoiling against hadronic activity and decaying to boosted taus, which subsequently decay leptonically. In this scenario the di-tau invariant mass squared depends on the transverse momenta of the resulting leptons and missing transverse momentum carried by neutrinos and can be approximated as

$$m_{\tau\tau}^2 \simeq 2p_{\ell_1}p_{\ell_2}(1 + \xi_1)(1 + \xi_2), \quad (4.5)$$

where the parameters ξ_1 and ξ_2 are determined by solving $\mathbf{p}_T^{\text{miss}} = \xi_1 \mathbf{p}_T^{\ell_1} + \xi_2 \mathbf{p}_T^{\ell_2}$. The variable used by the analysis is then defined as the signed square root

$$m_{\tau\tau} = \text{sign}(m_{\tau\tau}^2) \sqrt{|m_{\tau\tau}^2|}. \quad (4.6)$$

In the 2ℓ channel events with $m_{\tau\tau}$ in the region between 0 GeV and 160 GeV are vetoed.

Number of jets N_{jet} and leading jet momentum

To select events with hadronic activity from ISR, the number of jets is required to be $N_{\text{jet}} \geq 1$ with a momentum of the leading jet $p_T > 100$ GeV.

Number of b -tagged jets $N_{b\text{-jet}}$

SM processes involving t -quarks often produce final states with b -jets through the decay $t \rightarrow Wb$. An upper limit or veto on the number of b -tagged jets can therefore reduce the background from $t\bar{t}$ production.

As the signal model of the analysis does not feature enhanced appearance of b -quarks, a veto on b -tagged jets is placed in the 2ℓ channel.

Separation of jets and leptons from $\mathbf{p}_T^{\text{miss}}$

Any jet in an event has to pass the requirement $\min(\Delta\phi(\text{any jet}, \mathbf{p}_T^{\text{miss}})) > 0.4$ to ensure the separation of jets from to $\mathbf{p}_T^{\text{miss}}$ in order to suppress the impact of jet energy mismeasurement on E_T^{miss} .

The requirement $\Delta\phi(j_1, \mathbf{p}_T^{\text{miss}}) \geq 2.0$ for the leading jet to be clearly separated from $\mathbf{p}_T^{\text{miss}}$ is very efficient for the signal involving ISR and reduces background contributions.

The $1\ell 1T$ signal region requires $\Delta\phi(\text{lep}, \mathbf{p}_T^{\text{miss}}) < 1.0$ to reject backgrounds with non-prompt leptons or hadrons.

Missing transverse energy $E_{\text{T}}^{\text{miss}}$

In SM processes missing transverse energy $E_{\text{T}}^{\text{miss}}$ can only be caused by neutrinos or mismeasurements in the detector. The SUSY scenarios considered by searches at the LHC typically lead to a much higher value of $E_{\text{T}}^{\text{miss}}$, due to invisible sparticles with high mass escaping the detector unmeasured.

Due to the low p_{T} values of the decay products of electroweakinos in models with compressed mass spectra the analysis presented here relies on the sparticle system to be recoiling off initial state radiation in order for the LSP to contribute to significant $E_{\text{T}}^{\text{miss}}$. All events are required to have $E_{\text{T}}^{\text{miss}} > 120$ GeV. Two signal regions with the additional upper limit of $E_{\text{T}}^{\text{miss}} < 200$ GeV select events in the trigger turn-on region and increase the search sensitivity to larger mass splittings, while a third SR and the $1\ell 1T$ signal region require $E_{\text{T}}^{\text{miss}} > 200$ GeV, where the online triggers are fully efficient.

Transverse mass $m_{\text{T}}^{\ell_1}$

The transverse mass of the leading lepton and $E_{\text{T}}^{\text{miss}}$, defined as

$$m_{\text{T}}^{\ell_1} = \sqrt{2(E_{\text{T}}^{\ell_1} E_{\text{T}}^{\text{miss}} - \mathbf{p}_{\text{T}}^{\ell_1} \cdot \mathbf{p}_{\text{T}}^{\text{miss}})}, \quad (4.7)$$

can be used to reduce backgrounds from fake and non-prompt leptons as the leading lepton and $\mathbf{p}_{\text{T}}^{\text{miss}}$ are expected to be closer for the signal as for the background processes.

$E_{\text{T}}^{\text{miss}}/H_{\text{T}}^{\text{lep}}$ variable

The $E_{\text{T}}^{\text{miss}}/H_{\text{T}}^{\text{lep}}$ variable, where $H_{\text{T}}^{\text{lep}}$ is the scalar sum of the lepton momenta

$$H_{\text{T}}^{\text{lep}} = \sum_i p_{\text{T}}^{\ell_i} \quad (4.8)$$

is an effective discriminant of events with soft leptons against events with harder leptons. As the SUSY models targeted with this analysis produce leptons with low p_{T} and only small contributions to the missing transverse energy, the values of $E_{\text{T}}^{\text{miss}}/H_{\text{T}}^{\text{lep}}$ tend to be rather low for the signal events.

The two signal regions with low $E_{\text{T}}^{\text{miss}}$ are made orthogonal by requirements on $E_{\text{T}}^{\text{miss}}/H_{\text{T}}^{\text{lep}}$, increasing the sensitivity to small mass splitting in the SR called SR-E-med by the selection $E_{\text{T}}^{\text{miss}}/H_{\text{T}}^{\text{lep}} > 10$

Recursive Jigsaw variables

In scenarios where the electroweakino system is recoiling against jets from initial state radiation there will be correlations between the missing transverse energies of the produced lightest neutralinos and the momenta of the ISR jets. These can be used to define a new type of kinematic observables based on the recursive jigsaw reconstruction (RJR) technique [101], which can be more useful than typical discriminating variables in scenarios like the one considered here. The RJR procedure uses the axis of maximum back-to-back p_{T} , referred to as the thrust axis, to define the direction of the recoil of the produced sparticles against the ISR jets. The thrust axis is then used to define two different hemispheres perpendicular to it. The hemisphere labeled S contains the decay products of the initially produced electroweakinos responsible for the $E_{\text{T}}^{\text{miss}}$, while the ISR hemisphere contains the hadronic activity. Based on this description two variables used by the analysis are defined.

	2ℓ	$1\ell 1T$
number of leptons (tracks)	= 2 leptons	= 1 lepton and ≥ 1 track
lepton p_T [GeV]	$p_T^{\ell_1} > 5$	$p_T^\ell < 10$
$\Delta R_{\ell\ell}$	$\Delta R_{ee} > 0.3, \Delta R_{e\mu} > 0.2, \Delta R_{\mu\mu} > 0.05$	$0.05 < \Delta R_{\ell track} < 1.5$
lepton (track) charge and flavour	$e^\pm e^\mp$ or $\mu^\pm \mu^\mp$	$e^\pm e^\mp$ or $\mu^\pm \mu^\mp$
lepton (track) invariant mass [GeV]	$3 < m_{ee} < 60, 1 < m_{\mu\mu} < 60$	$0.5 < m_{\ell track} < 5$
J/ψ invariant mass [GeV]	veto $3 < m_{\ell\ell} < 3.2$	veto $3 < m_{\ell track} < 3.2$
$m_{\tau\tau}$ [GeV]	< 0 or > 160	-
E_T^{miss} [GeV]	> 120	> 120
N_{jets}	≥ 1	≥ 1
$N_{b\text{-jets}}$	= 0	-
leading jet p_T [GeV]	≥ 100	≥ 100
$\min(\Delta\phi(\text{any jet}, \mathbf{p}_T^{\text{miss}}))$	> 0.4	> 0.4
$\Delta\phi(j_1, \mathbf{p}_T^{\text{miss}})$	≥ 2.0	≥ 2.0

Table 4.1: Preselection requirements used for all search regions. Dashes indicate that no selection is made.

	SR-E-low	SR-E-med	SR-E-high	SR-E-1 $\ell 1T$
E_T^{miss} [GeV]	[120, 200]	[120, 200]	> 200	> 200
$E_T^{\text{miss}}/H_T^{\text{lep}}$	< 10	> 10	-	> 30
$\Delta\phi(\text{lep}, \mathbf{p}_T^{\text{miss}})$	-	-	-	< 1.0
lepton (track) p_T [GeV]	$p_T^{\ell_2} > 5 + m_{\ell\ell}/4$	-	$p_T^{\ell_2} > 5 + \min(10, 2 + m_{\ell\ell}/3)$	$p_T^{\text{track}} < 5$
M_T^S [GeV]	-	< 50	-	-
$m_T^{\ell_1}$ [GeV]	[10, 60]	-	< 60	-
R_{ISR}	[0.8, 1.0]	-	$[\max(0.85, 0.98 - 0.02 \times m_{\ell\ell}, 1.0)]$	-

Table 4.2: Event selection for the signal regions used to search for electroweakinos. The preselection requirements specified in Tab. 4.1 are implied. Dashes indicate that no selection is made.

The variable R_{ISR} is given by the ratio of the E_T^{miss} to the transverse momentum in the ISR hemisphere and is sensitive to the mass ratio of the lightest electroweakinos. The signals have values of R_{ISR} close to 1 especially for low mass splittings, which is used for the signal region requirements. The transverse mass of the S system M_T^S takes low values for signal events.

4.6 Signal regions

The final definitions of the three signal regions targeting electroweakinos in the 2ℓ and the SR in the $1\ell 1T$ channel used by the electroweak compressed analysis are specified in Tab. 4.1 and 4.2. The region SR-E-high selects events with high missing transverse energy, where the E_T^{miss} trigger is fully efficient. SR-E-1 $\ell 1T$ also selects events in the plateau region of the trigger and enhances the sensitivity of the search for scenarios with very compressed electroweakino mass spectra. The regions SR-E-low and SR-E-med are both designed for events with E_T^{miss} in the trigger turn-on region with SR-E-low targetting larger mass splittings and SR-E-med providing sensitivity for smaller mass splittings.

The signal regions of the 2ℓ channel are binned in nine $m_{\ell\ell}$ bins with boundaries at $m_{\ell\ell} = 1, 2, 3, 5, 10, 20, 30, 40$ and 60 GeV. Dielectron and dimuon events are binned separately. As the invariant mass for a dilepton pair is required to be greater than 3 GeV the first bins will remain empty in this case. Events in the $m_{\ell\ell} > 30$ GeV bins of the SR-E-med region are ignored as they have minimal sensitivity to the targeted signal models. The signal region

SR-E- $1\ell 1T$ is divided into six bins with boundaries at $m_{\ell\text{track}} = 0.5, 1, 1.5, 2, 3, 4$ and 5 GeV. Due to the low number of events the two lepton flavours are not treated separately in this channel.

The analysis performs two different types of statistical fits. By merging the two different flavour scenarios and by merging the signal region bins introduced above up to all possible bin boundaries a set of inclusive single-bin signal regions is constructed. Every one of these inclusive SRs is fitted individually to test for model-independent excesses of events above the SM prediction.

The second statistical test is an exclusion fit, which is performed in the case that no significant excess above the SM expectation is seen and uses the full binning introduced above in order to perform a shape-fit in $m_{\ell\ell}$. As such a shape-fit exploits the distribution of $m_{\ell\ell}$ in the signal models it yields limits, which depend on the corresponding model. In the exclusion fit all four orthogonal signal regions for electroweakinos are statistically combined.

4.7 Background estimation

In order to draw any conclusions about the SUSY signal under consideration an accurate estimate of the SM background is needed. Two sources of background exist. Reducible backgrounds are caused by missed or false reconstruction of physics objects or mismeasurements. Irreducible backgrounds stem from processes with final states identical or almost identical to the one from the studied signal.

4.7.1 Reducible background

The main sources of reducible background in the 2ℓ channel are events with leptons originating from photon conversions or heavy-flavour hadron decays, or due to the misidentification of jets. These are estimated using a data-driven method, referred to as the Fake Factor method [102, 103].

In the $1\ell 1T$ channel the dominant background is given by events where a lepton is associated with a random track. This background is estimated using a dedicated data-driven method.

4.7.2 Irreducible background

While processes with only little contributions to the total irreducible background in the 2ℓ channel are estimated using MC simulation only, the dominant backgrounds are estimated by a semi-data-driven approach. This procedure involves the definition of control regions (CR), which are each designed to be enriched in a certain type of background and ideally free of signal. A fit of MC samples to the observed data is performed and the normalization obtained for the background estimate in the CR is extrapolated to the SRs. In order to assess the validity of the extrapolation from the CRs to the SRs, validation regions (VR) are defined. The VRs are placed in between the signal and control regions in terms of the observables extrapolated over and designed to be similar to the SRs while minimising signal contamination. The VRs do not participate in the actual fits of the physics analysis. In order to simultaneously fit both the SRs and CRs these regions have to be orthogonal. Fig. 4.5 gives a schematic overview of this analysis strategy.

The dominant irreducible backgrounds $t\bar{t}/tW$, WW/WZ and $Z^{(*)}/\gamma^*(\rightarrow \tau\tau) + \text{jets}$ are estimated using the method just described. An overview of the control regions and the validation regions employed in the search for electroweakinos is given in Tab. 4.3. Three control regions

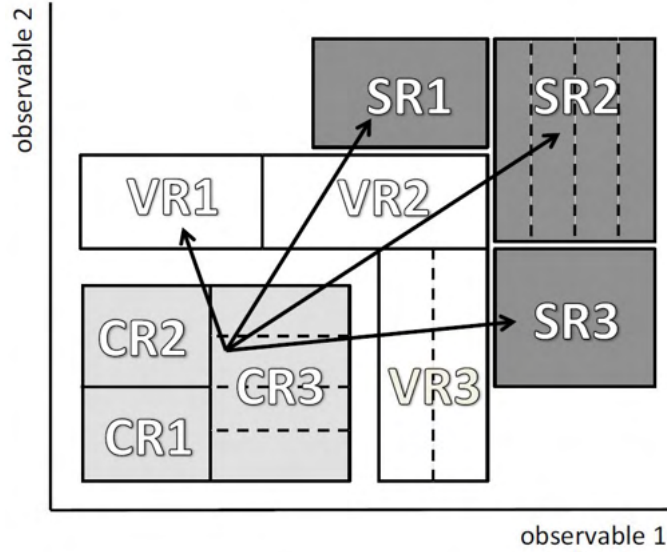


Figure 4.5: Schematic view of an analysis strategy involving control, validation and signal regions. The extrapolation procedure is indicated by the arrows. All regions can in principle have more than one bin. Figure taken from Ref. [104].

labeled CR-E-high and CR-E-low are used to constrain the backgrounds in SR-E-high and SR-E-low respectively. For SR-E-med no dedicated CRs are constructed and the CRtau-E-low region is instead used to normalize the dominant $Z^{(*)}/\gamma^{*}(\rightarrow \tau\tau) + \text{jets}$ background in this signal region. For each SR an individual validation region, which keeps the selection criteria of the SR in question but requires events to contain two different-flavour leptons, is designed.

A so-called background-only fit simultaneously taking into account all the control regions is performed using the `HistFitter` package [104] and the corresponding dominant background processes are normalized. The results of this fit are used to obtain a background prediction in the validation regions, which is then used to validate the background model by comparing to data. As only the observed event counts in the CRs are taken into account in this procedure the obtained background estimate allows for an unbiased comparison with the observed numbers of events in the VRs. This comparison is shown in Fig. 4.6 for the validation regions VRDF-E-high, VRDF-E-low and VRDF-E-med binned in $m_{\ell\ell}$ in the same way as the corresponding signal regions. A slight disagreement between data and background estimation is observed in several VR bins. In particular for the region VRDF-E-low a trend towards an overfluctuation of the observed data with respect to the SM expectation can be seen. As no general over- or underestimation is observed and all significances are below 2σ the overall agreement is deemed to be acceptable.

In order to further assess the behaviour of the background estimate also in the signal regions, a so-called CR+SR background-only fit [104] is performed. This fit configuration takes into account all control regions and the exclusive signal regions, while turning off the signal component. A comparison of the observed event yields with the background expectation obtained from this fit, as shown in Fig. 4.7, again reveals over- and underfluctuations in several bins of the different signal regions. Overall the deviations are evaluated to be acceptable.

region	SR orthogonality	lepton flavour	additional requirements
CRtop-E-high CRtop-E-low	$N_{b\text{-jet}} \geq 1$	$ee + \mu\mu + e\mu + \mu e$	$R_{\text{ISR}} \in [0.7, 1.0]$, $m_{\text{T}}^{\ell_1}$ removed $E_{\text{T}}^{\text{miss}}/H_{\text{T}}^{\text{lep}}$ and $m_{\text{T}}^{\ell_1}$ removed
CRtau-E-high CRtau-E-low VRtau-E-med	$m_{\tau\tau} \in [60, 120]$ GeV	$ee + \mu\mu + e\mu + \mu e$	$R_{\text{ISR}} \in [0.7, 1.0]$, $m_{\text{T}}^{\ell_1}$ removed $R_{\text{ISR}} \in [0.6, 1.0]$, $m_{\text{T}}^{\ell_1}$ removed -
CRVV-E-high CRVV-E-low	$R_{\text{ISR}} \in [0.7, 0.85]$ $R_{\text{ISR}} \in [0.6, 0.8]$	$ee + \mu\mu + e\mu + \mu e$	$m_{\text{T}}^{\ell_1}$ removed $m_{\text{T}}^{\ell_1} > 30$ GeV, $N_{\text{jets}} \in [1, 2]$, $E_{\text{T}}^{\text{miss}}/H_{\text{T}}^{\text{lep}}$ removed
VRDF-E-high VRDF-E-low VRDF-E-med	$e\mu + \mu e$	$e\mu + \mu e$	- - -

Table 4.3: Control and validation regions used for the estimation of irreducible backgrounds, presented relative to the selections of the corresponding signal regions according to Tab. 4.1 and 4.2. Dashes indicate that no selection is made.

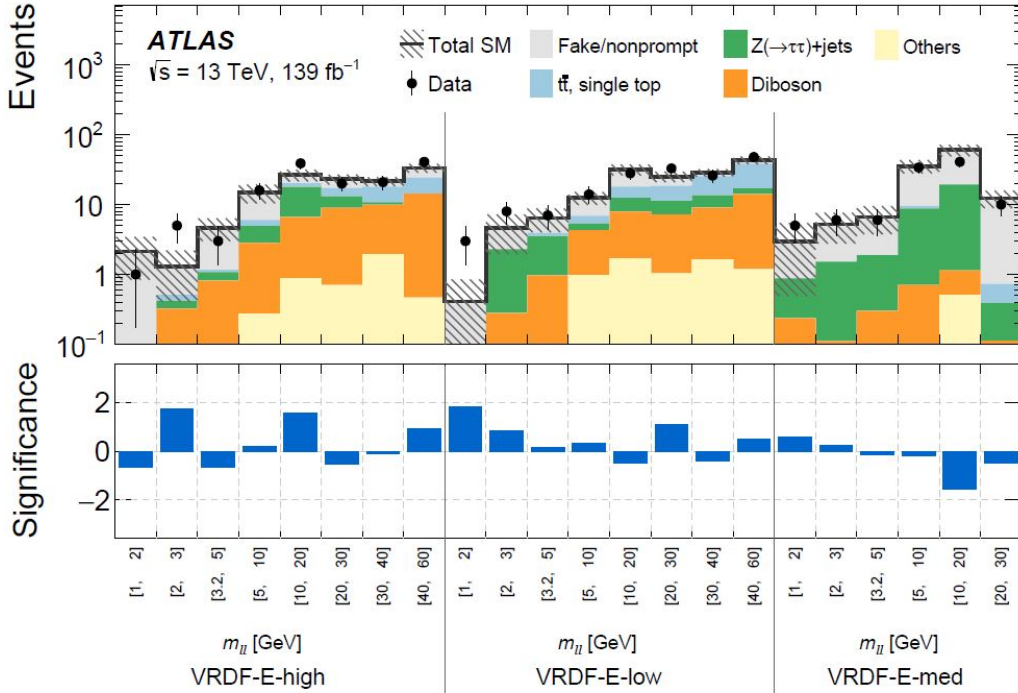


Figure 4.6: Comparison of the observed and expected event yields in the VRs after a background-only fit of the CRs. The VRs are divided into $m_{e\ell\ell}$ bins identically to the corresponding SRs. The shaded uncertainty band includes both MC statistical and systematic uncertainties. The bottom panel shows the significance of the differences between the observed data and the expected event counts computed according to Ref. [105]. Figure adapted from Ref. [1].

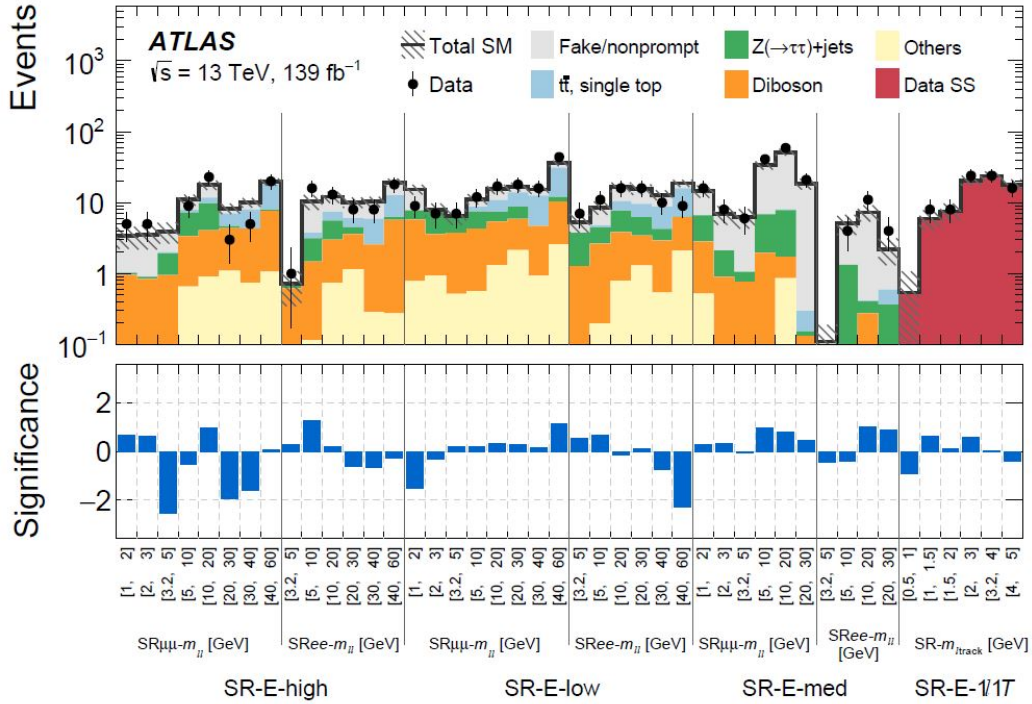


Figure 4.7: Comparison of the observed and expected event yields in the $m_{\ell\ell}$ bins of the SRs after a CR+SR background-only fit. The uncertainties of the background estimate include both MC statistical and systematic uncertainties. The bottom panel shows the significance of the differences between the observed data and the expected event counts computed according to Ref. [105]. Figure adapted from Ref. [1].

4.8 Results of the model dependent signal fit

This section only presents the results obtained by a model-dependent signal fit [104], also called exclusion fit. For the results of the fit based on the inclusive signal regions see Ref. [1].

The exclusion fit is performed separately for all signal points in the signal grid and uses all control regions and the binned signal regions (including SR-E-1 ℓ 1T). In addition to the background, signal contributions are allowed in all regions. The signal strength parameter μ_{sig} is introduced as a factor scaling the signal sample across all regions. Ultimately for each signal point expected and observed CL_s values can be calculated. A model is considered excluded if $\text{CL}_s < 0.05$. The exclusion at 95% confidence level for the different studied scenarios is presented in two-dimensional plots with $m(\tilde{\chi}_2^0)$ on the horizontal and the mass difference $\Delta m(\tilde{\chi}_2^0, \tilde{\chi}_1^0)$ on the vertical axis. The top plot in Fig. 4.8 shows the obtained exclusion limits for the Higgsino signal samples, with all points inside the contour excluded at 95% CL. The two plots on the bottom correspond to the two different scenarios where the LSP is Bino-like.

The exclusion power achieved by the analysis is mostly due to the high E_T^{miss} channel. The low E_T^{miss} channel adds sensitivity to models with higher mass splittings, while the 1 ℓ 1T channel improves the results for very small mass splittings.

The behaviour of the observed exclusion contour in the bottom right plot in Fig. 4.8 at high mass differences is caused by a combination of an overfluctuation of data for events with $10 \text{ GeV} < m_{\mu\mu} < 20 \text{ GeV}$ and an underfluctuation for events with $20 \text{ GeV} < m_{\mu\mu} < 40 \text{ GeV}$ in SR-E-high. This behaviour is already visible in the results of the CR+SR background-only fit in Fig. 4.7 and is enhanced by the presence of the signal model in the signal fit.

In the case of Higgsino production, $\tilde{\chi}_2^0$ masses up to 193 GeV can be excluded at a mass splitting of 9.3 GeV. At the lower bound set on the $\tilde{\chi}_2^0$ mass by LEP, mass splittings from 2.4 GeV to 55 GeV are excluded. For the scenario with Bino-like LSP and $m(\tilde{\chi}_2^0) \times m(\tilde{\chi}_1^0)$, electroweakino masses of up to 240 GeV for mass splittings of 7 GeV are excluded. The mass splittings of the excluded models in this case lie in a range from 1.5 GeV to 46 GeV.

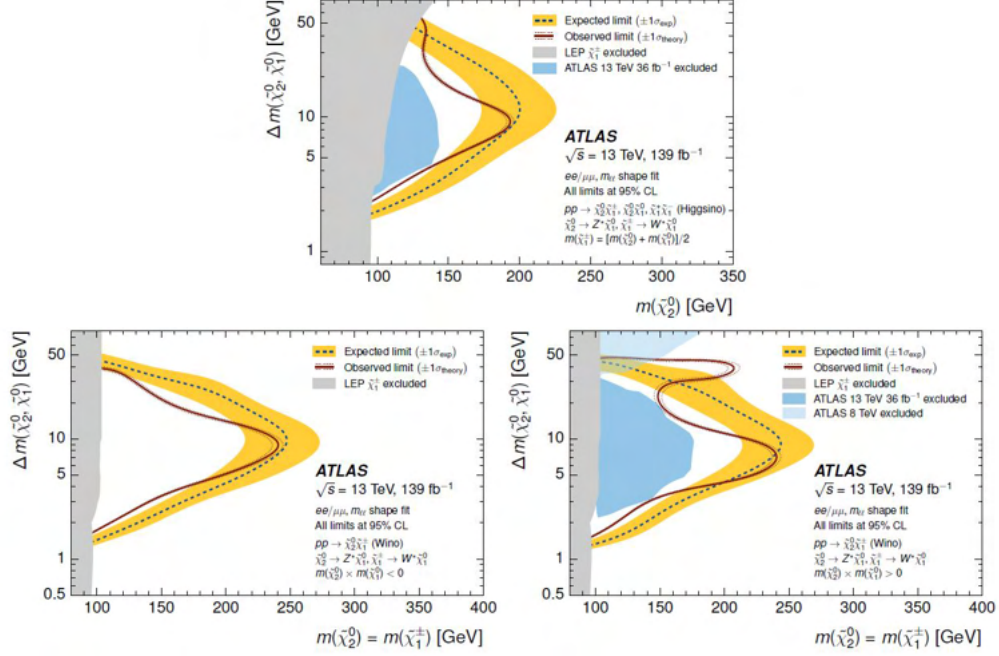


Figure 4.8: Expected (blue dashed line) and observed (red solid line) 95 % CL exclusion contours (with uncertainties) for different electroweakino scenarios determined by the electroweak compressed analysis [1]. The top plot shows the results for the Higgsino scenario, the bottom plots correspond to the two different scenarios with a Bino LSP, which differ by the relative sign of the lightest neutralino masses (see. 4.1). The gray regions indicate the LEP lower limits on the chargino mass. The blue regions correspond to the exclusion limits set by previously performed ATLAS analyses [67, 106, 107].

Chapter 5

Reinterpretations in the pMSSM

Traditionally, the ATLAS Collaboration uses a large set of simplified models to interpret the results of SUSY searches at the LHC. In addition to the issue regarding the validity of results based on these models mentioned in Sec. 2.2.7, another potential issue of searching for SUSY by performing individual analyses optimized for individual decay chains is that important effects present in more complete models might be neglected and that certain regions of SUSY models might remain uncovered. In particular, simplified models struggle to cover topologies where the initially produced sparticles decay to the final state via a long decay chain with various intermediate sparticles in a generic way. For this reason, performing reinterpretations of these searches in more complex models with a higher dimensional parameter space is a highly desirable task. Not only will this reveal the constraints put on more realistic SUSY scenarios by individual searches, but this will also lead to a better understanding of the true coverage of the ATLAS SUSY search program, by offering the possibility to determine a combined sensitivity of the different searches and by potentially revealing model regions not covered by current searches.

One model space particularly suited for such reinterpretations is the pMSSM, introduced in Sec. 2.2.6. The pMSSM with its 19 parameters represents a compromise between providing more complex SUSY scenarios and still being of low enough dimensionality to enable large-scale studies with reasonable computational effort. Nevertheless, approximations in the evaluation of the pMSSM models are needed in order to make the evaluation of a high number of models with the complete set of considered SUSY searches feasible. The results of corresponding studies, performed by the ATLAS Collaboration based on data taken during Run 1 of the LHC, can be found in Refs. [108, 109]. Efforts for the second iteration of pMSSM reinterpretations of ATLAS searches, including e.g. the electroweak compressed analysis, using the full Run-2 dataset are currently ongoing and some aspects of this are discussed in the following sections.

Another important aspect of performing interpretations of the ATLAS SUSY search program in the pMSSM, is that results from other measurements, e.g. direct or indirect dark matter searches, electroweak precision measurements and flavour-physics experiments can be taken into account. The results of these experiments place constraints on the pMSSM model space, which can be accounted for in different ways. In Ref. [108] the pMSSM models were sampled from the parameter space using flat probability distributions and only later the models were filtered according to the requirements put on certain observables by the experiments. Analogously, in Sec. 5.4 an upper limit on the dark matter relic abundance as observed by the Planck experiment [23] filters out models not compatible with the corresponding constraint. A different approach was used in Ref. [109]. In these studies, focusing on the part of the pMSSM relevant for electroweakinos, a dedicated Bayesian likelihood was used to in-

clude external constraints during the sampling of the models. The goal of this is to generate and subsequently process only models, which are interesting in terms of the considered non-collider experiments. In particular this can be (and has been) used to include results from (in)direct DM detection experiments, in order to study the impact of ATLAS searches for electroweakinos on the parameter space of DM candidates. This method of performing an initial likelihood scan is discussed more in Chap. 7.

This chapter starts with an introduction of two approaches to analysis simplifications: a truth-level implementation of the signal-related analysis steps (see Sec. 5.1) and the statistical evaluation based on simplified likelihoods (see Sec. 5.3). These simplifications are necessary in large-scale reinterpretations, in order to process the high number of models under consideration. Validation studies of the truth-level implementation of the electroweak compressed analysis, comparing event counts, are presented in Sec. 5.2. A description of the generation of pMSSM models focusing on the electroweak sector used to perform preliminary studies on reinterpretations of ATLAS searches for electroweakinos, including the compressed search, is given in Sec. 5.4. The results of the evaluation of these models are presented in Sec. 5.5.

5.1 Truth-level analyses

The aim of ongoing efforts within the ATLAS Collaboration is to perform a search for SUSY in the parameter space of the pMSSM. These large-scale studies, referred to as a pMSSM scan, are going to evaluate a high number of pMSSM models using a set of SUSY searches originally only interpreted in simplified models. In order to make such a collective reinterpretation of analyses computationally feasible, while still maintaining the original sensitivity of the analysis, sophisticated simplifications have to be employed in the analysis chains. One of these simplifications involves running a truth-level implementation of all the analyses included in the scan in the first step. This means that in each analysis the generator-level objects are used, instead of performing a dedicated full detector simulation, a process that is highly expensive in terms of computing resources. Only a so-called smearing procedure is employed as an approximation of the detector response.

The truth-level implementations of the ATLAS SUSY analyses employed in the pMSSM scan are collected in the SIMPLEANALYSIS framework¹ [110]. An analysis in this framework contains the object definitions, overlap removal, computation of relevant observables and the definitions of the control and signal regions of the original search, as e.g. presented in Chap. 4 for the electroweak compressed search. A truth smearing procedure is applied. The smearing approximates the effects of a detector simulation on MC samples through parametrized reconstruction and identification efficiencies and maps mimicking the effects of finite detector resolution. The different physics objects are smeared independently and the exact smearing procedure depends on the object definitions of the analysis. The parametrizations of the efficiency maps are obtained from results of studies of the performance of the ATLAS detector.

For electrons [86] the identification efficiencies are parametrized by $|\eta|$ and p_T . In p_T , six bins in the range from 7 GeV to 120 GeV are used in the parametrization and the efficiencies are obtained by a linear interpolation between the centers of two adjacent bins. If an electron has a p_T value outside of this range, the value at the respective bin boundary is used. The efficiency maps are different for the different identification working points. Rates of recon-

¹It is worth noting that the SIMPLEANALYSIS framework and with it the full technical implementation of the included searches are made publicly available, which enables reinterpretations by efforts outside of the ATLAS Collaboration.

structuring a fake electron in a true jet are also taken into account with similarly constructed maps. The effect of the finite resolution of energy measurements in the detector on the transverse energy of electrons is approximated by drawing from a Gaussian centered around the truth value and width corresponding to the measured energy resolution also parametrized in $|\eta|$ and p_T .

For muons [89] the efficiencies are handled analogously to the case of electrons. Several maps parametrized in $|\eta|$ and p_T exist for the different identification working points and the p_T is smeared using a Gaussian distribution corresponding to finite momentum resolution.

The transverse momentum of jets is smeared to account for effects from finite detector resolution. Flavour tagging efficiencies are obtained from measurements and the resulting efficiency maps for the different working points of the flavour tagging algorithm, parametrized in $|\eta|$ and p_T , are used in the smearing procedure.

The smeared missing transverse energy is calculated based on the smeared truth objects and an approximation of the track soft term obtained from measurements.

5.2 Validation of the truth-level electroweak compressed analysis

In this section studies comparing event counts in the 2ℓ signal regions of the electroweak compressed analysis defined in Sec. 4.6 and distributions of kinematic observables of exemplary signal points as obtained from the analysis at smeared truth- and reconstruction-level², are presented. In order for the smeared truth-level analysis to be a valid approximation these should largely agree.

5.2.1 E_T^{miss} trigger efficiencies

The signal regions SR-E-low and SR-E-med both select events with $120 < E_T^{\text{miss}} < 200$ GeV in the turn-on region of the E_T^{miss} trigger. As already mentioned in Sec. 4.4 the trigger efficiencies during data-taking also have to be applied to simulated MC samples. The left plot in Fig. 5.1 compares the distributions of missing transverse energy for a signal model considered in the analysis, where the corresponding trigger efficiencies are taken into account only for the reconstruction-level sample. A clear mismatch between the two distributions is seen for values of E_T^{miss} in the turn-on region with higher number of events for the truth-level distribution. After the effect of the E_T^{miss} trigger is removed for the reconstruction-level sample in the plot shown in Fig. 5.1(b) a much better agreement is observed.

A rigorous implementation of the E_T^{miss} trigger efficiencies in the truth-level analysis is difficult, in part because several different trigger algorithms resulting in different turn-on curves were used in the Run-2 data-taking period. In an analysis on reconstruction-level the appropriate trigger efficiencies are applied using the run number assigned to MC events, which is not possible on truth-level. As a naive implementation of the effects of the missing transverse energy trigger on the truth-level events, in the simplified analysis one representative trigger curve is chosen from which the needed efficiencies are determined according to the calculated E_T^{miss} value. A comparison of the distribution obtained after the E_T^{miss} trigger is included in the truth-level analysis is shown in Fig. 5.1(c). It can be seen that for values of E_T^{miss} between 120 GeV and 140 GeV the number of truth-level events is reduced too much, while in the rest of the trigger turn-on region the agreement improves. This is most likely caused by the chosen

²The term reconstruction-level in this context refers to MC samples for which a dedicated detector simulation is performed and the physics objects are reconstructed as in the original analysis.

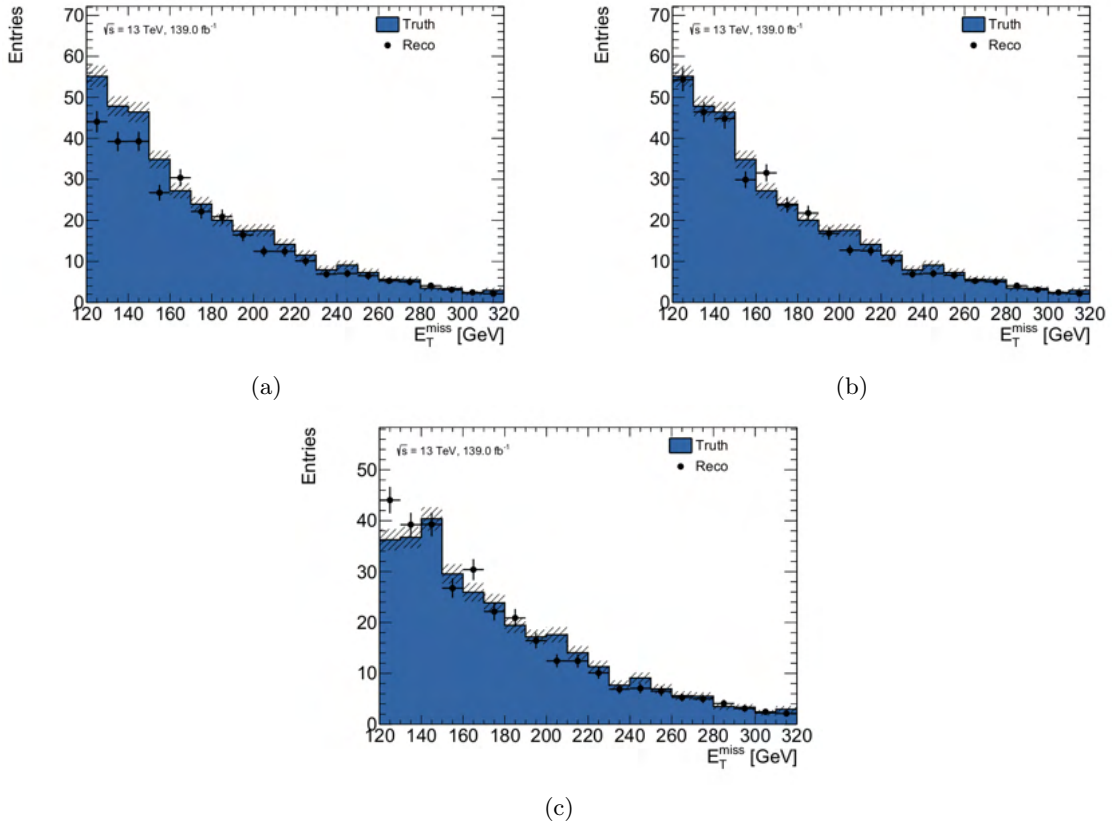


Figure 5.1: The distribution of E_T^{miss} for a signal point with $(m(\tilde{\chi}_2^0), m(\tilde{\chi}_1^0)) = (100, 40)$ GeV is shown. The analysis preselection (see Tab. 4.1) and an additional requirement on the p_T of both leptons to be above 20 GeV are applied. Smearing is applied to the truth-level samples. In (a) an event selection according to the missing energy trigger is applied to the reconstruction-level sample, while in (b) the trigger efficiencies are ignored. The distribution in (c) is obtained, when the E_T^{miss} trigger is also implemented in the truth-level analysis. The uncertainties are MC statistical only.

turn-on curve not being appropriate for the reconstruction-sample considered here. A general improvement could probably be achieved by implementing E_T^{miss} trigger efficiencies obtained by averaging the efficiencies of curves of several different trigger algorithms.

The implementation of E_T^{miss} trigger efficiencies is already applied to the samples used for the plots in the following.

5.2.2 Comparison of kinematic distributions at preselection level

Fig. 5.2 shows distributions of kinematic observables used in the analysis for two different exemplary signal points at smeared truth- and reconstruction-level with low and high mass splittings. The preselection requirements specified in Tab. 4.1 are applied. All plots for both signal points show an overall excess in the event counts of the smeared truth samples in comparison to the reconstruction-level. Distributions of additional analysis variables for the two signal points considered here, showing a similar behaviour, can be found in Figs. A.1-A.4. Plots for an additional signal point with masses $(m(\tilde{\chi}_2^0), m(\tilde{\chi}_1^0)) = (175, 150)$ GeV, also showing the same behaviour are shown in Figs. A.5 and A.6.

In Fig. 5.2(c) a mismatch in shape between the distributions is also visible with a discrepancy of the yields in the bins at low values of the p_T of the leading lepton. This leads e.g. to a higher overall mismatch for the very compressed signal point with $(m(\tilde{\chi}_2^0), m(\tilde{\chi}_1^0)) = (100, 95)$ GeV for which the sample contains almost exclusively events where the leading lepton has $p_T < 20$ GeV.

A comparison of the numbers of b -tagged jets in smeared truth and full reconstruction samples of the signal point with $(m(\tilde{\chi}_2^0), m(\tilde{\chi}_1^0)) = (100, 40)$ GeV are shown in Fig. 5.3. For this plot the preselection is applied with the requirement on the number of b -jets removed. While at smeared truth-level there is again an overestimation of the event counts with zero b -tagged jets, the number of events with one or more b -jets shows the opposite behaviour.

Overall the plots show that, although smearing is activated when the truth-level analysis is run, the truth-level analysis systematically overestimates the event counts and leads to different shapes of the distributions of the transverse momentum of leptons and number of b -tagged jets. This is in contrast to results of other studies, where the implementation of a different analyses together with the smearing procedure in SIMPLEANALYSIS lead to a good agreement with the reconstruction-level results (see Ref. [111]). The reason for this is that the scenario of direct production of electroweakinos with compressed mass spectra considered in the electroweak compressed analysis produces leptons with very low p_T . The smearing procedure as introduced in Sec. 5.1 is not optimized for the electron and muon object definitions given in Sec. 4.2, specifically chosen to handle the targeted low-momentum regime. Additionally, Fig. 5.3 implies that the b -tagging efficiencies employed in the smearing procedure might not be an accurate approximation of the corresponding detector effects. As the analysis selects only events with zero b -jets this will lead to an overall mismatch between the truth- and reconstruction-level event counts in the preselection used for the plots shown above, as well as in the signal regions.

5.2.3 Comparison of yields in the signal regions

The overestimation of yields on truth-level is also clearly visible after the different signal region event selections are applied, as can be seen in the left column in Fig 5.4. These plots show pairs of the total truth and reconstruction event counts obtained per each signal point in a 2-dimensional scatterplot. The bins in $m_{\ell\ell}$ and the different flavours have been combined for all the signal regions SR-E-high, SR-E-low and SR-E-med. The plots in the left column are

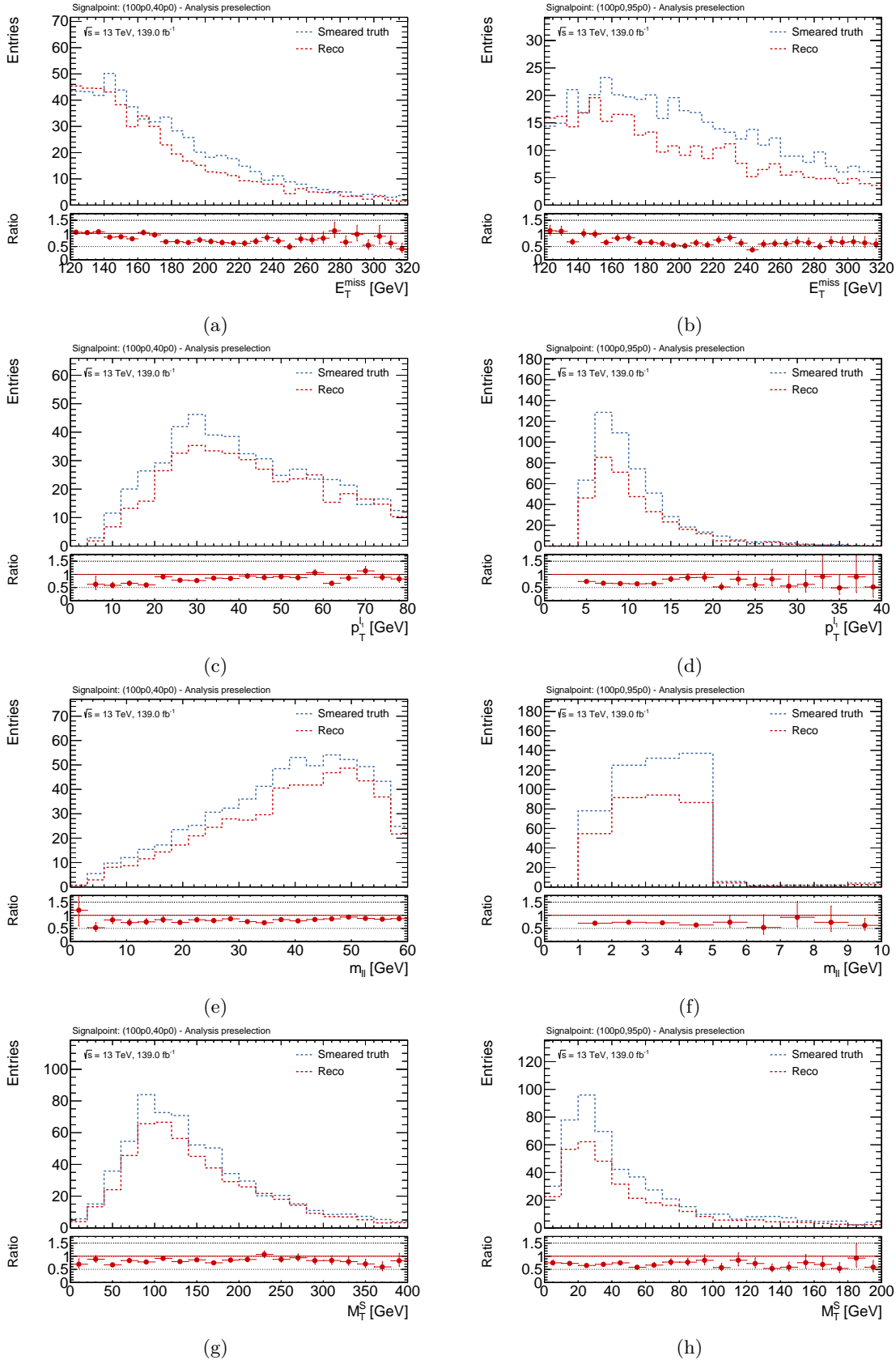


Figure 5.2: Comparison of the distributions of kinematic observables used in the analysis for two different signal points at smeared truth- and full-reconstruction-level with low and high mass splittings: $(m(\tilde{\chi}_2^0), m(\tilde{\chi}_1^0)) = (100, 40)$ and $(100, 95)$ GeV. All distributions are shown in the preselection defined in Tab. 4.1. The ratio pads give the ratios of the reco- to the smeared truth-level distributions with error bars corresponding to MC statistical uncertainties.

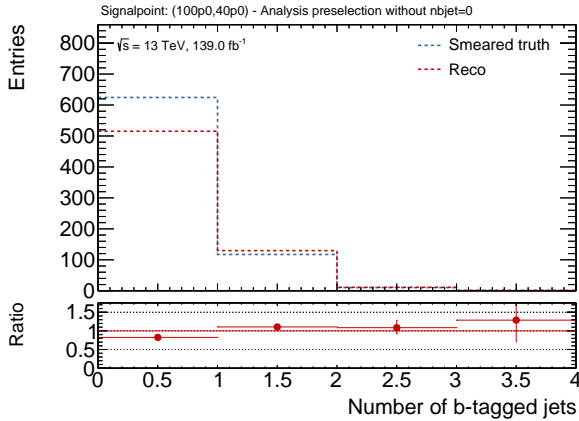


Figure 5.3: Distribution of the number of b -tagged jets at smeared truth- and reconstruction-level. Preselection requirements without the veto on b -jets are applied. The plot shows different behaviour for the number of events with zero or one or more b -jets. Only MC statistical uncertainties are considered.

obtained running the same truth-level analysis including the smearing procedure as before. The points corresponding to individual signal points mostly lie under the diagonal indicating an excess of truth-level event rates. The observed mismatch motivates the computation of additional efficiencies and their implementation in the truth-level version of the analysis.

5.2.4 Computation of additional efficiencies

In order to correct for the observed mismatch, additional efficiencies are computed and implemented. These efficiencies are calculated based on smeared truth-level yields obtained for samples of a set of electroweakino signal points using the truth-level implementation of the electroweak compressed analysis. For every signal point the event rates in the individual bins (also split up into ee and $\mu\mu$) of the signal regions SR-E-high, SR-E-low and SR-E-med are determined. Then for every signal point the ratios of the reconstruction-level yields of the considered signal point to the truth-level yields are calculated for all SR bins. These ratios are averaged over all signal points to obtain an efficiency for every individual SR bin. The calculated efficiencies are implemented in the truth-level analysis by weighting the event counts obtained for the different signal regions with the corresponding efficiency. An obvious downside of this approach to correct the truth-level event count is that it is specific to the electroweak compressed analysis.

Results obtained with these efficiencies implemented are shown in the right column of Fig. 5.4. For these plots the smeared truth-level yields in the individual signal region bins are determined, weighted by the corresponding efficiencies and then summed to obtain an event rate for every signal point. Especially for the signal region SR-E-high an improvement of the match of the yields obtained for truth- and reconstruction-level is achieved.

5.3 Simplified likelihood fit

In order to be able to perform large-scale reinterpretations not only the signal chain of the employed analyses but also the statistical evaluation has to be computationally feasible. Typical searches for SUSY within ATLAS use complex statistical models with a high number of search regions, additionally split in multiple bins and nuisance parameters. As one also wants to perform not just one analysis and in the end evaluate a number of models on the order of $\mathcal{O}(10^6)$ running the statistical inference at full complexity for all models would quickly become to computationally expensive.

In the pMSSM scans that were performed by ATLAS after Run 1 [108, 109] two different

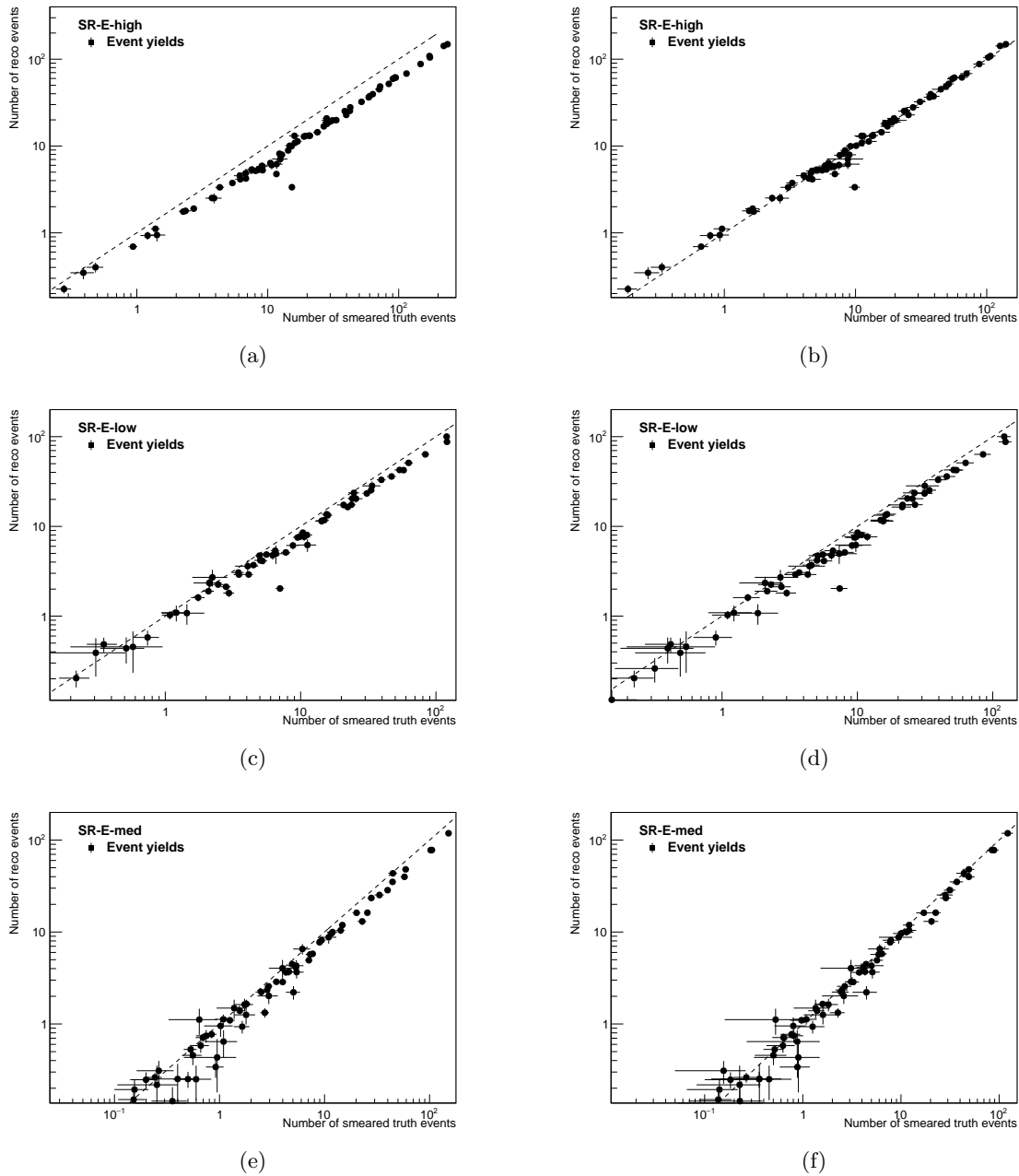


Figure 5.4: Comparison of reco- and truth-level yields in the SRs of the 2ℓ channel. The SR bins are merged. The dashed line is the diagonal where the yields are equal. In the left columns the points representing individual signal points mostly lie under the diagonal. The plots on the right show the yields obtained with the additional efficiencies derived in Sec. 5.2.4 applied.

methods were used to reduce the computational cost of the statistical evaluation. Both relied on simplifying the original analyses featured in the respective scan by only using single-bin signal regions or by using every bin of a originally binned signal region separately. The calculation whether a model is excluded or not excluded did therefore not make use of the statistical combination of SRs or a shape-fit for any analysis in either of the two efforts. This leads to an overall worse exclusion power. It is therefore highly desirable to improve the method that is used to reduce the complexity of the statistical evaluation of ATLAS SUSY searches in the pMSSM scan after Run 2.

The method introduced in Refs. [111, 112] uses the results of a background-only fit to data using the full likelihood of an analysis as the background model in a simplified likelihood. The simplified background model consists of a single sample with pre-fit rates obtained from the background-only fit. All nuisance parameters of the original likelihood are reduced to one parameter corresponding to the uncertainty of the total SM background estimate obtained from the fit using the full analysis likelihood. The search regions and the binning of the original likelihood are still present in the simplified likelihood. In addition a signal sample is needed, which then adds the signal strength as a second parameter to the likelihood.

The goal of the simplified evaluation of pMSSM models using the truth-level implementations introduced in Sec. 5.1 and the simplified statistical treatment introduced here is to reduce the number of models for which the computationally expensive full analysis is run. Only for models, which can not be safely excluded or not excluded based on this first evaluation step, the analyses are additionally performed at full precision. For the models considered in the following only the simplified evaluation is performed.

5.4 Model generation

The generation of the pMSSM models considered in the following starts with choosing values for the set of pMSSM parameters for each model point. The parameter values are picked from within the ranges shown in Tab. 5.1 based on flat probability distributions. Each sampled set of parameters corresponds to one pMSSM signal model.

The parameter ranges in Tab. 5.1 are chosen such that the sampled models are suited to particularly study electroweakinos in the pMSSM with a set of ATLAS SUSY searches. Therefore the values of the mass parameters of all sleptons are set to values much higher than what is accessible at the LHC in order to decouple them from the targeted phenomenology. The same is done for the mass parameters of the first and second generation of squarks. For the mass parameters of the third generation of squarks and the gluino a compromise is chosen between not completely decoupling them for reasons connected to the concept of naturalness and setting the values high enough to not markedly affect the electroweak sector. The remaining trilinear couplings and the parameters defining the gaugino-Higgsino and Higgs sector are chosen from within ranges from 0 GeV up to several GeV in order to generate mostly models with electroweakino masses accessible by the ATLAS search program, while not constraining the probed parameter space too much.

After the random sample is drawn from the parameter space introduced above, for each sampled model the corresponding SUSY spectrum and other properties are calculated. A set of publicly available software packages combined in a framework called EASYS SCANHEP [113] are used. In a first step SPHENO [114, 115] is used to calculate the sparticle spectrum, which serves as input for the calculation of the masses and branching fractions of the Higgs sector with FEYNHIGGS [116–118]. The output of the Higgs sector calculations is then used to run the spectrum generation with SPHENO again in order to get improved results based on the correct Higgs properties. An additional calculation of the SUSY spectrum is performed with

parameter	min	max	meaning
$m_{\tilde{L}_1} = m_{\tilde{L}_2}$	10 TeV	10 TeV	Left-handed slepton (first two gens.) mass
$m_{\tilde{e}_1} = m_{\tilde{e}_2}$	10 TeV	10 TeV	Right-handed slepton (first two gens.) mass
$m_{\tilde{L}_3}$	10 TeV	10 TeV	Left-handed stau double mass
$m_{\tilde{e}_3}$	10 TeV	10 TeV	Right-handed stau mass
$m_{\tilde{Q}_1} = m_{\tilde{Q}_2}$	10 TeV	10 TeV	Left-handed squark (first two gens.) mass
$m_{\tilde{u}_1} = m_{\tilde{u}_2}$	10 TeV	10 TeV	Right-handed up-type squark (first two gens.) mass
$m_{\tilde{d}_1} = m_{\tilde{d}_2}$	10 TeV	10 TeV	Right-handed down-type squark (first two gens.) mass
$m_{\tilde{Q}_3}$	2 TeV	5 TeV	Left-handed squark (third gen.) mass
$m_{\tilde{u}_3}$	2 TeV	5 TeV	Right-handed top squark mass
$m_{\tilde{d}_3}$	2 TeV	5 TeV	Right-handed bottom squark mass
$ M_1 $	0 TeV	2 TeV	Bino mass parameter
$ M_2 $	0 TeV	2 TeV	Wino mass parameter
$ \mu $	0 TeV	2 TeV	Bilinear Higgs mass parameter
M_3	1 TeV	5 TeV	Gluino mass parameter
$ A_t $	0 TeV	8 TeV	Trilinear top coupling
$ A_b $	0 TeV	2 TeV	Trilinear bottom coupling
$ A_\tau $	0 TeV	2 TeV	Trilinear τ lepton coupling
M_A	0 TeV	5 TeV	Pseudoscalar Higgs boson mass
$\tan \beta$	1	60	Ratio of the Higgs vacuum expectation values

Table 5.1: Ranges of the pMSSM parameters from which random values are drawn based on a flat probability distribution to generate a set of pMSSM models focusing on the electroweak sector. For the parameters written with a modulus sign positive and negative values are possible.

SOFTSUSY [119]. Due to worse performance, the output of this calculation is not used in the following studies other than to exclude models with pathological properties for which the software does not run successfully. Additional properties related to dark matter, as e.g. the relic abundance are calculated with MICROMEAS [120].

Models where any of the mentioned programs did not run successfully are discarded, before cross sections are computed with PROSPINO [121, 122]. The models are further filtered based on the calculated cross section. All models with inclusive production cross sections for electroweakinos below 0.07 fb are discarded as they would not produce an amount of expected signal events at an integrated luminosity of 139 fb^{-1} which is sufficient to be sensitive with the employed SUSY searches. Models where the LSP is not a neutralino are discarded. The models are required to satisfy an upper limit $\Omega_{\tilde{\chi}} h^2 < 0.12$ on the relic abundance of the lightest neutralino, which is set by the Planck experiment [23] and allows the neutralino to possibly be only a component of DM. This constraint causes most of the models with a Bino-like LSP to be filtered out. The resulting set of pMSSM models studied in the following contains 26,210 models.

Truth-level events are generated for each model using MADGRAPH5_AMC@NLO [71, 72] and PYTHIA8 [73] with the number of events N determined by an effective luminosity $L_{\text{eff}} = 700 \text{ fb}^{-1}$ and the total production cross section σ as

$$N = \sigma \times L_{\text{eff}}. \quad (5.1)$$

A minimum number of 10,000 and a maximum number of 1,000,000 events is generated per model point.

	all models	Bino LSP	Wino LSP	Higgsino LSP
number of models	26210	629	11190	14391
excluded by 1Lbb	1.6%	0.3%	3.7%	0.0%
excluded by 2L0J	2.2%	1.7%	5.0%	0.0%
excluded by EwkCompressed	5.0%	5.1%	0.5%	8.5%
summary	7.7%	7.0%	6.7%	8.5%

Table 5.2: Exclusion of pMSSM models as obtained from a scan featuring 26,210 model points evaluated with the 1Lbb, 2L0J and electroweak compressed (EwkCompressed) analysis. The exclusion is in addition shown for subset of models with different LSP types.

5.5 Scan results

The models are evaluated using a preliminary set of electroweak SUSY searches performed by ATLAS: a search in final states with one lepton and a Higgs boson decaying into two b -jets [123], referred to in the following as 1Lbb, a search in final states with two leptons [124], referred to as 2L0J and the electroweak compressed search [1]. For each of the analyses the simplified version using smeared truth-level objects and the simplified likelihood is used. For each model point the overall decision on its exclusion is based on the analysis with best expected CL_s value. A model is considered excluded if $CL_s < 0.05$.

Tab. 5.2 shows the impact of the the considered electroweak SUSY searches on the set of 26,210 pMSSM models. Overall 7.7% of the models can be excluded. As already discussed the set of sampled models contains almost no models with a Bino LSP, because these typically fail the relic density constraint. The reason for the low percentage of 0.3% of models with a Bino LSP excluded by the 1Lbb search is connected to this. It has been shown (see. Ref. [111]) that this search mostly provides exclusion power to models with a Bino LSP which overproduce dark matter and are therefore filtered out during the model generation. Both the 1Lbb and the 2L0J analysis show some sensitivity to models with a Wino LSP excluding 3.7% and 5.0% of the 11,190 models respectively. The percentages of Wino LSP models excluded by the individual searches do not add up to the overall excluded percentage of 6.7%, which means that some models have a CL_s value lower than 0.05 for more than one search. The electroweak compressed analyses is the only search with sensitivity to pMSSM models with a Higgsino LSP, excluding 8.5% of the 14,391 sampled models.

In this dataset the effect of the 1Lbb analysis is not really visible as it does not contain many models with Bino LSP to which the analysis would be sensitive. The sensitivity of the 2L0J analysis in this scan is probably overestimated as there are some problems with the truth-level version of this search, generally predicting higher truth yields than reconstruction yields, similar to what has been discussed in 5.2. The plots shown in the following therefore focus on the impact of the compressed search on the model-set.

Fig. 5.5 shows the bin-wise fractions of models excluded by the electroweak compressed search in the 2-dimensional plane spanned by the masses of the two lightest neutralinos. The numbers in each bin correspond to the number of models in the respective bin, with bins left blank if there is no sampled models in that parameter region. The fraction of excluded models in this type of plots is indicated by a colour-scheme. While bins are coloured in black if all models in the bin are excluded, white bins indicate that no models are excluded. The plot in Fig. 5.5(a) shows the exclusion for models with all three LSP types, while the plots in (b)-(d) only show models with a Higgsino, Bino and Wino LSP. The same type of plots with the mass of the lightest chargino on the horizontal axis are shown in Fig. 5.6.

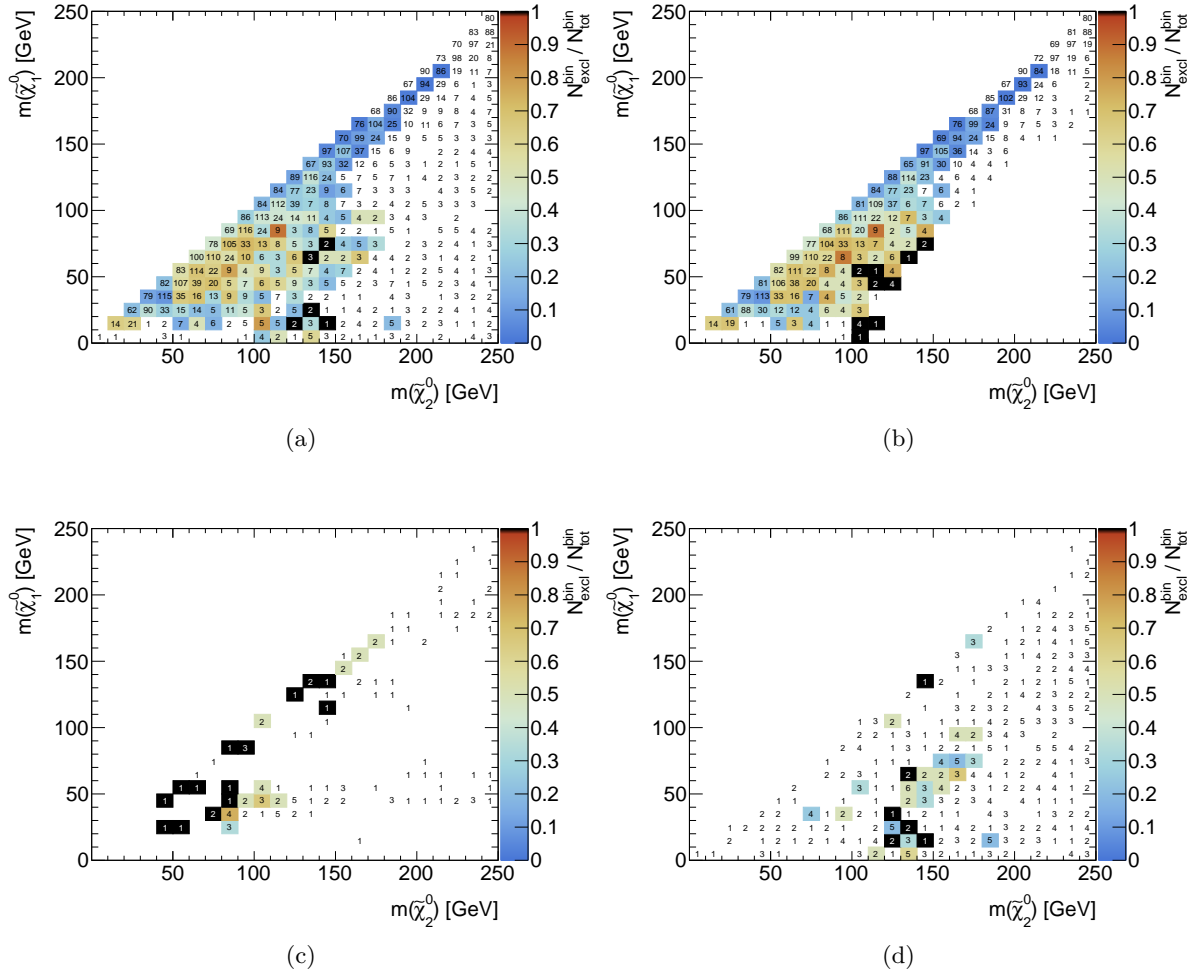


Figure 5.5: Bin-wise fractions of models excluded by the electroweak compressed search in the 2-dimensional plane of the neutralino masses $m(\tilde{\chi}_1^0)$ and $m(\tilde{\chi}_2^0)$. The exclusion of models with any LSP type is shown in (a), while the other three plots contain only models with a (b) Higgsino, (c) Bino and (d) Wino LSP. The numbers in each bin correspond to the number of models in the respective bin. The fraction of excluded models is indicated by the given colour-scheme. Bins where all models are excluded are coloured in black. Bins where no models are excluded are left white.

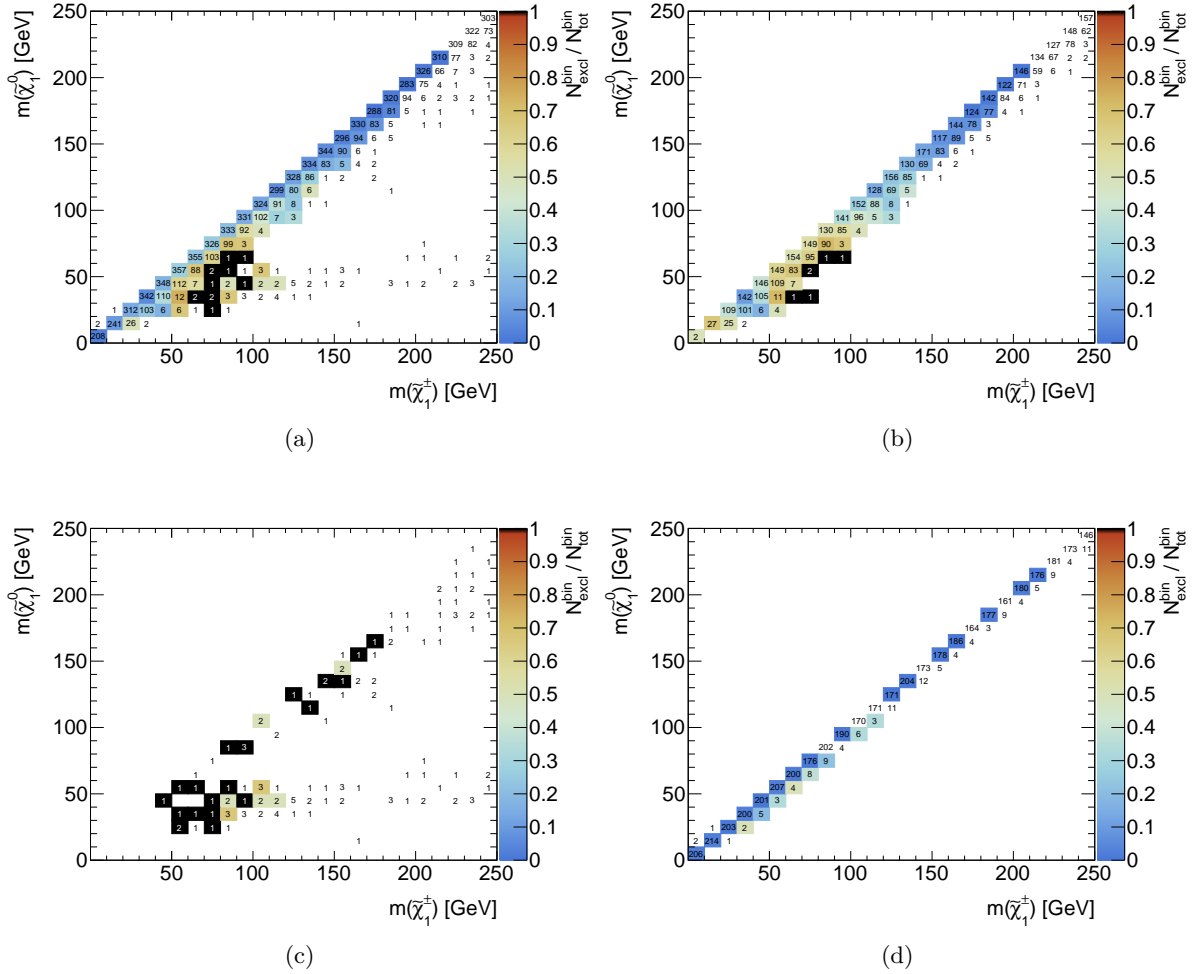


Figure 5.6: Bin-wise fractions of models excluded by the electroweak compressed search in the 2-dimensional plane of the masses $m(\tilde{\chi}_1^0)$ and $m(\tilde{\chi}_1^\pm)$ of the lightest neutralino and chargino. The exclusion of models with any LSP type is shown in (a), while the other three plots contain only models with a (b) Higgsino, (c) Bino and (d) Wino LSP.

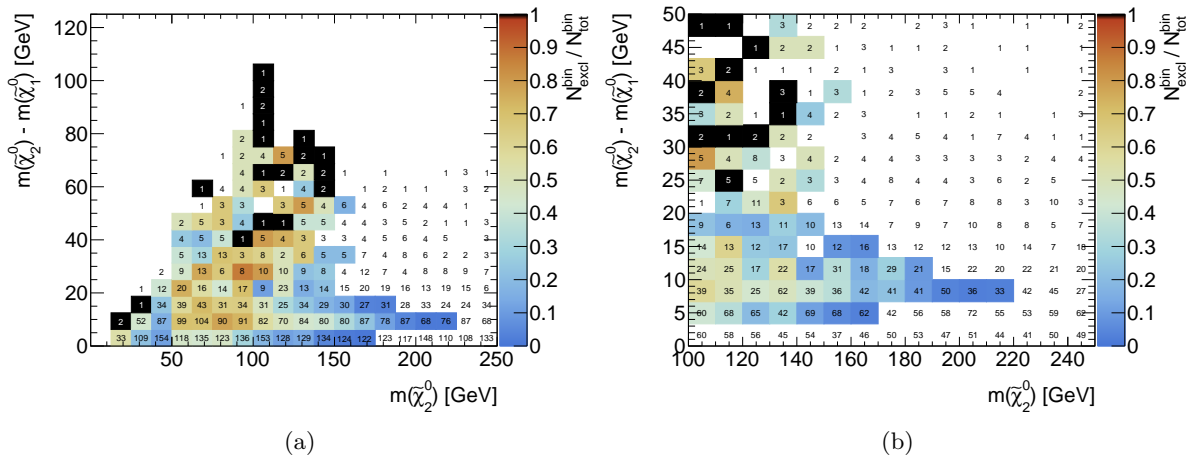


Figure 5.7: Bin-wise fractions of models with Higgsino LSP excluded by the electroweak compressed search as a function of the mass of the LSP and its mass difference with respect to the second to lightest neutralino. The plot in (a) shows all models, while the plot in (b) focuses on models with mass splittings below 50 GeV.

Unsurprisingly a high number of pMSSM models excluded by the compressed search has very compressed electroweakino mass spectra. From Fig 5.5(a) and Fig 5.6(a) it can be seen that overall models with compressed spectra with masses $m(\tilde{\chi}_2^0)$, $m(\tilde{\chi}_1^\pm)$ and $m(\tilde{\chi}_1^0)$ up to about 220 GeV can be excluded. In particular the search has sensitivity to Bino LSP models with relatively compressed spectra, which are thus similar to the simplified models considered in the original analysis (see. Fig 5.5(c) and Fig 5.6(c)). Models with a Wino LSP typically have nearly mass-degenerate $\tilde{\chi}_1^\pm$ and $\tilde{\chi}_1^0$. As can be seen from Fig 5.5(d), the analysis has some sensitivity to models with a Wino LSP, where the mass difference with the $\tilde{\chi}_2^0$ is higher and has mostly values $m(\tilde{\chi}_2^0) - m(\tilde{\chi}_1^0) > 50$ GeV.

The exclusion of models with a Higgsino LSP is also shown as a function of the mass of the LSP and its mass difference with respect to the second to lightest neutralino in Fig. 5.7. The plot on the left shows the complete relevant range of masses and mass differences, while the plot on the right focuses on the region with mass differences $m(\tilde{\chi}_2^0) - m(\tilde{\chi}_1^0) < 50$ GeV. It can be observed that, while not many Higgsino models with relatively high mass differences are sampled, these models can often be excluded. At a mass splitting slightly below 10 GeV the electroweak compressed search has sensitivity to models with masses of the $\tilde{\chi}_2^0$ of up to about 220 GeV. In general the analysis is able to exclude a good amount of pMSSM models with a Higgsino LSP in the parameter region matching the exclusion contour obtained in the analysis based on the simplified model (see. Fig. 4.8). Still, the sensitivity in the context of the pMSSM is significantly reduced, being able to only exclude a fraction of the models falling into this parameter region. Studies aiming to explore the properties of pMSSM models and to provide explanations to why some of the models, for which one might expect sensitivity, can not be excluded, are presented in Chap. 6.

5.6 Discussion

Performing large-scale reinterpretations in the pMSSM offers the possibility to determine the sensitivity of SUSY searches to SUSY scenarios more realistic than the simplified models for which the searches are originally designed. In order to make such studies computationally feasible, suitable analysis approximations are needed. For each considered analysis it has to

be checked whether these approximations are valid by comparing the results obtained with the simplified treatment with the ones from the original search. The example of the evaluation of signal models with the smeared truth-level version of the electroweak compressed analysis, discussed above, shows that this is not always as straightforward as one would hope. In this case the discrepancies between the event yields obtained from the smeared truth-level and the reconstruction-level analysis can be attributed to the presence of a high number of leptons with low values of p_T . The simplified analysis is not optimized for this low-momentum regime, which is in general difficult to handle. Nonetheless, the preliminary studies performed, show that the electroweak compressed analysis is important for scans of the electroweak sector of the pMSSM as it provides sensitivity to models with a Higgsino LSP.

The pMSSM model-set considered in this work contains almost no models with a Bino LSP, as these are filtered out by a requirement on the DM relic density. Therefore in order to assess the impact of the SUSY searches on pMSSM models with Bino LSP, which are also relevant for DM interpretations, a different sampling method has to be applied. One possibility is to include the constraint on the DM relic density (and other constraints) in a dedicated likelihood function and sample the models according to this likelihood. This is discussed further in Chap. 7.

Chapter 6

Properties of pMSSM models

The preliminary studies in Chap. 5 on the impact of ATLAS searches for electroweak SUSY production, specifically the electroweak compressed analysis, on the pMSSM parameter space, show that the searches have sensitivity beyond simplified models. The electroweak compressed search excludes models with a Higgsino LSP in regions of the electroweakino masses similar to the region excluded by the original analysis. However, the exclusion of the pMSSM models is not as strict. Only fractions of the models in the respective parameter region can be excluded. This is due to the fact that the pMSSM models are by design more complex than the simplified models considered in the original analysis. The additional properties of the considered pMSSM models, e.g. the higher number of non-decoupled sparticles and decay branching ratios not fixed to 100 % lead to signatures different than the ones targeted in the analysis and can thus reduce the sensitivity.

Analysing the properties of pMSSM models in the context of whether the models are excluded or not by existing ATLAS SUSY searches is a very interesting task. It can potentially reveal uncovered parameter regions and help to improve the future search program. As the parameter space spanned by the SUSY spectrum and the decay modes of pMSSM models is very high-dimensional, it is rather difficult to analyse. Therefore an approach based on clustering algorithms is explored in the following. These unsupervised machine learning techniques can be used to partition data into groups of data points, called clusters, which can help in assessing the properties of the data. The data points in a cluster are loosely speaking more similar to other points in their cluster than to points in other clusters. An introductory treatment to these machine learning methods can be found e.g. in Refs. [125, 126].

6.1 K-means clustering

In the studies presented in the following the set of models generated and evaluated in Chap. 5 is analysed. The dataset used as input for the clustering algorithm consists of data points, corresponding to the pMSSM models, with features given by the masses of the electroweakinos and branching fractions of their decays. As masses and branching fractions are very different parameters on different scales, a preprocessing step is necessary in order for the algorithms, which employ the distance between data points, to produce sensible results [126]. In this step the features are transformed to the same scale. Two different approaches are used. Standardization scales (and shifts) the values of the features in the dataset so that the features have a mean of zero and unit standard deviation. Alternatively the parameters, which are non-negative by default, are scaled to lie in the range from 0 to 1, with the maximum value scaled to 1.

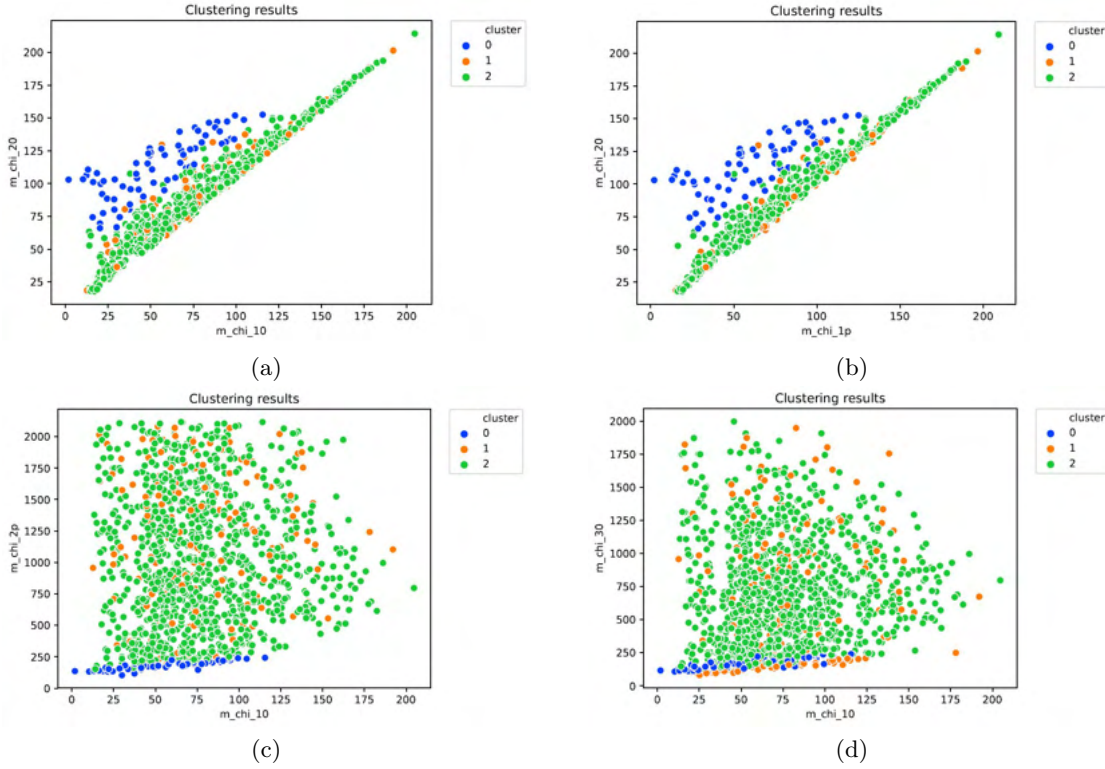


Figure 6.1: Clusterings obtained for models with a Higgsino LSP, which are excluded by the electroweak compressed analysis at 95 % CL. The plot in (a) shows the $\tilde{\chi}_1^0/\tilde{\chi}_2^0$ -plane, (b) the $\tilde{\chi}_1^\pm/\tilde{\chi}_2^0$ -plane, (c) the $\tilde{\chi}_1^0/\tilde{\chi}_2^\pm$ -plane and (d) the $\tilde{\chi}_1^0/\tilde{\chi}_3^0$ -plane. The cluster assignments are indicated by the colours shown on the right.

The implementation of a clustering algorithm called k-means in the scikit-learn package [127] is used. For this technique the number of clusters has to be specified beforehand and for each cluster a data point is chosen to represent the cluster center. The algorithm then minimizes the sum of squared distances of the data points to the cluster centers by alternately performing the following steps until the cluster centers do not change:

- Associate each data point to the nearest cluster center.
- Replace the cluster centers with the mean of the data points in the corresponding cluster.

6.2 Clustering of pMSSM models

Clusterings obtained for the set of pMSSM models with Higgsino LSP already used in Chap. 5 are discussed in the following.

Fig. 6.1 shows models with a Higgsino LSP, which are excluded by the electroweak compressed analysis at 95 % CL in the plane spanned by different combinations of electroweakino masses. The models are distributed to three different clusters, indicated by the colours. From the plots in (a) and (b) it can be seen that most of the models with less compressed mass spectra, where the mass of the $\tilde{\chi}_2^0$ is significantly higher than the $\tilde{\chi}_1^0$ and $\tilde{\chi}_1^\pm$ masses, are assigned to the cluster with the blue colour. The plots in (c) and (d) reveal that these models all have $\tilde{\chi}_2^\pm$ and $\tilde{\chi}_3^0$ masses lower than most of the other, more compressed models in the yellow and green clusters.

Overall, this approach might help to analyse the properties of pMSSM models in the context of their exclusion by the SUSY search program. Still, extracting useful information from the high number of possible clusterings is difficult.

Chapter 7

Dark matter interpretations of ATLAS SUSY searches

The pMSSM models used for the preliminary studies presented in Chap. 5 are sampled using flat probability distributions over a restricted region of the pMSSM parameter space. The restrictions on the parameter ranges are chosen such that the sampled models are suited for studies focusing on electroweakinos. In the main effort to interpret the results of ATLAS SUSY searches after Run 1 [108] the same sampling approach of picking parameter values according to flat probability distributions was chosen. Less restrictive ranges for the pMSSM parameters were used as these efforts aimed to explore the impact of SUSY searches on the complete pMSSM parameter space. Conservative upper bounds were set to ensure that all particles in the corresponding generated events are accessible at the LHC. The sampled models were then required to pass experimental constraints set by precision electroweak and flavour measurements, and dark matter and other collider experiments before they were further evaluated.

In the currently ongoing efforts within ATLAS to reinterpret the SUSY search program for Run 2 in the pMSSM, the same sampling method using flat distributions will be used. In contrast to that, the following chapter will present a different approach where constraints from other experiments are incorporated through the use of a dedicated likelihood, already during the sampling of the models. This method has already been used in a pMSSM scan performed after Run 1 [109], which focused on the electroweak sector of the pMSSM and interpretations of SUSY searches in the context of dark matter. These studies are described in more detail in Sec. 7.1. The sampling procedure involving a dedicated likelihood can be implemented in different ways. Different approaches and technical details, including the approach used in Ref. [109], are discussed in Sec. 7.2. This also includes a discussion of how the likelihood used in the electroweak Run-1 pMSSM scan is constructed, based on the considered experimental constraints, in particular with respect to measurements related to dark matter.

7.1 Run-1 electroweak pMSSM scan

The goal of the efforts presented in Ref. [109] is to study the impact of a set of ATLAS Run-1 searches for SUSY using 20 fb^{-1} of data at $\sqrt{s} = 8 \text{ TeV}$ on the electroweak production of SUSY particles in the pMSSM in particular in the context of dark matter interpretations. Therefore the studies restrict the pMSSM parameter space to a subspace with only five parameters, referred to in the following as EWKH. The relevant parameters are M_1 , M_2 , μ , $\tan \beta$ and

parameter	range
M_1 [TeV]	(-4, 4)
M_2 [TeV]	(0.01, 4)
μ [TeV]	(-4, 4)
M_A [TeV]	(0.01, 4)
$\tan\beta$	(2, 62)

Table 7.1: Considered ranges of the parameters defining the EWKH. Table adapted from Ref. [109].

m_A , defining the gaugino-higgsino and Higgs sector. The other sfermions are decoupled by setting the respective mass parameters to 4 TeV or 5 TeV. The trilinear couplings are set to 0.1 GeV. The scanned ranges of the relevant parameters can be seen in Tab. 7.1. The lightest neutralino, which is a dark matter candidate, is completely described by the 5 parameters of the EWKH and thus this model space is well suited to study the constraints placed on the models by the SUSY searches specifically from a dark matter perspective.

7.1.1 Selection of models

In order to select and subsequently evaluate a high amount of models, which are interesting in the context of dark matter a sampling strategy using a likelihood reflecting constraints from dark matter experiments is employed. Other experimental results from electroweak precision, flavour-physics and the Higgs mass measurement as well as the LEP2 limit on the chargino mass are also taken into account. The models are selected from the parameter space according to this likelihood, such that the drawn sample contains mostly models with high compatibility to the external constraints.

The distribution of the models picked by this initial likelihood scan in the plane spanned by $m(\tilde{\chi}_1^0)$ and $m(\tilde{\chi}_1^\pm)$ are shown in Fig. 7.1. The LSP composition of these models is additionally indicated by different colours. The way the sampled models are distributed in this plot is mostly induced by the constraint on the dark matter relic density [128] employed in the likelihood as an upper limit. Models with an LSP mass close to 45 GeV, such that $m(\tilde{\chi}_1^0) \approx m(Z)/2$, are able to pass the upper limit on $\Omega_{\tilde{\chi}} h^2$ due to enhanced annihilation of the lightest neutralino through s -channel Z exchange. The models in this so-called Z -funnel region have mostly Bino-like LSPs, with some models showing a sizeable Higgsino component, which increases the annihilation rate. A similar mechanism, involving s -channel Higgs exchange leads to an accumulation of models at $m(\tilde{\chi}_1^0) \approx m(h)/2$. This is called the h -funnel. The models in this region have again mostly Bino-like LSPs or Bino LSPs, which have an admixture of a Higgsino component. The reason for most models having a mostly pure Bino LSP at small LSP masses is that models with a Wino/Higgsino LSP have a lightest chargino nearly mass degenerate with the lightest neutralino and charginos with low masses are excluded by the LEP limit, which is taken into account in the initial likelihood scan. The models in the compressed region with LSP masses mostly above 100 GeV feature a variety of LSP types. Additionally, the A -funnel region is visible with models with a Bino-like LSP at masses above roughly 200 GeV. For these models the lightest neutralino can resonantly annihilate through the pseudoscalar Higgs boson.

7.1.2 Evaluation of models

Before the main evaluation step, the 570,599 sampled models are prefiltered. Models having a LSP mass below 1 GeV and not fulfilling the limit $m(\tilde{\chi}_1^\pm) > 92.4$ GeV obtained from LEP2

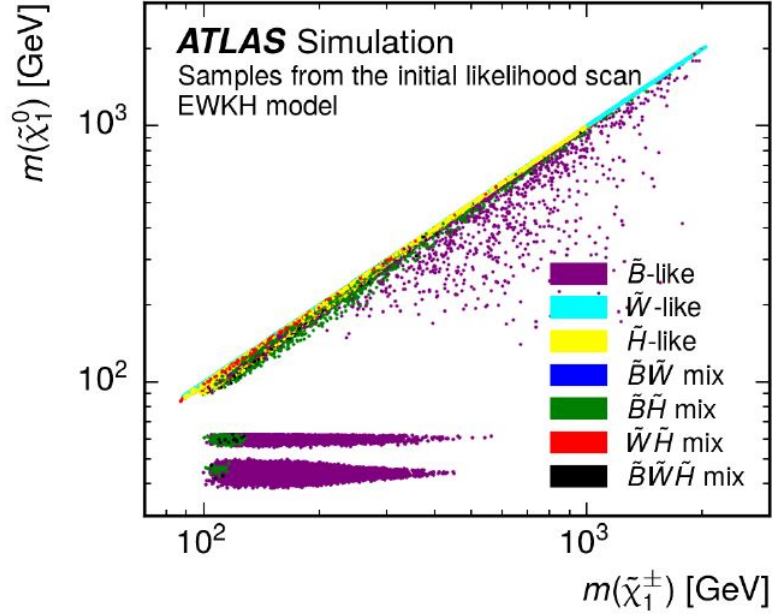


Figure 7.1: Models sampled by the initial likelihood scan. In the white area no models are selected. The colours of the points encode the phenomenology of the LSP. The $\tilde{\chi}_1^0$ is referred to as e.g. Bino-like if the corresponding fraction is at least 80 %. A mixed $\tilde{\chi}_1^0$ has at least 20 % of each denoted component and less than 20 % of the other component. Plot taken from Ref. [109].

are considered to be excluded. Models where the considered analyses are expected to be insensitive based on the total cross section of the relevant electroweak production processes are considered as unexcluded.

The remaining 326,951 models are simulated at particle-level and expected signal region yields are determined. In order to circumvent the computationally expensive ATLAS detector simulation and full statistical evaluation a calibration procedure is used. For a representative set of 500 models a fast detector simulation is performed and events are generated. The models are then evaluated using the considered set of ATLAS analyses and CL_s values are calculated to determine the model exclusion. As a further simplification, signal regions that are statistically combined in the original analysis efforts and bins of binned SRs are treated separately. The results for this set of 500 models is used to construct a calibration function mapping the particle-level event yields in the different simplified signal regions directly to CL_s values. Before this calibration function is applied the particle-level yields are scaled by a reconstruction efficiency obtained from averaging over the considered 500 models. Signal regions, where this efficiency can not be determined with enough statistical precision and/or where none of the 500 representative models can be excluded are ignored. This method is used to extract CL_s values for the complete set of models. The conservative approach of using the CL_s value determined for the SR with smallest expected value is taken.

7.1.3 Impact of ATLAS searches on the sampled models

The impact of the considered electroweak SUSY searches on the models in Fig. 7.1 is shown in Fig. 7.2. A model is considered excluded if $CL_s < 0.05$. In the plot the plane of $m(\tilde{\chi}_1^0)$ and $m(\tilde{\chi}_1^\pm)$ is divided into a number of bins. The excluded fraction of models per bin is indicated by a colour scheme as shown. The results show that a large fraction of pMSSM models can be excluded in the Z - and h -funnel regions, while there is almost no sensitivity to any models where the difference between $m(\tilde{\chi}_1^0)$ and $m(\tilde{\chi}_1^\pm)$ is small.

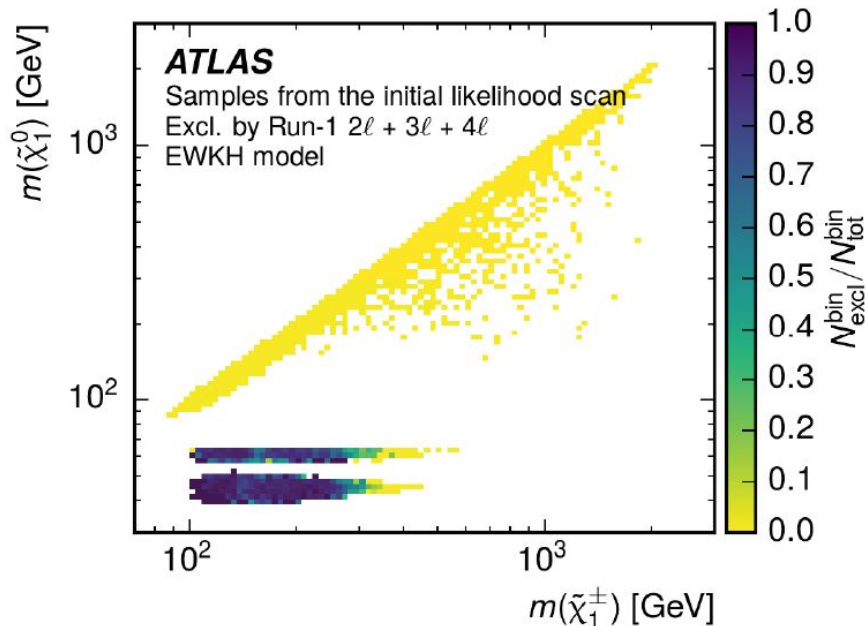


Figure 7.2: Bin-wise fraction of excluded models. In the white area no models are selected by the initial likelihood scan. The fraction of excluded models is indicated by a colour scheme. Plot adapted from Ref. [109].

7.2 Likelihood-driven sampling

The idea behind the sampling procedure employed in Ref. [109] is based on the central formula of Bayesian statistics: Bayes' Theorem. There is a vast amount of literature on the topic of Bayesian probability theory. An introduction suited to the needs of the discussion presented here can be found in Ref. [129].

7.2.1 Sampling in the spirit of Bayesian statistics

In principle Bayes' theorem is a simple consequence of the rules on how to manipulate probabilities. If one considers the joint probability of two propositions A and B , this is given by

$$p(A, B|I) = p(A|B, I)p(B|I), \quad (7.1)$$

where $p(A|B, I)$ denotes the probability of A given that B occurs and $p(B|I)$ is the probability of B on its own. The probabilities are conditional on some relevant information I , which is true for all probabilities. Since $p(A, B|I)$ is the same as $p(B, A|I)$, above relation can be written as

$$p(A|B, I)p(B|I) = p(B|A, I)p(A|I), \quad (7.2)$$

which then gives Bayes' theorem:

$$p(A|B, I) = \frac{p(B|A, I)p(A|I)}{p(B|I)}. \quad (7.3)$$

In the context presented here the relevance of this becomes more clear by replacing I and A with a given model M (as in this case the pMSSM) defined by a set of parameters Θ . The proposition B is likewise replaced by some data D . In principle a set of nuisance parameters, e.g. corresponding to relevant SM parameters, could be added to the set of parameters Θ .

This is omitted here for simplicity, but the treatment is straightforward. Then Bayes' theorem

$$p(\Theta|D, M) = \frac{p(D|\Theta, M)p(\Theta|M)}{p(D|M)} \quad (7.4)$$

gives a rule on how to update the prior $p(\Theta|M)$, which reflects the knowledge about the model parameters before seeing the data. The information provided by the data, obtained e.g. from experiments, is contained in the likelihood $p(D|\Theta, M)$, which is a measure of how well a model point with parameters Θ predicts the data set D [130]. If regarded as a function of the parameters Θ for fixed measured data it is often written as $\mathcal{L}(\Theta)$. The likelihood will typically depend on the basis parameters Θ through some derived observables $O(\Theta)$. In the context of this work, these are the observables related to electroweak precision, B -physics and the Higgs mass measurement, the LEP2 experiment as well as dark matter experiments. The likelihood constructed with these observables basically represents a comparison of the values calculated for the observables from the basis parameters Θ (with a set of different programs) and the measured values from the respective experiments. More details about how the likelihood is constructed for the Run-1 electroweak pMSSM scan are given in Sec. 7.2.3. The resulting probability distribution $p(\Theta|D, M)$ in Eq. 7.4 is called the posterior and $p(D|M)$ is the Bayesian evidence. The evidence is only a normalization, which can be ignored in the context presented here, as one is only interested in relative posterior probability.

Now this can be used in order to obtain a sample of models, which takes the constraints set by experiments into account through the corresponding likelihood, if a sample is generated such that the density of model points in the sample is proportional to the posterior probability function. This can be achieved with numerical methods as e.g. Markov Chain Monte Carlo (MCMC) techniques. MCMC algorithms construct sequences of points in the parameter space in a probabilistic way where the probability of the $(i + 1)$ -th element in the chain is determined by the i -th element. Various different algorithms exist, e.g. the so-called Metropolis-Hastings algorithm [131, 132]. It can be shown that a sequence generated this way converges to the targeted probability distribution, in this case the posterior. In practice, for each parameter point selected by the algorithm at some point, all the derived observables $O(\Theta)$ relevant for the evaluation of the likelihood $\mathcal{L}(\Theta)$ have to be calculated. The obtained value of the likelihood then gets multiplied by the prior to obtain the posterior probability for the parameter point in question.

7.2.2 Run-1 initial likelihood scan

The sampling and model selection procedure employed in the Run-1 electroweak pMSSM scan builds on the idea just presented, where a sample is drawn according to the Bayesian posterior. Based on the obtained sample, profile likelihood ratios are constructed and used to derive confidence regions. The confidence regions determine which models from the initial sample are selected to study the impact of the considered ATLAS SUSY searches.

The chosen prior probability has an effect on how thoroughly different regions in the parameter space are sampled by the numerical method involved. For the mass parameters M_1 , M_2 , μ and m_A of the constrained pMSSM model considered in the scan, both flat priors (uniform in the parameter) and log priors (uniform in the logarithm of the parameter) are used. For $\tan\beta$ only a flat prior is used. By generating and subsequently merging samples based on both types of prior (as advocated in Ref. [133]), parameter regions corresponding to low and high masses are scanned thoroughly.

The sampling of the constrained pMSSM parameter space is performed with the code MULTINEST v2.18 [134, 135], which is an implementation of the nested sampling Monte Carlo technique [136]. This algorithm is in principle designed to calculate the evidence, but also

produces posterior samples, which are, for appropriate choices of the parameters of the algorithm [133], suited to accurately map profile likelihood ratios

$$\lambda(\theta) = \frac{\mathcal{L}(\theta, \hat{\psi})}{\mathcal{L}(\hat{\theta}, \hat{\psi})}. \quad (7.5)$$

Here θ are parameters of interest, while ψ denotes other undesired parameters. The symbols with hats denote the conditional maximum likelihood estimator $\hat{\psi}$ for a given θ and the unconditional maximum likelihood estimators $\hat{\theta}$ and $\hat{\psi}$. The profile likelihood ratio $\lambda(\theta)$ can be constructed from a sample of the posterior as long as the value of the likelihood is available for every sampled point. The sample is grouped in bins of θ and for each bin the maximum likelihood is determined, which then corresponds to $\mathcal{L}(\theta, \hat{\psi})$. The unconditional maximum likelihood estimate is given by the highest likelihood value across all sampled model points. From the approximation of the profile likelihood for a one- or two-dimensional set of parameters θ , one-dimensional and two-dimensional confidence regions can be deduced by assuming that $-2 \ln \lambda(\theta)$ follows a χ^2 -distribution. The models of interest are selected based on these confidence regions. All the models shown in Figs. 7.1 and 7.2 are within the corresponding 95% confidence region of the profile likelihood.

7.2.3 Construction of the likelihood

The likelihood reflecting experimental constraints used in the Run-1 electroweak pMSSM scan is constructed as a product of the contributions for different observables. Its logarithm is given by

$$\ln \mathcal{L} = \ln \mathcal{L}_{\text{EW}} + \ln \mathcal{L}_{\text{B}} + \ln \mathcal{L}_{\text{Higgs}} + \ln \mathcal{L}_{\text{LEP}} + \ln \mathcal{L}_{\Omega_{\tilde{\chi}} h^2} + \ln \mathcal{L}_{\text{DD}}. \quad (7.6)$$

In this expression \mathcal{L}_{EW} represents constraints on electroweak precision observables, including the effective electroweak mixing angle for leptons $\sin^2 \theta_{\text{eff}}^{\text{lept}}$, the total width of the Z boson Γ_Z , the invisible Z boson width Γ_Z^{inv} , the W boson mass m_W , the hadronic pole cross-section σ_{had}^0 as well as the decay width ratios R_ℓ^0 , R_b^0 and R_c^0 [137–139]. The B -physics likelihood terms \mathcal{L}_{B} reflect constraints on the branching ratios $BR(B \rightarrow X_s \gamma)$, $BR(B_s^0 \rightarrow \mu^+ \mu^-)$ and the ratio of $BR(B_u \rightarrow \tau \nu)$ to its SM prediction [137, 140, 141]. For the Higgs boson likelihood $\mathcal{L}_{\text{Higgs}}$ the measured value of the Higgs mass presented in Ref. [142] is used. All these experimental constraints are modeled with Gaussian likelihood terms with standard deviation given by the corresponding experimental and theoretical uncertainties. The electroweak precision and flavour-physics observables are calculated from the model parameters with SUSYPOPE [143] and SUPERISO 3.0 [144] as well as SUSYBSG 1.6 [145]. The Higgs mass is computed with SOFTSUSY 3.3.10 [119], which is used to determine the SUSY spectrum.

The lower limits on the mass of the lightest chargino set by LEP2 are included with a smeared-out step function as in Ref. [146]. A value of 92.4 GeV is used as the experimental lower bound [137].

Dark matter observables

The constraint set by the Planck experiment [128] on the dark matter relic density is included through the likelihood term $\mathcal{L}_{\Omega_{\tilde{\chi}} h^2}$. The lightest neutralino is considered to be only a component of dark matter and therefore the measured value is not applied as a Gaussian likelihood term but as an upper limit instead. The expression used for the likelihood

$$\mathcal{L}_{\Omega_{\tilde{\chi}} h^2} = \mathcal{L}_0 \int_{\Omega_{\tilde{\chi}} h^2 / \sigma_{\text{Planck}}}^{\infty} e^{\frac{1}{2}(x-r_*)^2} x^{-1} dx, \quad (7.7)$$

is derived in Ref. [147] and takes uncertainties into account. Here \mathcal{L}_0 is an irrelevant normalisation constant, $r_\star \equiv \mu_{\text{Planck}}/\sigma_{\text{Planck}}$, where μ_{Planck} is the experimentally measured value of the relic density and σ_{Planck} is its uncertainty and $\Omega_{\tilde{\chi}}h^2$ is the predicted relic density of the lightest neutralino, calculated from the model parameters. The computation of $\Omega_{\tilde{\chi}}h^2$ for the models is performed with MICROMEAS 2.4 [120].

The constraints from direct dark matter detection experiments included in the likelihood through \mathcal{L}_{DD} comprise observations from the XENON100 [148, 149] and LUX [150] experiments. These experiments search for WIMP dark matter candidates (as e.g. the lightest neutralino) by measuring the ionization and scintillation signals produced by particle interactions in dedicated detectors. From the collected data the experiments identify potential recoil events with WIMP scattering off nucleons. The observed rates of these recoil events are proportional to the respective scattering cross sections and can be used to obtain limits on the cross section of the lightest neutralino off nucleons.

As a simplified likelihood reflecting the constraints set by the results of the XENON100 experiment, with an observed total number of events N and background b , a Poisson distribution

$$\mathcal{L}_{\text{XENON100}}(m_{\tilde{\chi}}, \sigma|N) = \frac{(b+s)^N}{N!} e^{-(b+s)} \quad (7.8)$$

can be used. Here $s = s(m_{\tilde{\chi}}, \sigma)$ is the expected number of signal events for a given WIMP mass, i.e. lightest neutralino mass, and scattering cross section σ . Both the spin-independent neutralino-nucleon and the spin-dependent neutralino-proton scattering cross section $\sigma_{\tilde{\chi}N}^{\text{SI}}$ and $\sigma_{\tilde{\chi}p}^{\text{SD}}$ are used and their values are calculated from the pMSSM parameters with DARKSUSY 5.0.5 [151]. The calculation of the expected total number of events s follows the procedure presented in Ref. [152]. The expected rate of recoil events of a dark matter particle off nucleons depends linearly on the local dark matter density ρ_{DM} . If the lightest neutralino is assumed to be only a component of DM, the local neutralino density $\rho_{\tilde{\chi}}$ is smaller than ρ_{DM} . This leads to a suppression of the calculated event rates by a factor $\xi = \rho_{\tilde{\chi}}/\rho_{\text{DM}}$, which, following Ref. [153], is assumed to be given by

$$\xi = \frac{\rho_{\tilde{\chi}}}{\rho_{\text{DM}}} = \frac{\Omega_{\tilde{\chi}}}{\Omega_{\text{DM}}}, \quad (7.9)$$

where $\Omega_{\tilde{\chi}}$ is relic density calculated for the corresponding model and Ω_{DM} is the value measured by the Planck experiment. The likelihood given by a single Poisson function ignores the energy distribution of the observed events and only takes their total number into account. Data from XENON100 collected over a duration of 225 live days with a 34 kg fiducial volume is used [148, 149]. The observed number of events is $N = 2$ with a background prediction of $N_b = 1.0 \pm 0.2$ events.

The results of the LUX experiment are included with a likelihood constructed with the LUXCalc package [154] based on the same type of Poisson distribution.

7.3 Updating the Run-1 procedure

The sampling procedure involving a dedicated likelihood provides an efficient way to select models from the pMSSM parameter space, which are particularly interesting from the dark matter perspective. In the main efforts of the ATLAS Collaboration, aiming to assess the impact of the searches for the electroweak production of supersymmetric particles on the pMSSM parameter space after Run 2, this approach will not be used. The models are going to be randomly sampled according to flat probability distributions and experimental constraints will be applied only at a later stage, in order to allow the scan to be more general. Nonetheless,

reproducing the studies reviewed in the above chapter, is certainly interesting and offers the possibility to compare results obtained with the different approaches. In comparison to the Run-1 procedure the evaluation of the sampled pMSSM models at smeared truth-level together with the simplified likelihoods introduced in Chap. 5 offers a much more reliable and powerful reinterpretation method. Furthermore the likelihood function, reflecting the external experimental constraints, used in the scan can be updated to include the newest results, as e.g. the limits set by the most recent dark matter direct-detection experiments conducted by the XENON Collaboration [155].

The software used in the reinterpretation procedure presented in Chap. 5 is publicly available. This includes the analysis implementations collected in the SIMPLEANALYSIS framework but without the smearing procedure. The ATLAS Collaboration recently also started to publish the full likelihoods of analyses, which allows efforts outside of ATLAS to construct the simplified likelihoods used in the evaluation of models. With this it is possible to perform an updated likelihood-driven pMSSM scan focusing on dark matter interpretations in parallel to the official ATLAS efforts.

Chapter 8

Conclusion

This work gave an overview of a search for the direct production of electroweakinos with compressed mass spectra in a final state with two leptons, missing transverse momentum and hadronic activity. Data from proton-proton collisions at $\sqrt{s} = 13$ TeV, corresponding to an integrated luminosity of 139 fb^{-1} recorded with the ATLAS detector in Run 2 of the LHC was analysed in the original analysis. The search is mainly optimised for a simplified model where a pair-produced $\tilde{\chi}_1^\pm$ and $\tilde{\chi}_2^0$ decay to an off-shell W boson and $\tilde{\chi}_1^0$ as well as an off-shell Z boson and $\tilde{\chi}_1^0$. The search mainly targets the scenario where a subsequent decay of the off-shell Z boson produces a pair of leptons, for which the dilepton invariant mass $m_{\ell\ell}$ has a kinematic endpoint determined by the mass splitting between the two lightest neutralinos. In order to search for electroweakinos with compressed mass spectra the analysis therefore requires excellent reconstruction of low p_T leptons. The sensitivity of the search is enhanced by requiring the presence of a jet from initial state radiation.

The search defines exclusion signal regions optimised for the considered simplified model. All signal regions are mutually exclusive and divided into bins of $m_{\ell\ell}$ and can thus be statistically combined in a shape-fit, which exploits the differences in shape of the distribution in this variable between the SUSY signal and SM background processes. The dominant contributions to the SM background from $t\bar{t}/tW$, WW/WZ and $Z^{(*)}/\gamma^*(\rightarrow \tau\tau) + \text{jets}$ processes are estimated with a semi-data-driven method using dedicated control regions.

No significant excess has been observed in any of the signal regions and exclusion limits are set. The analysis is able to exclude scenarios where the $\tilde{\chi}_2^0$ is about 9 GeV heavier than the Higgsino-like LSP up to $\tilde{\chi}_2^0$ masses of slightly below 200 GeV at 95% CL. Models within a range of mass splittings from roughly 2 GeV to 55 GeV can be excluded in this case. For scenarios where the LSP is Bino-like, $\tilde{\chi}_2^0$ masses of maximally 240 GeV are excluded with mass splittings ranging from 1.5 GeV to 46 GeV.

Overall the search is able to achieve sensitivity to electroweakinos with very compressed mass spectra and exclude sizeable amounts of parameter space, despite the challenging to target signature with low energetic leptons.

The non-observation of a significant sign for SUSY in the presented analysis matches the results of other searches performed by ATLAS (and CMS) analysing the Run-1 and Run-2 dataset of the LHC. Having the full dataset of Run 2 available together with new developments in terms of analysis techniques and strategies improves the sensitivity especially of searches for electroweakinos and sleptons. This leads to an increase of the regions of sparticle masses ruled out by the exclusion limits. However, as these limits are usually obtained in the context of simplified models, their scope is limited to the specific assumptions made in these models. Realistic SUSY scenarios typically do not fulfill these assumptions like e.g. only having a

small number of relevant sparticles and fixed decay mode for each. Therefore the limits set by searches in simplified models can not be interpreted as constraints on the sparticles in more realistic SUSY scenarios directly.

From this point of view, performing reinterpretations of SUSY searches in more complex models is a highly desirable task. Large-scale reinterpretations, e.g. in the 19-parameter phenomenological MSSM, including a set of SUSY searches based on simplified models, offer the possibility to determine a combined sensitivity of the searches in more complete SUSY scenarios. As these large-scale efforts are computationally challenging, suitable analysis approximations are necessary. Studies in order to validate the smeared truth-level implementation of the electroweak compressed analysis have been presented. These studies revealed a discrepancy between the approximated and the original analysis, which can be traced back to the search targeting a signature with low energetic leptons, for which the simplified treatment is not optimized. A reinterpretation in the phenomenological MSSM was performed, which showed that the electroweak compressed analysis provides sensitivity to models with a Higgsino LSP. For this reason the search is important in the context of large-scale reinterpretation efforts in the pMSSM.

Another important aspect of performing reinterpretations of SUSY searches in the phenomenological MSSM is that results from direct and indirect dark matter searches can be taken into account. In the considered model-set the majority of the models with a Bino LSP are discarded, because they do not fulfill the constraint on the DM relic density. In order to select only models relevant in the context of dark matter for further evaluation, a sampling method based on a dedicated likelihood reflecting the corresponding constraints by DM experiments can be used. In this context updating efforts performed after Run 1 with improved evaluation strategies and new experimental results is highly desirable.

Another reason to continue searching for SUSY at the LHC is, that so far only a fraction of the amount of data, which the LHC is designed to record, has been analysed. While the evaluation of the Run-2 dataset is still ongoing, a third data-taking period is planned to start in 2022 and deliver an integrated luminosity of pp collision data equal to the two previous runs combined [156]. After Run 3 the LHC is going to receive a big upgrade, raising the total luminosity delivered to the experiments during the lifetime of the LHC to about 3000 fb^{-1} [157]. The High Luminosity Large Hadron Collider (HL-LHC) is planned to start operation in 2027. This will enable searches for supersymmetric scenarios currently not accessible.

Bibliography

- [1] ATLAS Collaboration. Searches for electroweak production of supersymmetric particles with compressed mass spectra in $\sqrt{s} = 13$ TeV pp collisions with the ATLAS detector. *Phys. Rev. D*, 101(5), 2020. doi: <http://dx.doi.org/10.1103/PhysRevD.101.052005>.
- [2] M. D. Schwartz. *Quantum Field Theory and the Standard Model*. Cambridge University Press, 2014.
- [3] I. C. Brock and T. Schoerner-Sadenius. *Physics at the Terascale*. Wiley, Weinheim, 2011. doi: <http://dx.doi.org/10.1002/9783527634965>.
- [4] S. P. Martin. A Supersymmetry Primer. *Advanced Series on Directions in High Energy Physics*, 18:1–98, 1998. doi: http://dx.doi.org/10.1142/9789812839657_0001.
- [5] M. Bustamante, L. Cieri, and J. Ellis. Beyond the Standard Model for Montaneros. arXiv:0911.4409 [hep-ph], 2009.
- [6] S. L. Glashow. Partial-symmetries of weak interactions. *Nuclear Physics*, 22:579–588, 1961. doi: [http://dx.doi.org/10.1016/0029-5582\(61\)90469-2](http://dx.doi.org/10.1016/0029-5582(61)90469-2).
- [7] S. Weinberg. A Model of Leptons. *Phys. Rev. Lett.*, 19:1264–1266, 1967. doi: <http://dx.doi.org/10.1103/PhysRevLett.19.1264>.
- [8] A. Salam. Weak and Electromagnetic Interactions. *Conf. Proc. C*, 680519:367–377, 1968. doi: http://dx.doi.org/10.1142/9789812795915_0034.
- [9] F. Englert and R. Brout. Broken Symmetry and the Mass of Gauge Vector Mesons. *Phys. Rev. Lett.*, 13:321–323, 1964. doi: <http://dx.doi.org/10.1103/PhysRevLett.13.321>.
- [10] P. W. Higgs. Broken Symmetries and the Masses of Gauge Bosons. *Phys. Rev. Lett.*, 13:508–509, 1964. doi: <http://dx.doi.org/10.1103/PhysRevLett.13.508>.
- [11] P. W. Higgs. Spontaneous Symmetry Breakdown without Massless Bosons. *Phys. Rev.*, 145:1156–1163, 1966. doi: <http://dx.doi.org/10.1103/PhysRev.145.1156>.
- [12] D. J. Gross and F. Wilczek. Ultraviolet Behavior of Non-Abelian Gauge Theories. *Phys. Rev. Lett.*, 30:1343–1346, 1973. doi: <http://dx.doi.org/10.1103/PhysRevLett.30.1343>.
- [13] H. D. Politzer. Reliable Perturbative Results for Strong Interactions? *Phys. Rev. Lett.*, 30:1346–1349, 1973. doi: <http://dx.doi.org/10.1103/PhysRevLett.30.1346>.
- [14] Particle Data Group. Review of Particle Physics. *Progress of Theoretical and Experimental Physics*, 2020(8), 2020. doi: <http://dx.doi.org/10.1093/ptep/ptaa104>.
- [15] E. Wigner. On Unitary Representations of the Inhomogeneous Lorentz Group. *Annals of Mathematics*, 40(1):149–204, 1939. doi: <http://dx.doi.org/10.2307/1968551>.

- [16] C. N. Yang and R. L. Mills. Conservation of Isotopic Spin and Isotopic Gauge Invariance. *Phys. Rev.*, 96:191–195, 1954. doi: <http://dx.doi.org/10.1103/PhysRev.96.191>.
- [17] Y. Nambu. Quasi-Particles and Gauge Invariance in the Theory of Superconductivity. *Phys. Rev.*, 117:648–663, 1960. doi: <http://dx.doi.org/10.1103/PhysRev.117.648>.
- [18] J. Goldstone. Field theories with Superconductor solutions. *Nuovo Cim*, 19:154–164, 1961. doi: <http://dx.doi.org/10.1007/BF02812722>.
- [19] N. Cabibbo. Unitary Symmetry and Leptonic Decays. *Phys. Rev. Lett.*, 10:531–533, 1963. doi: <http://dx.doi.org/doi/10.1103/PhysRevLett.10.531>.
- [20] M. Kobayashi and T. Maskawa. CP-Violation in the Renormalizable Theory of Weak Interaction. *Progress of Theoretical Physics*, 49:652–647, 1973. doi: <http://dx.doi.org/10.1143/PTP.49.652>.
- [21] G. Bertone, D. Hooper, and J. Silk. Particle Dark Matter: Evidence, Candidates and Constraints. *Physics Reports*, 405(5):279–390, 2005. doi: <http://dx.doi.org/10.1016/j.physrep.2004.08.031>.
- [22] V. C. Rubin and W. K. Ford. Rotation of the Andromeda Nebula from a Spectroscopic Survey of Emission Regions. *Astrophys. J.*, 159, 1970. doi: <http://dx.doi.org/10.1086/150317>.
- [23] Planck Collaboration. Planck 2018 results. VI. Cosmological parameters. *Astronomy & Astrophysics*, 641(A6), 2020. doi: <http://dx.doi.org/10.1051/0004-6361/201833910>.
- [24] Super-Kamiokande Collaboration. Evidence for Oscillation of Atmospheric Neutrinos. *Phys. Rev. Lett.*, 81:1562–1567, 1998. doi: <http://dx.doi.org/10.1103/PhysRevLett.81.1562>.
- [25] J. M. Lorenz. Supersymmetry and the collider dark matter picture. *Modern Physics Letters A*, 34(30), 2019. doi: <http://dx.doi.org/10.1142/S0217732319300052>.
- [26] S. Coleman and J. Mandula. All Possible Symmetries of the S Matrix. *Phys. Rev.*, 159:1251–1256, 1967. doi: <http://dx.doi.org/10.1103/PhysRev.159.1251>.
- [27] R. Haag, J. T. Lopuszanski, and M. Sohnius. All possible generators of supersymmetries of the S -matrix. *Nuclear Physics B*, 88(2):257–274, 1975. doi: [http://dx.doi.org/10.1016/0550-3213\(75\)90279-5](http://dx.doi.org/10.1016/0550-3213(75)90279-5).
- [28] MSSM Working Group. The Minimal Supersymmetric Standard Model: Group Summary Report. arXiv:hep-ph/9901246, 1998.
- [29] Super-Kamiokande Collaboration. Search for proton decay via $p \rightarrow e^+ \pi^0$ and $p \rightarrow \mu^+ \pi^0$ in 0.31 megaton-years exposure of the Super-Kamiokande water Cherenkov detector. *Phys. Rev. D*, 95(1), 2017. doi: <http://dx.doi.org/10.1103/PhysRevD.95.012004>.
- [30] A. Djouadi, J. Kneur, and G. Moultaka. SuSpect: A Fortran code for the Supersymmetric and Higgs particle spectrum in the MSSM. *Computer Physics Communications*, 176(6):426–455, 2007. doi: <http://dx.doi.org/10.1016/j.cpc.2006.11.009>.
- [31] D. Alves, N. Arkani-Hamed, S. Arora, et al. Simplified models for LHC new physics searches. *J. Phys. G: Nucl. Part. Phys.*, 39(10):105005, 2012. doi: <http://dx.doi.org/10.1088/0954-3899/39/10/105005>.

- [32] F. Ambrogio, S. Kraml, S. Kulkarni, et al. On the coverage of the pMSSM by simplified model results. *Eur. Phys. J. C*, 78(215), 2018. doi: <http://dx.doi.org/10.1140/epjc/s10052-018-5660-0>.
- [33] CERN. *CERN Annual Report 2020*, volume 67 of *Annual Report of the European Organization for Nuclear Research*. CERN, 2021. doi: <http://dx.doi.org/10.17181/AnnualReport2020>.
- [34] L. R. Evans and P. Bryant. LHC Machine. *JINST*, 3:S08001, 2008. doi: <http://dx.doi.org/10.1088/1748-0221/3/08/S08001>.
- [35] E. Mobs. The CERN accelerator complex - 2019. Complexe des accélérateurs du CERN - 2019, 2019. URL <https://cds.cern.ch/record/2684277>.
- [36] M. Vretenar, J. Vollaie, R. Scrivens, et al. *Linac4 design report*, volume 6 of *CERN Yellow Reports: Monographs*. CERN, 2020. doi: <http://dx.doi.org/10.23731/CYRM-2020-006>.
- [37] ATLAS Collaboration. The ATLAS Experiment at the CERN Large Hadron Collider. *JINST*, 3:S08003, 2008. doi: <http://dx.doi.org/10.1088/1748-0221/3/08/s08003>.
- [38] CMS Collaboration. The CMS experiment at the CERN LHC. *JINST*, 3:S08004, 2008. doi: <http://dx.doi.org/10.1088/1748-0221/3/08/s08004>.
- [39] ALICE Collaboration. The ALICE experiment at the CERN LHC. *JINST*, 3:S08002, 2008. doi: <http://dx.doi.org/10.1088/1748-0221/3/08/s08002>.
- [40] LHCb Collaboration. The LHCb Detector at the LHC. *JINST*, 3:S08005, 2008. doi: <http://dx.doi.org/10.1088/1748-0221/3/08/s08005>.
- [41] TOTEM Collaboration. The TOTEM Experiment at the CERN Large Hadron Collider. *JINST*, 3:S08007, 2008. doi: <http://dx.doi.org/10.1088/1748-0221/3/08/s08007>.
- [42] LHCf Collaboration. *LHCf experiment: Technical Design Report*. Number LHCF-TDR-001 in Technical design report. LHCf. CERN, 2006. URL <https://cds.cern.ch/record/926196>.
- [43] MoEDAL Collaboration. *Technical Design Report of the MoEDAL Experiment*. Number MoEDAL-TDR-001 in Technical design report. MoEDAL. CERN, 2009. URL <https://cds.cern.ch/record/1181486>.
- [44] FASER Collaboration. FASER: ForwArd Search ExpeRiment at the LHC. arXiv:1901.04468 [hep-ex], 2019.
- [45] A. Hoecker. Physics at the LHC Run-2 and Beyond. arXiv:1611.07864 [hep-ex], 2016.
- [46] ATLAS Collaboration. Improved luminosity determination in pp collisions at $\sqrt{s} = 7$ TeV using the ATLAS detector at the LHC. *Eur. Phys. J. C*, 73(2518), 2013. doi: <http://dx.doi.org/10.1140/epjc/s10052-013-2518-3>.
- [47] ATLAS Collaboration. Luminosity determination in pp collisions at $\sqrt{s} = 8$ TeV using the ATLAS detector at the LHC. *Eur. Phys. J. C*, 76(653), 2016. doi: <http://dx.doi.org/10.1140/epjc/s10052-016-4466-1>.
- [48] ATLAS Collaboration. Luminosity determination in pp collisions at $\sqrt{s} = 13$ TeV using the ATLAS detector at the LHC. ATLAS-CONF-2019-021, 2019. URL <https://cds.cern.ch/record/2677054>.

- [49] CERN. Record luminosity: well done LHC, 2017. URL <https://home.cern/news/news/accelerators/record-luminosity-well-done-lhc>. Accessed: 04.10.2021.
- [50] ATLAS Collaboration. ATLAS Experiment - Public Results: Luminosity Public Results Run 2. URL https://twiki.cern.ch/twiki/bin/view/AtlasPublic/LuminosityPublicResultsRun2#Luminosity_summary_plots_for_AN2. Accessed: 04.10.2021.
- [51] D. Froidevaux and V. A. Mitsou. Experimental prospects at the Large Hadron Collider. *Journal of Physics: Conference Series*, 171:012021, 2009. doi: <http://dx.doi.org/10.1088/1742-6596/171/1/012021>.
- [52] J. Pequenaõ. Computer generated image of the whole ATLAS detector, 2008. URL <https://cds.cern.ch/record/1095926>.
- [53] J. Pequenaõ. Computer generated image of the ATLAS inner detector, 2008. URL <https://cds.cern.ch/record/1095926>.
- [54] K. Potamianos. The upgraded Pixel detector and the commissioning of the Inner Detector tracking of the ATLAS experiment for Run-2 at the Large Hadron Collider. arXiv:1608.07850 [physics.ins-det], 2016.
- [55] ATLAS Collaboration. *ATLAS Insertable B-Layer Technical Design Report*. Number ATLAS-TDR-19 in Technical design report. ATLAS. CERN, 2010.
- [56] ATLAS Collaboration. Production and Integration of the ATLAS Insertable B-Layer. *JINST*, 13(05):T05008, 2018. doi: <http://dx.doi.org/10.1088/1748-0221/13/05/t05008>.
- [57] J. Pequenaõ. Computer generated image of the ATLAS calorimeter, 2008. URL <https://cds.cern.ch/record/1095927>.
- [58] J. Pequenaõ. Computer generated image of the ATLAS muons substem, 2008. URL <https://cds.cern.ch/record/1095929>.
- [59] ATLAS Collaboration. *ATLAS level-1 trigger: Technical Design Report*. Number ATLAS-TDR-12 in Technical design report. ATLAS. CERN, 1998. URL <https://cds.cern.ch/record/381429>.
- [60] ATLAS Collaboration. *ATLAS high-level trigger, data-acquisition and controls: Technical Design Report*. Number ATLAS-TDR-16 in Technical design report. ATLAS. CERN, 2003. URL <https://cds.cern.ch/record/616089>.
- [61] A. R. Martínez on behalf of the ATLAS Collaboration. The Run-2 ATLAS Trigger System. *Journal of Physics: Conference Series*, 762:012003, 2016. doi: <http://dx.doi.org/10.1088/1742-6596/762/1/012003>.
- [62] ATLAS Collaboration. Operation of the ATLAS trigger system in Run 2. *JINST*, 15(10):P10004, 2020. doi: <http://dx.doi.org/10.1088/1748-0221/15/10/P10004>.
- [63] SUSY cross section plots. URL <https://twiki.cern.ch/twiki/bin/view/LHCPhysics/SUSYCrossSections>. Accessed: 26.10.2021.
- [64] W. Beenakker, C. Borschensky, M. Kraemer, et al. NNLL-fast: predictions for coloured supersymmetric particle production at the LHC with threshold and Coulomb resummation. *J. High Energ. Phys.*, 133, 2016. doi: [http://dx.doi.org/10.1007/JHEP12\(2016\)133](http://dx.doi.org/10.1007/JHEP12(2016)133).

- [65] J. Fiaschi and M. Klasen. Neutralino-chargino pair production at NLO + NLL with resummation-improved parton density functions for LHC Run II. *Phys. Rev. D*, 98(5), 2018. doi: <http://dx.doi.org/10.1103/PhysRevD.98.055014>.
- [66] J. Fiaschi and M. Klasen. Slepton pair production at the LHC in NLO+NLL with resummation-improved parton densities. *J. High Energ. Phys.*, 94, 2018. doi: [http://dx.doi.org/10.1007/JHEP03\(2018\)094](http://dx.doi.org/10.1007/JHEP03(2018)094).
- [67] ATLAS Collaboration. Search for electroweak production of supersymmetric states in scenarios with compressed mass spectra at $\sqrt{s} = 13$ TeV with the ATLAS detector. *Phys. Rev. D*, 97(5), 2018. doi: <http://dx.doi.org/10.1103/PhysRevD.97.052010>.
- [68] R. Barbieri and G.F. Giudice. Upper bounds on supersymmetric particle masses. *Nuclear Physics B*, 306, 1988. doi: [http://dx.doi.org/10.1016/0550-3213\(88\)90171-X](http://dx.doi.org/10.1016/0550-3213(88)90171-X).
- [69] B. de Carlos and J.A. Casas. One-loop analysis of the electroweak breaking in supersymmetric models and the fine-tuning problem. *Physics Letters B*, 309, 1993. doi: [http://dx.doi.org/10.1016/0370-2693\(93\)90940-J](http://dx.doi.org/10.1016/0370-2693(93)90940-J).
- [70] B. Fuks, M. Klasen, D.R. Lamprea, et al. Precision predictions for electroweak superpartner production at hadron colliders with RESUMMINO. *Eur. Phys. J. C*, 73(2480), 2013. doi: <http://dx.doi.org/10.1140/epjc/s10052-013-2480-0>.
- [71] J. Alwall, R. Frederix, S. Frixione, et al. The automated computation of tree-level and next-to-leading order differential cross sections, and their matching to parton shower simulations. *J. High Energ. Phys.*, 79, 2014. doi: [http://dx.doi.org/10.1007/JHEP07\(2014\)079](http://dx.doi.org/10.1007/JHEP07(2014)079).
- [72] R. Frederix and S. Frixione. Merging meets matching in MC@NLO. *J. High Energ. Phys.*, 12, 2012. doi: [http://dx.doi.org/10.1007/JHEP12\(2012\)061](http://dx.doi.org/10.1007/JHEP12(2012)061).
- [73] T. Sjöstrand, S. Ask, and J.R. Christiansen. An introduction to PYTHIA 8.2. *Comput. Phys. Commun.*, 191:159–177, 2015. doi: <http://dx.doi.org/10.1016/j.cpc.2015.01.024>.
- [74] P. Artoisenet, R. Frederix, O. Mattelaer, et al. Automatic spin-entangled decays of heavy resonances in Monte Carlo simulations. *J. High Energ. Phys.*, 15, 2013. doi: [http://dx.doi.org/10.1007/JHEP03\(2013\)015](http://dx.doi.org/10.1007/JHEP03(2013)015).
- [75] A. Djouadi, M.M. Muhlleitner, and M. Spira. Decays of Supersymmetric Particles: the program SUSY-HIT (SUSpect-SdecaY-Hdecay-InTerface). arXiv:hep-ph/0609292, 2007.
- [76] ATLAS Collaboration. The ATLAS Simulation Infrastructure. *Eur. Phys. J. C*, 2010. doi: <http://dx.doi.org/10.1140/epjc/s10052-010-1429-9>.
- [77] GEANT4 Collaboration. GEANT4: a simulation toolkit. *Nucl. Instrum. Meth. A*, 506(3):250–303, 2003. doi: [http://dx.doi.org/10.1016/S0168-9002\(03\)01368-8](http://dx.doi.org/10.1016/S0168-9002(03)01368-8).
- [78] K. Griest and D. Seckel. Three exceptions in the calculation of relic abundances. *Phys. Rev. D*, 43:3191–3203, 1991. doi: <http://dx.doi.org/10.1103/PhysRevD.43.3191>.
- [79] J. Edsjoe and P. Gondolo. Neutralino relic density including coannihilations. *Phys. Rev. D*, 56:1879–1894, 1997. doi: <http://dx.doi.org/10.1103/PhysRevD.56.1879>.
- [80] B. Fuks, M. Klasen, S. Schmiemann, et al. Realistic simplified gaugino-higgsino models in the MSSM. *Eur. Phys. J. C*, 78, 2018. doi: <http://dx.doi.org/10.1140/epjc/s10052-018-5695-2>.

- [81] ATLAS Collaboration. Performance of the ATLAS track reconstruction algorithms in dense environments in LHC Run 2. *Eur. Phys. J. C*, 77(673), 2017. doi: <http://dx.doi.org/10.1140/epjc/s10052-017-5225-7>.
- [82] T. Cornelissen, M. Elsing, I. Gavrilenko, et al. The new ATLAS track reconstruction (NEWT). *Journal of Physics: Conference Series*, 119:032014, 2008. doi: <http://dx.doi.org/10.1088/1742-6596/119/3/032014>.
- [83] ATLAS Collaboration. Vertex Reconstruction Performance of the ATLAS Detector at $\sqrt{s} = 13$ TeV. ATL-PHYS-PUB-2015-026, 2015. URL <https://cds.cern.ch/record/2037717>.
- [84] ATLAS Collaboration. Reconstruction of primary vertices at the ATLAS experiment in Run 1 proton–proton collisions at the LHC. *Eur. Phys. J. C*, 77(332), 2017. doi: <http://dx.doi.org/10.1140/epjc/s10052-017-4887-5>.
- [85] ATLAS Collaboration. Characterisation and mitigation of beam-induced backgrounds observed in the ATLAS detector during the 2011 proton-proton run. *JINST*, 8:P07004, 2013. doi: <http://dx.doi.org/10.1088/1748-0221/8/07/P07004>.
- [86] ATLAS Collaboration. Electron reconstruction and identification in the ATLAS experiment using the 2015 and 2016 LHC proton–proton collision data at $\sqrt{s} = 13$ TeV. *Eur. Phys. J. C*, 79, 2019. doi: <http://dx.doi.org/10.1140/epjc/s10052-019-7140-6>.
- [87] ATLAS Collaboration. Topological cell clustering in the ATLAS calorimeters and its performance in LHC Run 1. *Eur. Phys. J. C*, 77(490), 2017. doi: <http://dx.doi.org/10.1140/epjc/s10052-017-5004-5>.
- [88] ATLAS Collaboration. Electron and photon performance measurements with the ATLAS detector using the 2015–2017 LHC proton-proton collision data. *JINST*, 14:P12006, 2019. doi: <http://dx.doi.org/10.1088/1748-0221/14/12/P12006>.
- [89] ATLAS Collaboration. Muon reconstruction and identification efficiency in ATLAS using the full Run 2 pp collision data set at $\sqrt{s} = 13$ TeV. *Eur. Phys. J. C*, 81(578), 2021. doi: <http://dx.doi.org/10.1140/epjc/s10052-021-09233-2>.
- [90] ATLAS Collaboration. Muon reconstruction performance of the ATLAS detector in proton–proton collision data at $\sqrt{s} = 13$ TeV. *Eur. Phys. J. C*, 76(292), 2016. doi: <http://dx.doi.org/10.1140/epjc/s10052-016-4120-y>.
- [91] M. Cacciari, G.P. Salam, and G. Soyez. The anti- k_t jet clustering algorithm. *J. High Energ. Phys.*, 2008. doi: <http://dx.doi.org/10.1088/1126-6708/2008/04/063>.
- [92] ATLAS Collaboration. Jet energy scale measurements and their systematic uncertainties in proton-proton collisions at $\sqrt{s} = 13$ TeV with the ATLAS detector. *Phys. Rev. D*, 96, 2017. doi: <http://dx.doi.org/10.1103/PhysRevD.96.072002>.
- [93] ATLAS Collaboration. Performance of pile-up mitigation techniques for jets in pp collisions at $\sqrt{s} = 8$ TeV using the ATLAS detector. *Eur. Phys. J. C*, 76(581), 2016. doi: <http://dx.doi.org/10.1140/epjc/s10052-016-4395-z>.
- [94] ATLAS Collaboration. Identification and rejection of pile-up jets at high pseudorapidity with the ATLAS detector. *Eur. Phys. J. C*, 77(580), 2017. doi: <http://dx.doi.org/10.1140/epjc/s10052-017-5081-5>.

- [95] ATLAS Collaboration. ATLAS b -jet identification performance and efficiency measurement with $t\bar{t}$ events in pp collisions at $\sqrt{s} = 13$ TeV. *Eur. Phys. J. C*, 79(970), 2019. doi: <http://dx.doi.org/10.1140/epjc/s10052-019-7450-8>.
- [96] ATLAS Collaboration. Early Inner Detector Tracking Performance in the 2015 data at $\sqrt{s} = 13$ TeV. ATL-PHYS-PUB-2015-051, 2015. URL <https://cds.cern.ch/record/2110140>.
- [97] ATLAS Collaboration. Performance of missing transverse momentum reconstruction with the ATLAS detector using proton–proton collisions at $\sqrt{s} = 13$ TeV. *Eur. Phys. J. C*, 78(903), 2018. doi: <http://dx.doi.org/10.1140/epjc/s10052-018-6288-9>.
- [98] ATLAS Collaboration. E_T^{miss} performance in the ATLAS detector using 2015-2016 LHC p - p collisions. ATLAS-CONF-2018-023, 2018. URL <https://cds.cern.ch/record/2625233>.
- [99] D. Adams, C. Anastopoulos, A. Andreazza, et al. Recommendations of the Physics Objects and Analysis Harmonisation Study Groups 2014. ATL-PHYS-INT-2014-018, 2014. URL <https://cds.cern.ch/record/1743654?>
- [100] ATLAS Collaboration. Performance of the missing transverse momentum triggers for the ATLAS detector during Run-2 data taking. *J. High Energ. Phys.*, 80, 2020. doi: [http://dx.doi.org/10.1007/JHEP08\(2020\)080](http://dx.doi.org/10.1007/JHEP08(2020)080).
- [101] P. Jackson and C. Rogan. Recursive jigsaw reconstruction: HEP event analysis in the presence of kinematic and combinatoric ambiguities. *Phys. Rev. D*, 96, 2017. doi: <http://dx.doi.org/10.1103/PhysRevD.96.112007>.
- [102] ATLAS Collaboration. Measurement of the WW cross section in $\sqrt{s} = 7$ TeV pp collisions with the ATLAS detector and limits on anomalous gauge couplings. *Physics Letters B*, 712(4):289–308, 2012. doi: <http://dx.doi.org/10.1016/j.physletb.2012.05.003>.
- [103] ATLAS Collaboration. Observation and measurement of Higgs boson decays to WW^* with the ATLAS detector. *Phys. Rev. D*, 92:012006, 2015. URL <http://dx.doi.org/doi/10.1103/PhysRevD.92.012006>.
- [104] M. Baak, G.J. Besjes, D. Côté, et al. HistFitter software framework for statistical data analysis. *Eur. Phys. J. C*, 75(153), 2015. doi: <http://dx.doi.org/10.1140/epjc/s10052-015-3327-7>.
- [105] D. C. Robert, T. L. James, and T. Jordan. Evaluation of three methods for calculating statistical significance when incorporating a systematic uncertainty into a test of the background-only hypothesis for a Poisson process. *Nucl. Instrum. Meth. A*, 595(2): 480–501, 2008. doi: <http://dx.doi.org/10.1016/j.nima.2008.07.086>.
- [106] ATLAS Collaboration. Search for direct production of charginos and neutralinos in events with three leptons and missing transverse momentum in $\sqrt{s} = 8$ TeV pp collisions with the ATLAS detector. *J. High Energ. Phys.*, 169, 2014. doi: [http://dx.doi.org/10.1007/JHEP04\(2014\)169](http://dx.doi.org/10.1007/JHEP04(2014)169).
- [107] ATLAS Collaboration. Search for direct production of charginos, neutralinos and sleptons in final states with two leptons and missing transverse momentum in pp collisions at $\sqrt{s} = 8$ TeV with the ATLAS detector. *J. High Energ. Phys.*, 71, 2014. doi: [http://dx.doi.org/10.1007/JHEP05\(2014\)071](http://dx.doi.org/10.1007/JHEP05(2014)071).

- [108] ATLAS Collaboration. Summary of the ATLAS experiment's sensitivity to supersymmetry after LHC Run 1 — interpreted in the phenomenological MSSM. *J. High Energy Phys.*, 134, 2015. doi: [http://dx.doi.org/10.1007/JHEP10\(2015\)134](http://dx.doi.org/10.1007/JHEP10(2015)134).
- [109] ATLAS Collaboration. Dark matter interpretations of ATLAS searches for the electroweak production of supersymmetric particles in $\sqrt{s} = 8$ TeV proton-proton collisions. *J. High Energy Phys.*, 175, 2016. doi: [http://dx.doi.org/10.1007/JHEP09\(2016\)175](http://dx.doi.org/10.1007/JHEP09(2016)175).
- [110] ATLAS Collaboration. SimpleAnalysis: Simplified ATLAS SUSY analysis framework, 2021. URL <https://gitlab.cern.ch/atlas-sa/simple-analysis>.
- [111] E. Schanet. *Search for Charginos and Neutralinos in a Signature with a Higgs Boson and an Isolated Lepton with the ATLAS Detector and its Reinterpretation in the Phenomenological MSSM*. Phd thesis, LMU Munich, 2021. URL https://www.etp.physik.uni-muenchen.de/publications/theses/download/phd_eschanet.pdf.
- [112] E. Schanet, J. M. Lorenz, G.H. Stark, et al. Simplified likelihoods for searches for supersymmetry. ATL-COM-PHYS-2021-124, 2021. URL <https://cds.cern.ch/record/2758958>.
- [113] Y. Zhang and L. Shang. EasyScanHEP: A tool for easily connecting programs to scan parameter space of high energy physics models. URL https://github.com/phyzhangyang/EasyScan_HEP.
- [114] W. Porod. SPheno, a program for calculating supersymmetric spectra, SUSY particle decays and SUSY particle production at e^+e^- colliders. *Computer Physics Communications*, 153(2):275–315, 2003. doi: [http://dx.doi.org/10.1016/S0010-4655\(03\)00222-4](http://dx.doi.org/10.1016/S0010-4655(03)00222-4).
- [115] W. Porod and F. Staub. SPheno 3.1: extensions including flavour, CP-phases and models beyond the MSSM. *Computer Physics Communications*, 183(11):2458–2469, 2012. doi: <http://dx.doi.org/10.1016/j.cpc.2012.05.021>.
- [116] S. Heinemeyer, W. Hollik, and G. Weiglein. FeynHiggs: a program for the calculation of the masses of the neutral CP-even Higgs bosons in the MSSM. *Computer Physics Communications*, 124(1):76–89, 2000. doi: [http://dx.doi.org/10.1016/S0010-4655\(99\)00364-1](http://dx.doi.org/10.1016/S0010-4655(99)00364-1).
- [117] H. Bahl, T. Hahn, S. Heinemeyer, et al. Precision calculations in the MSSM Higgs-boson sector with FeynHiggs 2.14. *Computer Physics Communications*, 249:107099, 2020. doi: <http://dx.doi.org/10.1016/j.cpc.2019.107099>.
- [118] T. Hahn, S. Heinemeyer, W. Hollik, et al. High-Precision Predictions for the Light CP-Even Higgs Boson Mass of the Minimal Supersymmetric Standard Model. *Phys. Rev. Lett.*, 112:141801, 2014. doi: <http://dx.doi.org/10.1103/PhysRevLett.112.141801>.
- [119] B.C. Allanach. SOFTSUSY: A program for calculating supersymmetric spectra. *Computer Physics Communications*, 143(3):305–331, 2002. doi: [http://dx.doi.org/10.1016/S0010-4655\(01\)00460-X](http://dx.doi.org/10.1016/S0010-4655(01)00460-X).
- [120] G. Belanger, F. Boudjema, A. Pukhov, et al. micrOMEGAs 2.0 : A Program to calculate the relic density of dark matter in a generic model. *Computer Physics Communications*, 176(5):367–382, 2007. doi: <http://dx.doi.org/10.1016/j.cpc.2006.11.008>.
- [121] W. Beenakker, R. Hoepker, and M. Spira. PROSPINO: A Program for the Production of Supersymmetric Particles in Next-to-leading Order QCD. arXiv:hep-ph/9611232, 1996.

- [122] W. Beenakker, M. Klasen, M. Kramer, et al. Production of Charginos, Neutralinos, and Sleptons at Hadron Colliders. *Phys. Rev. Lett.*, 83:3780–3783, 1999. doi: <http://dx.doi.org/10.1103/PhysRevLett.83.3780>.
- [123] ATLAS Collaboration. Search for direct production of electroweakinos in final states with one lepton, missing transverse momentum and a Higgs boson decaying into two b -jets in pp collisions at $\sqrt{s} = 13$ TeV with the ATLAS detector. *Eur. Phys. J. C*, 80, 2020. doi: <http://dx.doi.org/10.1140/epjc/s10052-020-8050-3>.
- [124] ATLAS Collaboration. Search for electroweak production of charginos and sleptons decaying into final states with two leptons and missing transverse momentum in $\sqrt{s} = 13$ TeV pp collisions using the ATLAS detector. *Eur. Phys. J. C*, 80(123), 2020. doi: <http://dx.doi.org/10.1140/epjc/s10052-019-7594-6>.
- [125] D. Forsyth. *Applied Machine Learning*. Springer, 2019.
- [126] K. Arvai. K-Means Clustering in Python: A Practical Guide. URL <https://realpython.com/k-means-clustering-python/>. Accessed: 12.12.2021.
- [127] F. Pedregosa, G. Varoquaux, and A. others Gramfort. Scikit-learn: Machine Learning in Python. *Journal of Machine Learning Research*, 12:2825–2830, 2011.
- [128] Planck Collaboration. Planck 2013 results. XVI. Cosmological parameters. *Astronomy & Astrophysics*, 571(A16), 2014. doi: <http://dx.doi.org/10.1051/0004-6361/201321591>.
- [129] R. Trotta. Bayes in the sky: Bayesian inference and model selection in cosmology. *Contemporary Physics*, 49(2):71–104, 2008. doi: <http://dx.doi.org/10.1080/00107510802066753>.
- [130] S. S. AbdusSalam, B. C. Allanach, F. Quevedo, et al. Fitting the phenomenological MSSM. *Phys. Rev. D*, 81:095012, 2010. doi: <http://dx.doi.org/doi/10.1103/PhysRevD.81.095012>.
- [131] N. Metropolis, A. W. Rosenbluth, M. N. Rosenbluth, et al. Equation of State Calculations by Fast Computing Machines. *The Journal of Chemical Physics*, 21(6):1087–1092, 1953. doi: <http://dx.doi.org/10.1063/1.1699114>.
- [132] W.K. Hastings. Monte Carlo sampling methods using Markov chains and their applications. *Biometrika*, 57(1):97–109, 1970. doi: <http://dx.doi.org/10.1093/biomet/57.1.97>.
- [133] F. Feroz, K. Cranmer, M. P. Hobson, et al. Challenges of profile likelihood evaluation in multi-dimensional SUSY scans. *J. High Energ. Phys.*, 42, 2011. doi: [http://dx.doi.org/10.1007/JHEP06\(2011\)042](http://dx.doi.org/10.1007/JHEP06(2011)042).
- [134] F. Feroz and M. P. Hobson. Multimodal nested sampling: an efficient and robust alternative to Markov Chain Monte Carlo methods for astronomical data analyses. *Mon. Not. Roy. Astron. Soc.*, 384(2), 2008. doi: <http://dx.doi.org/10.1111/j.1365-2966.2007.12353.x>.
- [135] F. Feroz, M. P. Hobson, and M. Bridges. MultiNest: an efficient and robust Bayesian inference tool for cosmology and particle physics. *Mon. Not. Roy. Astron. Soc.*, 398(4): 1601–1614, 2009. doi: <http://dx.doi.org/10.1111/j.1365-2966.2009.14548.x>.
- [136] J. Skilling. Nested sampling for general Bayesian computation. *Bayesian Analysis*, 1 (4):833 – 859, 2006. doi: <http://dx.doi.org/10.1214/06-BA127>.

- [137] Particle Data Group. Review of Particle Physics. *Chin. Phys. C*, 38(9):090001, 2014. doi: <http://dx.doi.org/10.1088/1674-1137/38/9/090001>.
- [138] LEP Electroweak Working Group et al. Precision electroweak measurements on the Z resonance. *Physics Reports*, 427(5):257–454, 2006. doi: <http://dx.doi.org/10.1016/j.physrep.2005.12.006>.
- [139] LEP Electroweak Working Group et al. Electroweak measurements in electron–positron collisions at W -boson-pair energies at LEP. *Physics Reports*, 532(4):119–244, 2013. doi: <http://dx.doi.org/10.1016/j.physrep.2013.07.004>.
- [140] A.G. Akeroyd and F. Mahmoudi. Measuring V_{ub} and probing SUSY with double ratios of purely leptonic decays of B and D mesons. *J. High Energ. Phys.*, 2010. doi: [http://dx.doi.org/10.1007/JHEP10\(2010\)038](http://dx.doi.org/10.1007/JHEP10(2010)038).
- [141] LHCb Collaboration. Measurement of the $B_s^0 \rightarrow \mu^+ \mu^-$ Branching Fraction and Search for $B^0 \rightarrow \mu^+ \mu^-$ Decays at the LHCb Experiment. *Phys. Rev. Lett.*, 111:101805, 2013. doi: <http://dx.doi.org/10.1103/PhysRevLett.111.101805>.
- [142] ATLAS Collaboration. Measurement of the Higgs boson mass from the $H \rightarrow \gamma\gamma$ and $H \rightarrow ZZ^* \rightarrow 4\ell$ channels in pp collisions at center-of-mass energies of 7 and 8 TeV with the ATLAS detector. *Phys. Rev. D*, 90:052004, 2014. doi: <http://dx.doi.org/10.1103/PhysRevD.90.052004>.
- [143] S. Heinemeyer, W. Hollik, A. M. Weber, et al. Z pole observables in the MSSM. *J. High Energ. Phys.*, 2008(04):039–039, 2008. doi: <http://dx.doi.org/10.1088/1126-6708/2008/04/039>.
- [144] F. Mahmoudi. SuperIso v2.3: A program for calculating flavor physics observables in supersymmetry. *Computer Physics Communications*, 180(9):1579–1613, 2009. doi: <http://dx.doi.org/10.1016/j.cpc.2009.02.017>.
- [145] G. Degrossi, P. Gambino, and P. Slavich. SusyBSG: a Fortran code for $BR[B \rightarrow X_s \gamma]$ in the MSSM with Minimal Flavor Violation. *Computer Physics Communications*, 179(10):759–771, 2008. doi: <http://dx.doi.org/10.1016/j.cpc.2008.06.012>.
- [146] R. Ruiz de Austri, R. Trotta, and L. Roszkowski. A Markov chain Monte Carlo analysis of the CMSSM. *J. High Energ. Phys.*, 2006(05), 2006. doi: <http://dx.doi.org/10.1088/1126-6708/2006/05/002>.
- [147] G. Bertone, K.l Kong, R. R. de Austri, et al. Global fits of the minimal universal extra dimensions scenario. *Phys. Rev. D*, 83:036008, 2011. doi: <http://dx.doi.org/10.1103/PhysRevD.83.036008>.
- [148] XENON100 Collaboration. Dark Matter Results from 225 Live Days of XENON100 Data. *Phys. Rev. Lett.*, 109:181301, 2012. doi: <http://dx.doi.org/10.1103/PhysRevLett.109.181301>.
- [149] XENON100 Collaboration. Limits on Spin-Dependent WIMP-Nucleon Cross Sections from 225 Live Days of XENON100 Data. *Phys. Rev. Lett.*, 111:021301, 2013. doi: <http://dx.doi.org/10.1103/PhysRevLett.111.021301>.
- [150] LUX Collaboration. First Results from the LUX Dark Matter Experiment at the Sanford Underground Research Facility. *Phys. Rev. Lett.*, 112:091303, 2014. doi: <http://dx.doi.org/10.1103/PhysRevLett.112.091303>.

- [151] P. Gondolo, J. Edsjö, P. Ullio, et al. DarkSUSY: computing supersymmetric dark matter properties numerically. *Journal of Cosmology and Astroparticle Physics*, 2004 (07), 2004. doi: <http://dx.doi.org/10.1088/1475-7516/2004/07/008>.
- [152] G. Bertone, Cerdeno D. G, M. Fornasa, et al. Global fits of the cMSSM including the first LHC and XENON100 data. *Journal of Cosmology and Astroparticle Physics*, 2012 (01), 2012. doi: <http://dx.doi.org/10.1088/1475-7516/2012/01/015>.
- [153] G. Bertone, D. G. Cerdeno, M. Fornasa, et al. Identification of dark matter particles with LHC and direct detection data. *Phys. Rev. D*, 82:055008, 2010. doi: <http://dx.doi.org/10.1103/PhysRevD.82.055008>.
- [154] Savothers., A. Scaffidi, M. White, et al. LUX likelihood and limits on spin-independent and spin-dependent WIMP couplings with LUXCalc. *Phys. Rev. D*, 92:103519, 2015. doi: <http://dx.doi.org/10.1103/PhysRevD.92.103519>.
- [155] XENON Collaboration. Search for inelastic scattering of WIMP dark matter in XENON1T. *Phys. Rev. D*, 103:063028, 2021. doi: <http://dx.doi.org/10.1103/PhysRevD.103.063028>.
- [156] CERN. New schedule for CERN's accelerators and experiments, 2020. URL <https://home.cern/news/news/accelerators/new-schedule-cerns-accelerators-and-experiments>. Accessed: 08.12.2021.
- [157] CERN. HL-LHC Project Schedule. URL <https://project-hl-lhc-industry.web.cern.ch/content/project-schedule>. Accessed: 08.12.2021.

Appendix A

Validation of the truth-level electroweak compressed analysis

The following sections provide additional material on the validation of the smeared truth-level implementation of the electroweak compressed analysis presented in Sec. 5.2.2.

A.1 Comparison of kin. distributions at preselection level

Figs. A.1 and A.2 show additional distributions of kinematic observables used in the analysis for the signal point with $(m(\tilde{\chi}_2^0), m(\tilde{\chi}_1^0)) = (100, 40)$ GeV at smeared truth- and reconstruction-level. An overall excess in the event counts of the smeared truth samples in comparison to the reconstruction-level can be seen, as well as a mismatch in shape between the distributions of the p_T of the subleading lepton at low values.

Figs. A.3 and A.4 provide additional plots for the signal point with $(m(\tilde{\chi}_2^0), m(\tilde{\chi}_1^0)) = (100, 95)$ GeV. This very compressed signal point shows a higher mismatch between smeared truth- and reconstruction-level yields, due to the smearing not being sufficient for leptons with low p_T resulting from the very compressed electroweakino scenario.

Figs. A.5 and A.6 show plots of distributions of the same kinematic variables for an additional signal point with $(m(\tilde{\chi}_2^0), m(\tilde{\chi}_1^0)) = (175, 150)$ GeV. The same behaviour with an overall excess of truth-level yields is again visible.

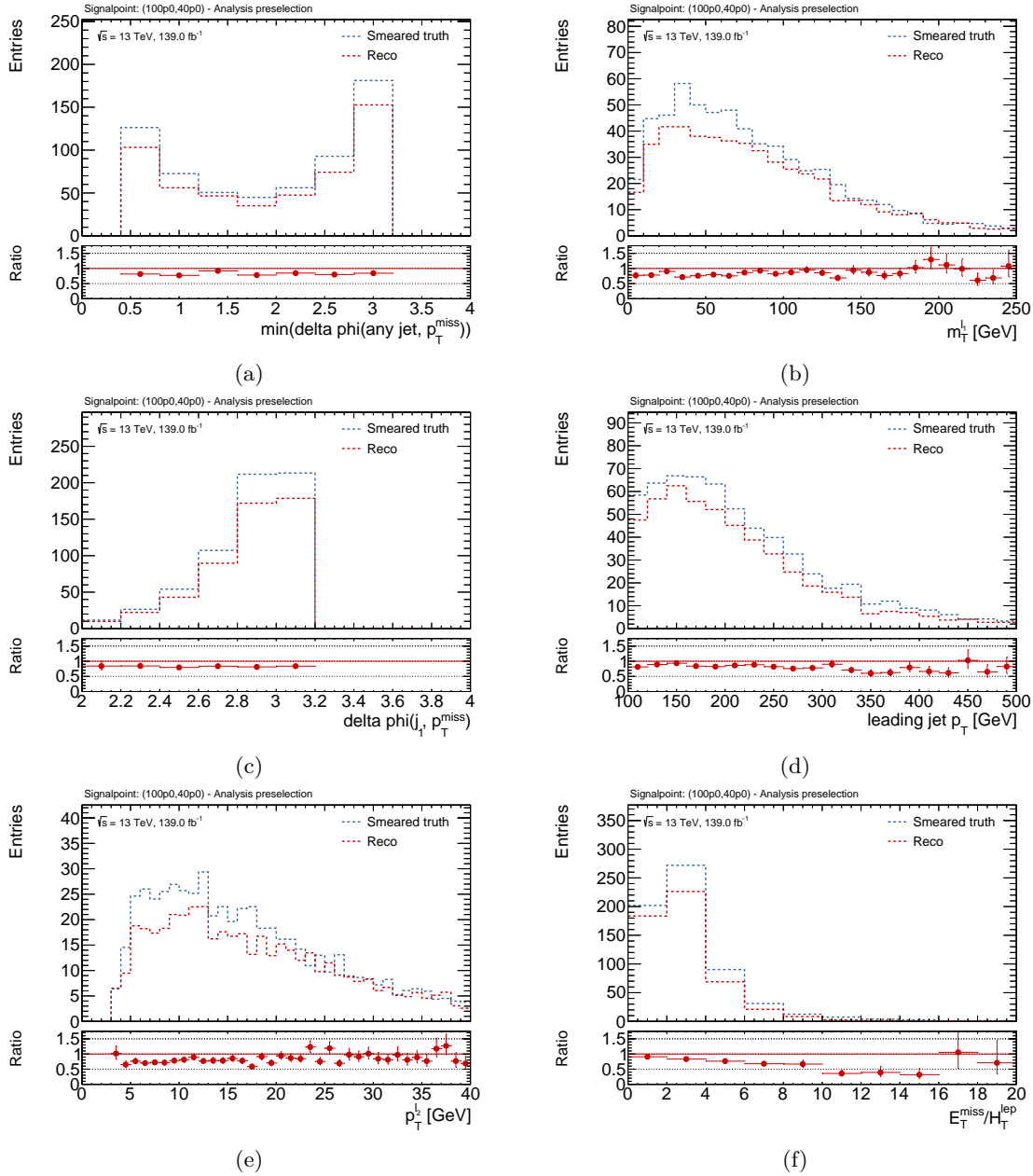


Figure A.1: Comparison of the distributions of kinematic observables used in the analysis for a signal point with $(m(\tilde{\chi}_2^0), m(\tilde{\chi}_1^0)) = (100, 40)$ GeV at smeared truth- and full-reconstruction-level. All distributions are shown in the preselection defined in Tab. 4.1. The ratio pads give the ratios of the reco- to the smeared truth-level distributions with error bars corresponding to MC statistical uncertainties.

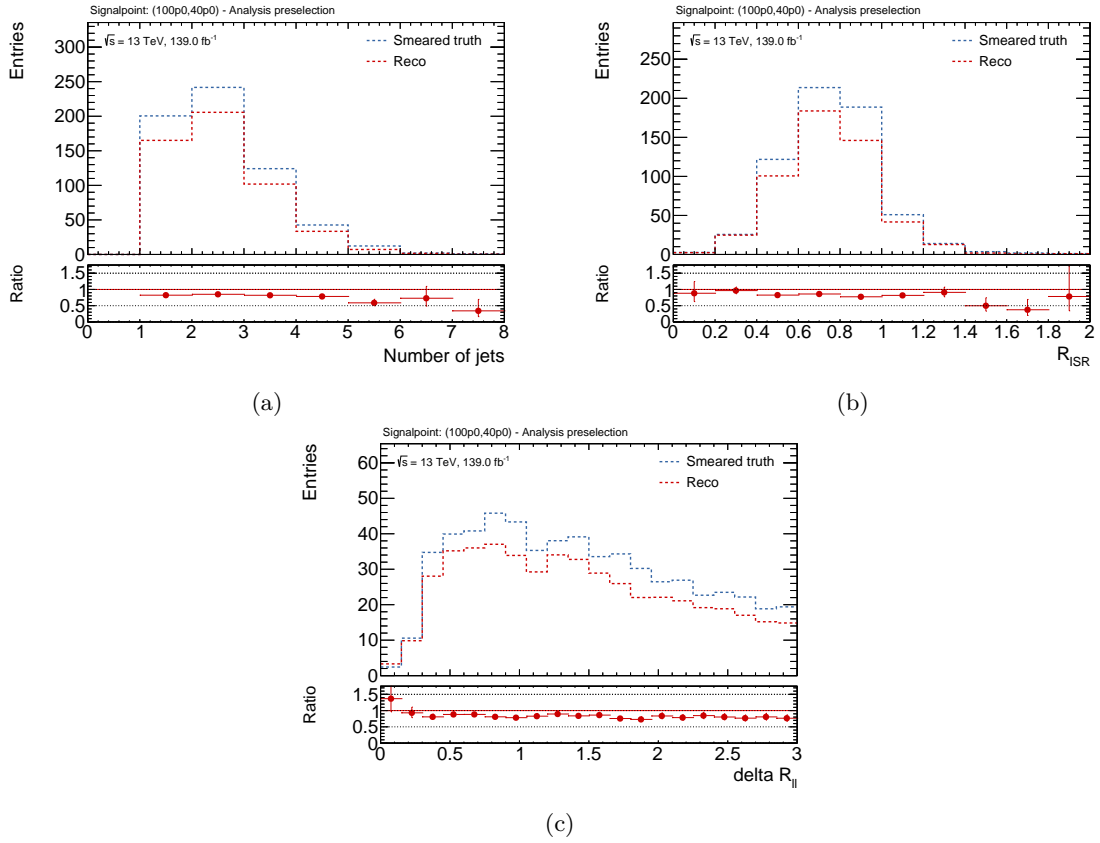


Figure A.2: Comparison of the distributions of kinematic observables used in the analysis for a signal point with $(m(\tilde{\chi}_2^0), m(\tilde{\chi}_1^0)) = (100, 40)$ GeV at smeared truth- and full-reconstruction-level. All distributions are shown in the preselection defined in Tab. 4.1. The ratio pads give the ratios of the reco- to the smeared truth-level distributions with error bars corresponding to MC statistical uncertainties.

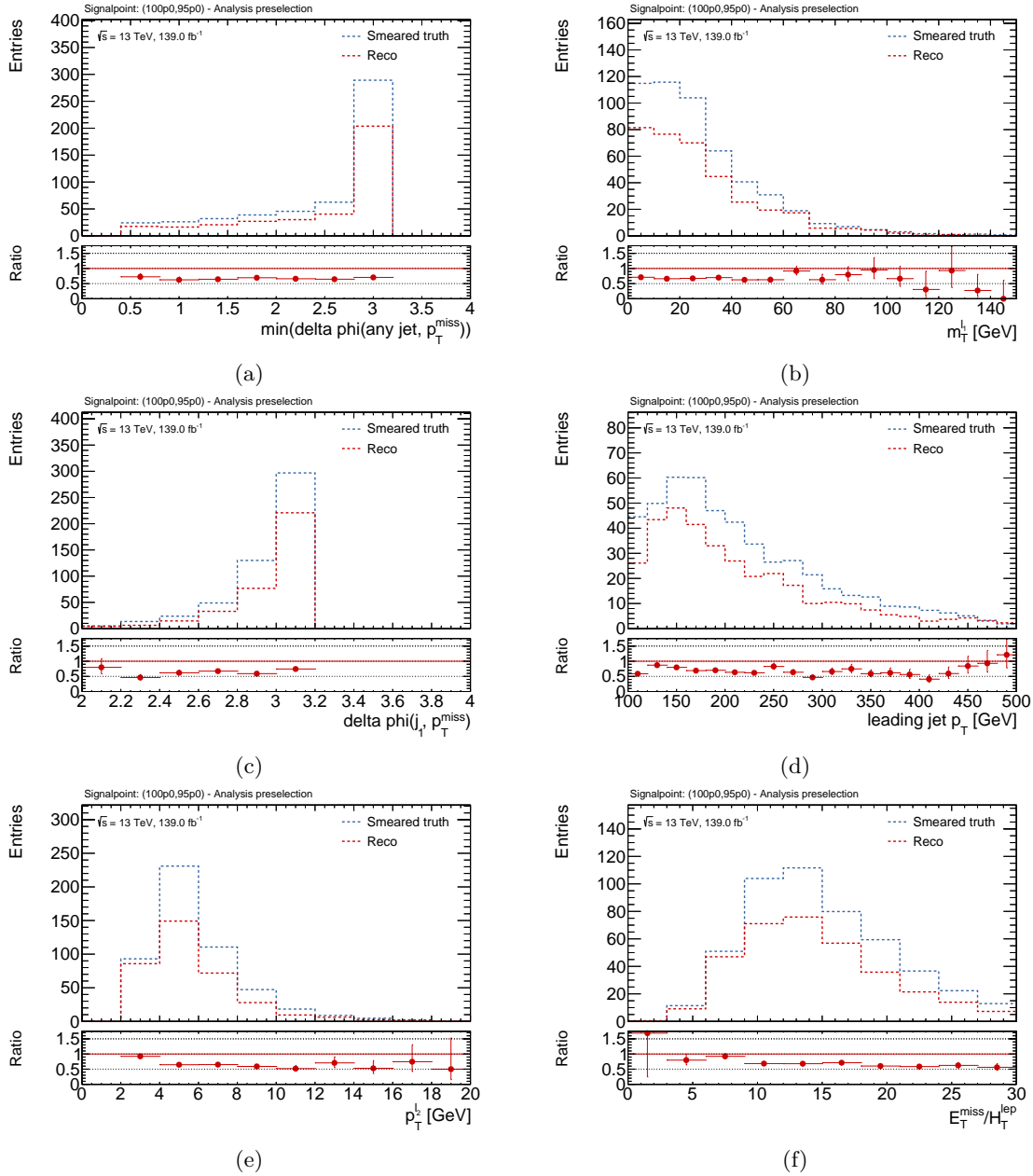


Figure A.3: Comparison of the distributions of kinematic observables used in the analysis for a signal point with $(m(\tilde{\chi}_2^0), m(\tilde{\chi}_1^0)) = (100, 95)$ GeV at smeared truth- and full-reconstruction-level. All distributions are shown in the preselection defined in Tab. 4.1. The ratio pads give the ratios of the reco- to the smeared truth-level distributions with error bars corresponding to MC statistical uncertainties.

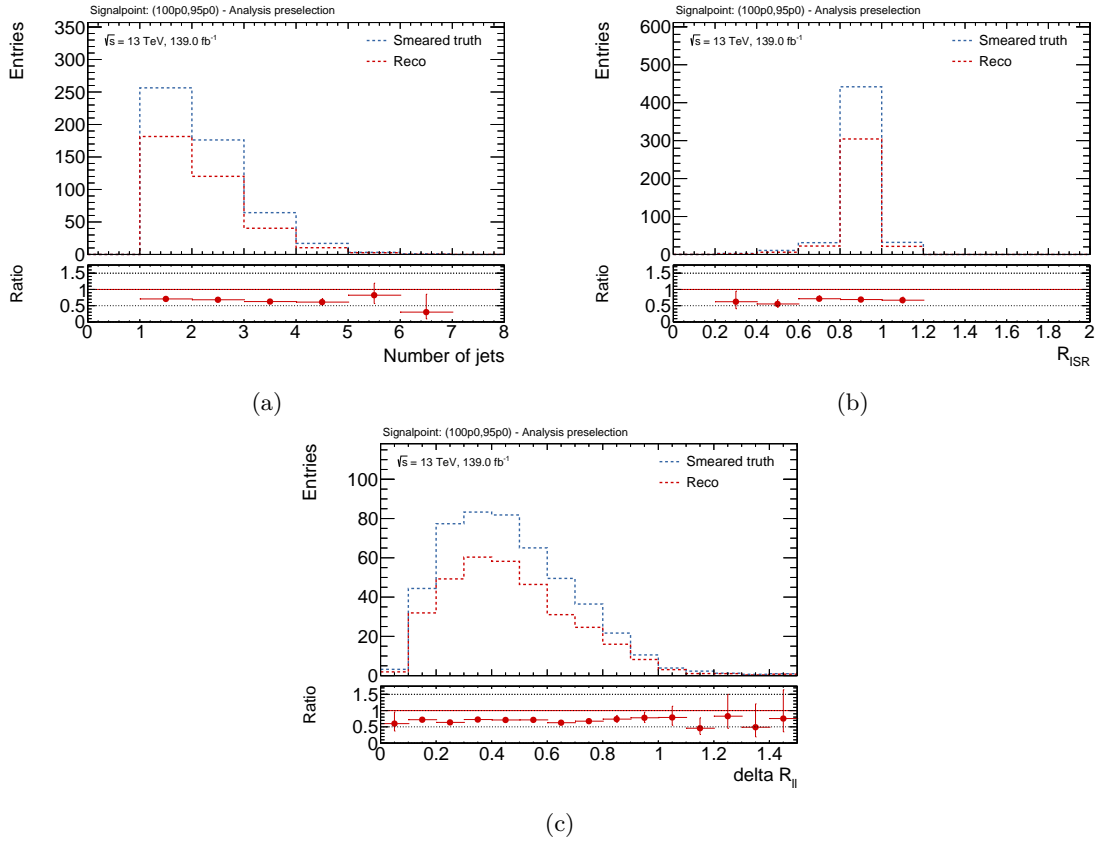


Figure A.4: Comparison of the distributions of kinematic observables used in the analysis for a signal point with $(m(\tilde{\chi}_2^0), m(\tilde{\chi}_1^0)) = (100, 95) \text{ GeV}$ at smeared truth- and full-reconstruction-level. All distributions are shown in the preselection defined in Tab. 4.1. The ratio pads give the ratios of the reco- to the smeared truth-level distributions with error bars corresponding to MC statistical uncertainties.

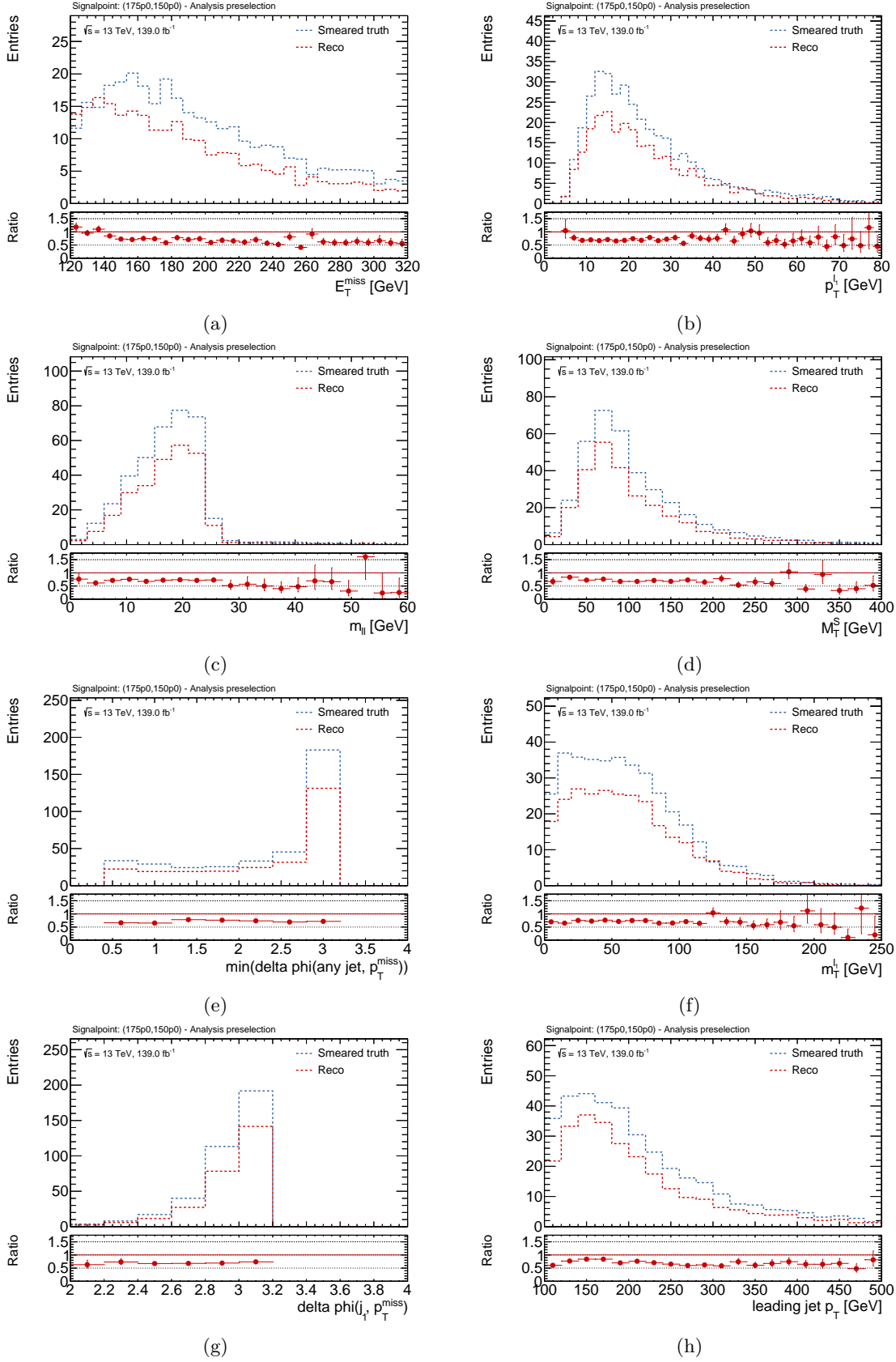


Figure A.5: Comparison of the distributions of kinematic observables used in the analysis for a signal point with $(m(\tilde{\chi}_2^0), m(\tilde{\chi}_1^0)) = (175, 150)$ GeV at smeared truth- and full-reconstruction-level. All distributions are shown in the preselection defined in Tab. 4.1. The ratio pads give the ratios of the reco- to the smeared truth-level distributions with error bars corresponding to MC statistical uncertainties.

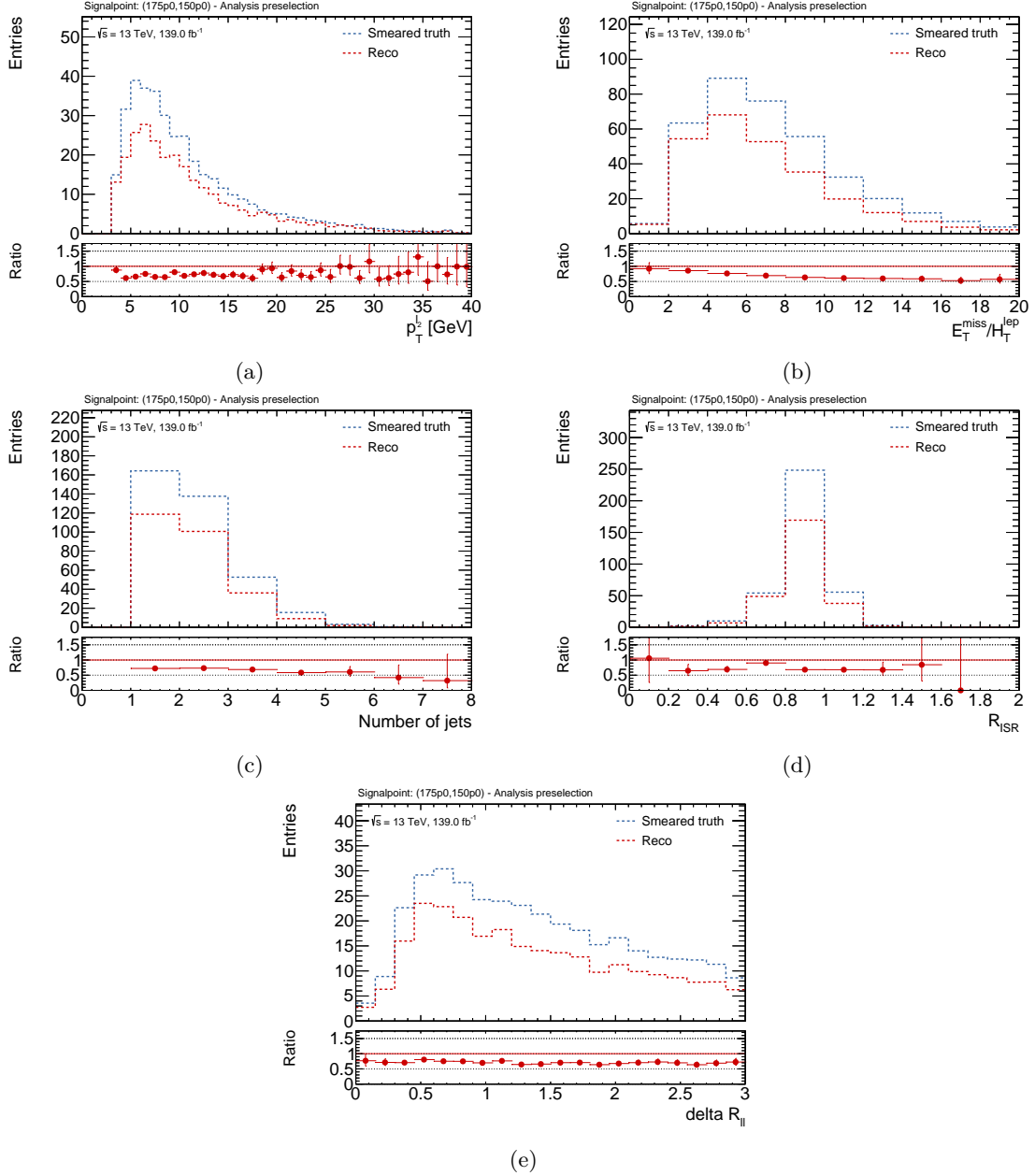


Figure A.6: Comparison of the distributions of kinematic observables used in the analysis for a signal point with $(m(\tilde{\chi}_2^0), m(\tilde{\chi}_1^0)) = (175, 150)$ GeV at smearing truth- and full-reconstruction-level. All distributions are shown in the preselection defined in Tab. 4.1. The ratio pads give the ratios of the reco- to the smeared truth-level distributions with error bars corresponding to MC statistical uncertainties.

Acknowledgements

An dieser Stelle möchte ich mich herzlich bei den Leuten bedanken, die mich während des Masterprojekts und beim Anfertigen dieser Arbeit unterstützt haben.

Zuallererst, Dr. Jeanette Lorenz die es mir ermöglicht hat diese Arbeit bei ihr als Betreuerin durchzuführen und mich trotz ihres Jobwechsels weiterhin betreut hat. Ein riesiges Dankeschön insbesondere für das Einsetzen für die Verlängerung meiner Abgabefrist, ohne die diese Arbeit nicht existieren würde. Danke auch an Dr. Otmar Biebel, der diese genehmigt hat.

Vielen Dank an Eric Schanet (mittlerweile Dr. Eric Schanet) für das stets ausführliche Beantworten meiner Fragen und die Vorschläge und Korrekturen zu dieser Arbeit.

Ein herzliches Dankeschön an Dr. Philipp Mogg für das Übernehmen der Betreuung meines Projekts ab der zweiten Hälfte und das Korrekturlesen der Arbeit.

Zu guter Letzt, danke an meine Frau Sarah, die immer für mich da ist und ohne die ich vermutlich durchgedreht wäre.

Selbstständigkeitserklärung

Hiermit erkläre ich, die vorliegende Arbeit selbständig verfasst zu haben und keine anderen als die in der Arbeit angegebenen Quellen und Hilfsmittel benutzt zu haben.

Pienzenau, 14.12.2021